NUMERICAL WEATHER PREDICTION OF GREAT SALT LAKE EFFECT PRECIPITATION AT CONVECTION-PERMITTING GRID SPACINGS

by

John Daniel McMillen

A dissertation submitted to the faculty of
The University of Utah
in partial fulfillment of the requirements for the degree of

Doctor of Philosophy

Department of Atmospheric Sciences

The University of Utah

December 2014

The University of Utah Graduate School

STATEMENT OF DISSERTATION APPROVAL

The dissertation of **John Daniel McMillen**

has been approved by the following supervisory committee members:

W. James Steenburgh, Chair **15 July 2014** Date Approved

Steven Krueger, Member **15 July 2014** Date Approved

Zhaoxia Pu, Member **15 July 2014** Date Approved

Jan Paegle, Member **15 July 2014** Date Approved

Lawrence Dunn, Member **15 July 2014** Date Approved

and by **Kevin D. Perry**, Chair/Dean of

the Department/College/School of **Atmospheric Sciences**

and by David B. Kieda, Dean of The Graduate School.

ABSTRACT

This dissertation examines Weather Research and Forecasting (WRF) simulations of Great Salt Lake Effect (GSLE) precipitation. An evaluation of banded and nonbanded GSLE-event simulations shows that WRF has low skill predicting GSLE precipitation. An object-based verification method is used in this evaluation to quantify a precipitation bias that contributes to WRF models' low skill. We also analyze WRF simulations of the 27 October 2010 banded GSLE event to evaluate the sensitivity of precipitation prediction to the choice of microphysics parameterization (MP).

WRF simulations of 11 banded and eight nonbanded GSLE events are evaluated with subjective, traditional, and object-based verification. Subjectively, a majority of simulations of banded GSLE events produce realistic precipitation features, whereas a majority of simulations of nonbanded GSLE events do not. Simulations of both banded and nonbanded GSLE events record low equitable threat scores, but simulations of banded GSLE events outperform simulations of nonbanded events. Verification using the Method for Object-based Diagnostic Evaluation (MODE) developed by Davis et al. shows that simulations of banded and nonbanded GSLE events exhibit a southward (rightward and downstream relative to the flow) bias in event total precipitation location that limits forecast skill.

WRF simulations of the 27 October 2010 GSLE event are sensitive to the choice of MP. Precipitation simulated using the Thompson MP scheme (THOM) verifies best against radar-estimated precipitation and gauge observations. The Goddard, Morrison, and WRF double-moment 6-class (WDM6) schemes produce more precipitation than THOM, with WDM6 producing the most. Analyses of hydrometeor mass tendencies show that WDM6 creates more graupel and total precipitation than the other schemes and indicate that the rate of graupel and snow production can strongly influence the precipitation efficiency in simulations of lake-effect storms.

These results show that significant improvements in deterministic model skill and/or the use of an ensemble approach are necessary to improve the reliability of GSLE simulations. Improved deterministic model skill will likely require observations of GSLE hydrometeor characteristics to improve MP, while rectifying the southward (rightward and downstream relative to the flow) precipitation location bias is crucial for deterministic and ensemble forecasting success.

TABLE OF CONTENTS

Chapters

ACKNOWLEDGEMENTS

I would first like to acknowledge my wife, Jennifer, without whom this work would not be possible. I also thank my children, Lily and Connor, for inspiring me to always work towards a better tomorrow.

This work was conducted in pursuit of a Doctor of Philosophy degree with valuable input provided by committee members Jim Steenburgh, Larry Dunn, Steven Krueger, Jan Paegle, and Zhaoxia Pu. I gratefully acknowledge the provision of data sets, software, and/or computer time and services provided by National Climatic Data Center, National Centers for Environmental Prediction, National Center for Atmospheric Research, Unidata, the University of Wyoming, and the University of Utah Center for High Performance Computing. This dissertation is based in part on work supported by the National Science Foundation under Grant Nos. AGS-0938611 and AGS-1262090 and the National Oceanic and Atmospheric Administration/National Weather Service C-STAR program under Grant No. NA13NWS5680003. Any opinions, findings, and conclusions or recommendations expressed in this dissertation are those of the authors and do not necessarily reflect those of the National Science Foundation or the NOAA/National Weather Service. The author gratefully acknowledges the support of the U.S. Air Force Institute of Technology (AFIT) program. The views expressed in this dissertation are those of the author and do not reflect the official policy or position of the U.S. Air Force, Department of Defense, or the U.S. Government.

CHAPTER 1

INTRODUCTION

1.1 Motivation

The Great Salt Lake (GSL) of northern Utah causes lake-effect snowstorms that occur on average 13 times per cool season and may cause significant snow accumulations and reductions in visibility that impact the population living in the lowlands to the south and east of the lake such as the Salt Lake Valley (Fig. 1.1; Carpenter 1993; Steenburgh et al. 2000; Alcott et al. 2012; Yeager et al. 2013). Forecasts of Great Salt Lake-effect (GSLE) events generated by operational and locally run real-time modeling systems at grid spacings of 4-km or less have proven somewhat unreliable in practice for predicting the occurrence, intensity, and location of these snowstorms (R. Graham, National Weather Service, personal communication, 2013). The frequent occurrence and large societal impact caused by GSLE are motivation to improve the currently limited numerical weather prediction (NWP) forecasting skill.

Ocean-, sea-, and lake-effect precipitation events (hereafter referred to as lake effect) similar to GSLE, affect many locations around the globe. Lake effect has been studied extensively in North America in vicinity of the Laurentian Great Lakes (hereafter referred to as the Great Lakes) (e.g., Mitchell 1921; Petterssen and Calabrese 1959; Williams 1963; Peace and Sykes 1966; Niziol 1987; Niziol et al. 1995). Lake effect is also well documented in western Japan where cold air flowing off of the Asian continent crosses over the Sea of Japan during the winter monsoon (Estoque and Ninomya 1975; Ohigashi and Tsuboki 2005; Takemi et al. 2009). Juga (2010) highlighted the road hazards in Finland caused by lake-effect snow, and Andersson and Nilsson (1990) described lake-effect snowfall over Sweden. Cha et al. (2011) modeled the sensitivity of lake-effect precipitation impacting South Korea to the choice of sea surface temperature data over the Yellow Sea. Kindap (2010) documented a lake-effect event caused by the Black Sea that produced significant snowfall over Istanbul in 2005. Recent work has proven that lake effect can also occur downstream of smaller lakes such as the Finger Lakes in New York and Lake Champlain (Laird et al. 2009, 2010). Understanding the performance of NWP forecasts of GSLE will enhance our understanding of lake effect forecasting in northern Utah and in these other diverse locations around the globe.

1.2 Background

1.2.1 Lake Effect Phenomenology

Lake effect is a convective phenomenon that occurs when cold air flows over a relatively warm body of water. Sensible and latent heating of the boundary layer by the lake surface prime the atmosphere for convection while boundary layer and mesoscale circulations (e.g., land breezes) influence the convective morphology (Peace and Sykes 1966; Estoque and Ninomya 1975; Passarelli and Braham 1981; Niziol 1987; Niziol et al. 1995). Early documentation of lake effect comes from Lake Michigan where C. L. Mitchell noted snow flurries over the eastern shore of Lake Michigan in westerly winds, but a lack of snow over the western shore. Mitchell (1921) used observations made by ship captains to deduce that the relatively warm lake surface destabilized the air above the lake to the point where convection was initiated, generating clouds and eventually snow flurries. Subsequent observational and theoretical work documented mesoscale circulations induced by a warm lake surface within a cold airmass (Petterssen and Calabrese 1959; Williams 1963). Peace and Sykes (1966) produced a detailed mesoscale analysis of a shoreline parallel snowband over Lake Ontario to show that sensible heating over the lake surface triggered the snowband and created a mesoscale convergence zone over the lake. Magono et al. (1966) compared Siberian and Japanese upper air soundings to show that the relatively warm Sea of Japan destabilized the airmass flowing from Asia, causing lake-effect snow over Western Japan.

1.2.2 The Great Lakes

1.2.2.1 Climatology

The winter precipitation climatology in the vicinity of the Great Lakes is remarkable, with areas over the eastern portions of the lakes and adjacent land areas receiving 50% to 100% more precipitation from lake-effect storms than from non-lake-effect storms (Scott and Huff 1996). Lake effect is so significant to precipitation in the Great Lakes region because synoptic conditions conducive to lake effect occur on 48% of the days between November and March (Ellis and Leathers 1996). 48% of snowfall events near Lake Michigan over a two cool-season period were lake-effect events, indicating a high likelihood of lake effect occurrence when synoptic conditions are conducive to lake effect (Kelly 1986).

1.2.2.2 Synoptic Conditions

A 13° C lake–850-hPa temperature difference is required to destabilize the cold air overrunning the lake surface, initiate convection, and create lake-effect precipitation over the Great Lakes (Niziol 1987). In addition, there must be sufficient depth beneath any inversion for convection to initiate condensation and produce precipitation. The inversion height is frequently 1–2 km above the surface, with heights above 3 km producing the most intense lake effect precipitation (Niziol 1987). Directional wind shear can be detrimental to lake effect with shear greater than 60° associated with only weak flurries and scattered clouds (Niziol 1987). Another consideration for lake effect occurrence over the Great Lakes is upstream moisture, which affects the intensity and development of lake effect (Kristovich and Laird 1998). Observational case studies over Lake Michigan found that the lake–land temperature difference initiated a land breeze and caused convergence over the lake resulting in a self-sustaining mesoscale circulation (Passarelli and Braham 1981).

1.2.2.3 Convection Morphology

Lake-effect convection over the Great Lakes can organize into three basic morphologies (Niziol et al. 1995; Laird et al. 2003a,b): 1) widespread wind-parallel bands, 2) a solitary shoreline or midlake wind-parallel band, and 3) mesoscale vortices. Widespread wind-parallel bands are associated with short fetches[1] when winds blow perpendicular to the long axis of a lake, while the solitary band morphology is more

---

[1] Fetch is the distance wind travels over the surface of a body of water.

likely when the wind is parallel to the long axis of a lake. Finally mesoscale vortices tend to occur under weak wind conditions (Niziol et al. 1995).

A proposed control of lake-effect morphology over the Great Lakes is the ratio of wind speed, U, to fetch, L, defined as: U/L (Laird et al. 2003a,b). Laird et al. (2003a,b) produced several idealized simulations and found threshold values of U/L that predicted the lake-effect morphology. However, U/L from several observed lake-effect events did not match U/L values from the idealized experiments implying the parameter has limited skill at predicting lake-effect morphology (Laird and Kristovich 2004).

1.2.2.4 Simulations

Modeling studies have reinforced the observationally discovered synoptic conditions required for lake effect over the Great Lakes. The lake-land temperature difference is the dominant required condition; some simulations have been run without any moisture and/or latent heat release and have still recreated circulations similar to those seen in lake effect events (Lavoie 1972; Hjelmfelt and Braham 1983; Pease et al. 1988; Hjelmfelt 1990; Laird et al. 2003a,b). Latent heat release, the presence of a capping inversion, lapse rate, upstream moisture, wind speed, fetch, and lake-ice cover have all been shown by simulations to impact the intensity and/or morphology of lake-effect precipitation (Hjelmfelt and Braham 1983; Hjelmfelt 1990; Laird et al. 2003a,b; Cordeira and Laird 2008; Wright et al. 2013). Simulations have also been used to show that terrain downstream of Lake Michigan causes a localized increase in lake-effect precipitation (Hjelmfelt 1992).

1.2.3 Japan

1.2.3.1 Climatology And Synoptic Conditions

Lake effect during the winter monsoon contributes to a sharp contrast in climatological snowfall amount from the Sea of Japan coast to the Pacific coast of Japan. The coastal lowlands nearest the Sea of Japan receive a mean annual maximum snow depth greater than 1 m, while the Pacific coastal lowlands receive half as much (Tadashi 1977; Mizukoshi 1977; Yoshino 1977). Comparing Siberian and Japanese upper-air soundings proved that the relatively warm Sea of Japan destabilizes and moistens cold airmasses flowing from Siberia towards Japan, causing lake-effect snow (Magono et al. 1966). Magono et al. (1966) also noted riming on snow crystals and graupel near the coast under convective cloud tops, while inland no riming or graupel is observed, and the clouds tops are more diffuse and smooth, highlighting the convective nature of the lake-effect cloud systems.

1.2.3.2 Convection Morphology

Lake effect over the Sea of Japan is sometimes organized, with the heaviest precipitation caused by wind parallel and/or wind perpendicular mesoscale bands that arise from thermally distinct Siberian airstreams, convergence downstream of terrain on the Asian continent, and/or a frontal structure along the Japanese coast (Hozumi and Magono 1984; Fujiyoshi et al. 1998; Yoshimoto et al. 2000; Ohigashi and Tsuboki 2007; Ohtake et al. 2009).

1.2.3.3 Orographic Effects

Lake effect convection over the Sea of Japan is advected onshore in northern Japan and snow falls in one of two patterns “satoyuki,” lowland snowfall, or “yamayuki,” mountain snowfall (Magono et al. 1966). Satoyuki is not influenced by orography at all, whereas yamayuki occurs when the lake-effect band rises over steep terrain generating snow on the windward slopes (Magono et al. 1966; Saito et al. 1996). Saito et al. (1996) simulated yamayuki with a 2D model to show that increasing cloud top height, decreasing cloud top temperature, and increasing number density of cloud ice as the convective elements move onshore lead to increased precipitation over the windward slope.

1.2.4 Small Lakes

Lake effect over the relatively small Finger Lakes of New York and Lake Champlain are also caused by relatively warm lake water destabilizing and moistening an overlying cold airmass (Payer et al. 2007; Laird et al. 2009, 2010). On these small lakes the fetch becomes more important, and lake effect is most frequently seen when the wind direction is aligned with the lake’s long axis (Payer et al. 2007; Laird et al. 2009; Alcott et al. 2012). Laird et al. (2009) also showed that the land breeze circulation and orographically forced convergence are significant contributors to lake-effect precipitation over small lakes.

1.3 The Great Salt Lake

1.3.1 Environs

The GSL is relatively small in comparison to any of the Great Lakes with an average surface area of 4,400 km^2. The lake is hypersaline with differing salt contents in its main body (~11%) and northern arm (~28%) (USGS 2013). The salinity reduces the rate of evaporation possible from the lake compared with fresh water and has a negative impact on GSLE precipitation (Steenburgh and Onton 2001). The longest fetch over the GSL is possible when the wind is from 325° and varies from ~120 to 135 km [record minimum to record maximum lake elevations and extents] (Alcott et al. 2012). Mountains surround the GSL, rising significantly above the 1280 m MSL median lake surface level (USGS 2013). To the northwest lie the Raft River Mountains of the Jarbidge-Caribou Highlands, and to the north the Promontory Mountains form a peninsula that juts into the lake. To the east are the Wasatch Mountains, while south of the lake are the Stansbury and Oquirrh Mountains (Fig. 1.1). The location and elevation of these ranges influence the meteorological conditions associated with lake-effect snow (Alcott and Steenburgh 2013).

1.3.2 Climatology

GSLE snowstorms occur several times a year, can reduce visibilities to below ¼ mi (400 m) at Salt Lake City International Airport, and have produced up to 129 cm of lowland snowfall (Carpenter 1993; Steenburgh et al. 2000; Alcott et al. 2012; Yeager et al. 2013). The peak frequencies of GSLE storms occur in the fall and spring when the lake is relatively warm compared to the overlying airmass (Alcott et al. 2012). GSLE events exhibit a diurnal pattern that favors formation overnight and dissipation a few hours after sunrise when the air above the surrounding land surface warms and the lake–land temperature contrast is diminished (Alcott et al. 2012). From a hydrological perspective, mean GSLE precipitation contributes at most an average of 8.4% of the total mean cool season snow water equivalent (SWE) in the GSL basin; however, intense GSLE events can contribute a much larger fraction of total cool season SWE (Yeager et al. 2013).

1.3.3 Synoptic Conditions

The first documented climatology of GSLE found the 700-hPa flow to be useful in predicting the potential occurrence as well as the location of the heaviest snow and noted a lake–700-hPa temperature difference of at least 17° C in the heaviest events (Carpenter 1993). Steenburgh et al. (2000) expanded on Carpenter's climatology and found a lake–700-hPa temperature difference of at least 16° C in GSLE events. Steenburgh et al. (2000) also noted low-level convergence over the GSL during GSLE periods, an absence of capping inversions or stable layers below 700 hPa during GSLE periods, and weak (< 60°) steering-layer (800–600 hPa) directional shear (except when the flow is weak).

An additional climatological study found GSLE could occur at lake–700-hPa temperature differences of as little as 12.4° C and that a minimum temperature difference derived from a curve fit to the climatological minimum lake–700-hPa temperature difference was better than a fixed temperature threshold (Alcott et al. 2012). Alcott et al. (2012) also revealed the importance of the land breeze in GSLE events by finding that

GSLE only occurred when the lake temperature was higher than the temperature of surrounding stations on the shore.

1.3.4 Convection Morphology

Three distinct morphologies of convection have been recorded in GSLE snow events (Steenburgh et al. 2000; Alcott et al. 2012):

1) Banded GSLE is a solitary shoreline- and wind-parallel snowband along the major (northwest to southeast) axis of the lake [similar to midlake bands described by Hjelmfelt (1990) and the Type I band described by Niziol (1995)].

2) Nonbanded GSLE occurs over a broad area with little organization over the GSL.

3) Mixed-mode GSLE is primarily nonbanded with some banded features.

Nonbanded GSLE is the dominant morphology (occurring 54% of the time during GSLE events), whereas the banded morphology occurs only 20% of the time (Alcott et al. 2012). Calculations of the parameter, *U/L*, for GSLE events showed some utility in predicting banded GSLE, but there was significant overlap in *U/L* values in banded and nonbanded GSLE events (Alcott et al. 2012).

1.3.5. Orographic Effects

Terrain is a factor for GSLE events as shown in two cases, 7 December 1998 and 27 October 2010 (Onton and Steenburgh 2001; Alcott and Steenburgh 2013). Simulations of the 7 December 1998 case produced GSLE when the model was run with and without local terrain, proving that the lake generated the GSLE, but the forecast with terrain did increase the intensity of precipitation (Onton and Steenburgh 2001). A similar experiment (simulations with local terrain or with flat terrain) conducted on the 27 October 2010 case showed that GSLE did not occur when the terrain around the lake was flat, revealing a continuum of mesoscale forcing where GSLE is caused by the thermodynamic forcing from the lake, the kinematic forcing of orography, and/or synergistic interaction between the two (Alcott and Steenburgh 2013).

1.3.6 Simulations

GSLE events have been successfully simulated and examined using NWP models. Steenburgh and Onton (2001) and Onton and Steenburgh (2001) used the Pennsylvania State University–National Center for Atmospheric Research fifth generation Mesoscale Model to illustrate the importance of thermally driven circulations in producing GSLE events. More recently, Alcott and Steenburgh (2013) used the Advanced Research core of the Weather Research and Forecasting (WRF) model to reveal a strong synergy between processes associated with the GSL and the surrounding orography in creating GSLE snowfall during some events. Despite simulating these cases with some fidelity, these studies noted errors in the simulated timing, location, and amount of precipitation that could prove problematic for operational forecasting (Steenburgh and Onton 2001; Onton and Steenburgh 2001; Alcott and Steenburgh 2013). In addition, GSLE forecasts generated by operational and locally run real-time modeling systems at grid spacings of 4-km or less have proven somewhat unreliable in practice (R. Graham, National Weather Service, 2013, personal communication).

1.4 Numerical Weather Prediction

1.4.1 Microphysics

The microphysics parameterization (MP) used by an NWP model is a critical aspect of GSLE simulation. Most MPs used for mesoscale modeling are bulk schemes that predict hydrometeor mass mixing ratios and/or number concentrations but assume hydrometeor size distributions based on empirical exponential or gamma distributions (e.g., Lin et al. 1983; Tao et al. 1989; Ferrier 1994; Thompson 2008; Milbrandt and Yao 2005; Morrison et al. 2009; Lim and Hong 2010; Lin and Colle 2011). Single-moment MP schemes predict the mass of hydrometeors, whereas dual-moment schemes predict the mass and number concentration of hydrometeors. Some MP schemes are hybrids, meaning that some hydrometeors are handled as single moment while others are handled as dual moment. Increasing the number of predicted moments has been shown to improve precipitation, the evolution of simulated convective systems, and orographic precipitation (Morrison et al. 2009; Lim and Hong 2010; Milbrandt et al. 2010; Van Weverberg 2012). The inclusion of ice hydrometeors (e.g., cloud ice, snow, graupel, hail) improves simulations of squall lines and supercells (Nicholls 1987; Fovell and Ogura 1988; Tao and Simpson 1989; Szeto and Cho 1994; Liu and Moncrieff 2007; Adams-Selin et al. 2013), and differences in the parameterization of ice behavior influence the accuracy of surface precipitation forecasts (Rutledge and Hobbs 1983; Thompson et al. 2004). Since differences in MP components can cause different simulation outcomes, it is not surprising that simulations of orographic precipitation, Arctic mixed-phase stratus, and squall lines are sensitive to the choice of MP (Colle and Mass 2000; Gilmore et al. 2004; Morrison and Pinto 2005; Lim and Hong 2010; Lin and

Colle 2011; Liu et al. 2011; Morrison and Milbrandt 2011; Bryan and Morrison 2012).

Simulations of cool-season precipitation are also sensitive to the choice of MP scheme. The Thompson scheme (THOM; Thompson 2008) and Morrison scheme (MORR; Morrison et al. 2009) were found to produce superior results when simulating winter season basin-scale snow over Colorado compared to the WRF Single-Moment, 5-Class (WSM5; Hong and Lim 2006), WRF Single-Moment, 6-Class (WSM6; Hong and Lim 2006), WRF Double-Moment, 6-Class (WDM6; Lim and Hong 2010), Goddard (GODD; Tao et al. 1989), and Purdue Lin (Chen and Sun 2002) schemes (Liu 2011). The relatively high snow amounts, high cloud liquid water, and low graupel amounts in temporally and spatially averaged profiles of hydrometeors shown by THOM and MORR are credited with creating accurate surface precipitation patterns, while schemes with high amounts of graupel and low amounts of cloud water (WSM5, WSM6, WDM6, Purdue Lin) produce the worst surface precipitation (Liu 2011). THOM also skillfully simulated the 27 October 2010 GSLE event (Alcott and Steenburgh 2013). On the other hand, in polar low convection simulations, WSM6 produced cloud fields, maximum precipitation rates, and hydrometeor fields that were consistent with observations, while THOM, MORR, GODD, and Purdue-Lin all performed poorly predicting the polar low (Wu and Petty 2010).

There is some recent work examining the impact of MP selection on lake-effect precipitation forecasts. Theeuwes et al. (2010) compared the results of a Lake Erie lake-effect simulation produced by the WRF with two different MP schemes and found differences in the locations and patterns of the forecast precipitation. The more complex THOM scheme performed poorly compared to WRF Single-Moment, 3-Class (WSM3, Hong et al. 2004) by underforecasting precipitation and by producing precipitation 4 hours later than WSM3 (Theeuwes et al. 2010). Sensitivity of quantitative precipitation forecasts to the choice of MP in WRF over Lake Ontario has also been shown (Reeves and Dawson 2013). Two forecast regimes were found: a steady regime that is characterized by broad precipitation shields, lower maximum precipitation amounts, longer downstream transport of hydrometeors, and uniform hourly precipitation rates and an unsteady regime that is characterized by narrower precipitation distribution, higher precipitation maxima, and unsteady hourly precipitation. The differences in regime arose from differing assumptions of the MP schemes that result in higher graupel content in the simulations of the unsteady regime. The MP schemes in the steady regime are GODD, THOM, MORR, SBYULIN, while the unsteady regime included the WSM6, WDM6, MY, and Ferrier MP schemes (Reeves and Dawson 2013).

1.4.2 Grid Spacing

NWP grid spacing is also a significant consideration in simulations of GSLE. Some current operational models operate with grid spacings of **O**(1 km). This grid spacing allows the simulation to explicitly resolve the largest circulations in a given convective element and is considered *convection permitting* (Weisman et al. 1997; Bryan et al. 2003; Langhans et al. 2012). The use of convection-permitting grid spacing allows the modeler to neglect the cumulus parameterization (Stensrud 2007) and is proven to adequately resolve mesoscale forcings in complex terrain that are important to GSLE (Steenburgh and Onton 2001; Garvert et al. 2005; Colle et al. 2008; Alcott and Steenburgh 2013). Furthermore, convection-permitting GSLE simulations at 1.33 km grid spacing have generated convective updrafts within GSLE snowbands (Alcott and Steenburgh 2013).

From a turbulence perspective, convection generated in convection-permitting simulations does not resolve an inertial subrange (Bryan et al. 2003). Bryan et al. (2003) showed that the inertial subrange is not explicitly resolved until grid spacing is reduced to **O**(100m). Therefore, simulations run at grid spacings **O**(100m) are considered *convection resolving*. Convection-resolving simulations have revealed different modes of convective overturning that were unseen in simulations at coarser grid spacings and produced improved simulations of convection (Petch 2001, 2002; Stevens et al. 2002; Bryan et al. 2003). Convection-resolving simulations of GSLE are so far untested, but it may be that decreasing grid spacing to convection-resolving grid spacing is necessary to more accurately simulate GSLE.

1.4.3 Verification

Verification of NWP models fulfills administrative, scientific, and economic requirements (Brier and Allen 1951). Wilks (2006) notes that the administrative category includes monitoring the performance of a model over time or providing a consistent comparison between models for the same event.

Convection-permitting NWP is particularly difficult to verify because of the different scales of phenomena represented in the forecast and observational data sets used for verification. Subjective evaluation of simulations at convection-permitting grid spacings is generally positive with many authors noting the ability of the simulations to produce more realistic precipitation structures than at coarser grid spacings (e. g., Mass

2002; Colle et al. 2003; Kain et al. 2003; Weisman et al. 2008; Duda and Gallus 2013). The studies of warm season convection that find precipitation structures to be realistic note timing errors **O**(1h) and location errors **O(**100 km) (Weisman et al. 2008; Duda and Gallus 2013). Unfortunately, positive subjective verification does not necessarily mean that a simulation will also achieve positive objective verification measures and furthermore, subjective evaluation is not used to influence model improvement or development (Kain et al. 2003).

Objective verification of precipitation typically compares forecast and observation pairs from a yes/no perspective. To do this, various statistics based on these yes/no pairs are computed (Wilks 2006). One such measure is the equitable threat score (ETS) (Wilks 2006) also known as the Gilbert skill score (Gilbert 1884). Various numerical weather prediction models have achieved ETS scores ranging between 0.1 and 0.3 for short-term warm-season precipitation forecasts, which are not very skillful considering a perfect forecast would score 1.0 and a forecast with no skill above chance scores 0.0 (Mesinger 1996; Gallus 2002; Gallus et. al. 2005; Wilks 2006; Aligo et al. 2009; Clark et. al. 2010; Stratman et al. 2013). Similarly, Colle et al. (1999) found an ETS range of 0.1– 0.3 for cool-season precipitation forecasts in the Pacific Northwest. Hamill et al. (2013) reported ETS scores ranging from less than 0.1 to 0.5 depending on precipitation threshold from January–March 2011 across the continental United States.

Objective skill scores tend to penalize convection-permitting forecasts for small timing and placement errors (Mass et al. 2002; Ebert 2009) and do not include information the modeler or forecaster can use to understand and/or correct model errors (Davis et al. 2006a). Object-based verification approaches aim to reduce the penalties for high-resolution forecasts that arise from objective approaches and provide additional information about what aspect of the model affects the skill of a simulation (e.g., Ebert and McBride 2000; Nachamkin 2004, 2009; Nachamkin et al. 2005; Marzban and Sandgathe 2006, 2008; Marzban et al. 2008; Wernli et al. 2008, 2009; Ebert and Gallus 2009; Gallus 2010). The Method for Object-based Diagnostic Evaluation (MODE) is one such approach that attempts to objectively identify objects in the forecast and observations that a human forecaster would identify as significant (Davis et al. 2006a,b, 2009).

1.5 Objectives and Outline

The objectives of this dissertation are to benchmark WRF performance in GSLE simulations, determine if nonbanded GSLE events can be predicted by WRF, to determine what aspects of WRF simulations hinder forecast skill, and to examine WRF sensitivity to MP choice in GSLE simulations. To meet these objectives, subjective and traditional verification of WRF model simulations of 11 banded and eight nonbanded GSLE events are presented to show WRF's ability to simulate GSLE in general, WRF's ability to simulate both banded and nonbanded GSLE morphologies, and to serve as a benchmark for future GSLE modeling. Object-based verification is also presented to reveal what factors are responsible for errors in WRF GSLE simulations. In addition, we show how and why the choice of MP in NWP models affects quantitative GSLE precipitation forecasts at convection-permitting grid spacings by simulating GSLE with six MP schemes: THOM, WDM6, Milbrandt two-moment (MY; Milbrandt and Yao 2005), GODD, Stonybrook University Lin (SBYULIN; Lin and Colle 2011), and MORR.

Chapter 2 describes verification results from WRF simulations of banded and nonbanded GFSLE events. Chapter 3 documents the sensitivity of WRF simulations of GSLE to the choice of MP. Chapter 4 will present conclusions reached by this dissertation and the possibilities for future work including recommendations for additional verification, the need for microphysical observations, updated GSLE climatology, and further modeling studies. Appendix A describes possible factors that may contribute to variation in GSLE band placement.

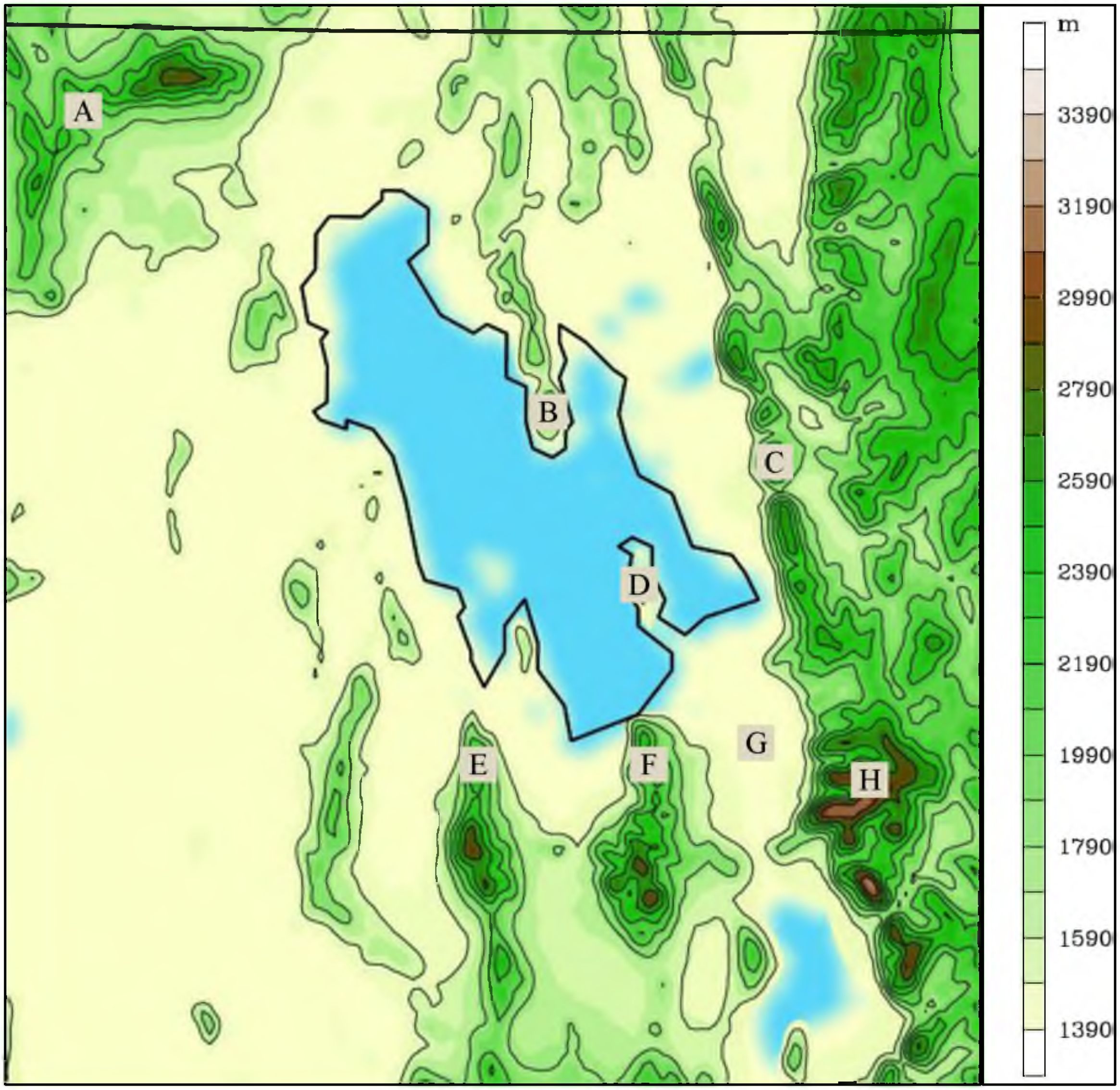

Fig. 1.1 Map of major geographic features including the Raft River Mountains (A), Promontory Mountains (B), northern Wasatch Mountains (C), Antelope Island (D), Stansbury Mountains (E), Oquirrh Mountains (F), Salt Lake Valley (G), and central Wasatch Mountains (H). Elevation (m) contoured and shaded following scale at right.

CHAPTER 2

VALIDATION OF NUMERICAL SIMULATIONS OF BANDED AND NONBANDED LAKE-EFFECT SYSTEMS OVER THE GREAT SALT LAKE

2.1 Abstract

The Advanced Research core of the Weather Research and Forecasting (WRF) model can produce physically realistic banded Great Salt Lake-Effect (GSLE) precipitation structures, but the skill of these simulations has not been quantified. The ability of the WRF to simulate nonbanded GSLE events is also unknown. In this chapter we use subjective, traditional, and object-based verification approaches to evaluate convection-permitting WRF simulations of 11 banded and 8 nonbanded GSLE events. Subjectively, a majority of the simulations of banded GSLE events produce physically realistic precipitation features. In contrast, simulations of nonbanded GSLE events rarely produce physically realistic precipitation features and sometimes erroneously produce banded precipitation features. Traditional contingency table statistics reveal low skill in all 19 simulations, but simulations of banded GSLE events produce Equitable Threat Scores (ETS) comparable to other convective verification studies, whereas simulations of nonbanded events produce lower ETS than simulations of banded events. In addition, analysis of data from the Method for Object-based Diagnostic Evaluation (MODE)

developed by Davis et al. (2006a,b) shows that simulations of banded and nonbanded GSLE events exhibit a southward (rightward and downstream relative to the flow) bias in precipitation location that limits forecast skill. The inability of the optimally configured and initialized WRF to simulate GSLE events with an appreciable level of skill reveals low GSLE predictability in convection-permitting simulations.

2.2 Introduction

Predicting Great Salt Lake-Effect (GSLE) precipitation is a significant challenge for forecasters in Northern Utah (Carpenter 1993). This challenge may arise from the inherently low predictability of convective systems and the small-scale phenomena that influence mesoscale precipitation (Lorenz 1982; Anthes 1986; Stamus et al. 1992; Emanuel 1994; Mullen et al. 1999). Alternatively, forecasting may be difficult because GSLE storms are sensitive to many environmental parameters (atmospheric moisture, lake temperature, vertical wind shear, etc.), some of which are poorly observed and/or simulated (Onton and Steenburgh 2001; Steenburgh and Onton 2001; Alcott et al. 2012). In either case, GSLE forecasts generated by operational Numerical Weather Prediction (NWP) models at convection-permitting grid spacings (4-km or less) appear to be somewhat unreliable in practice (R. Graham, National Weather Service, personal communication, 2013).

Research simulations at convection-permitting grid spacings, however, subjectively produce physically realistic GSLE precipitation structures (Steenburgh and Onton 2001; Onton and Steenburgh 2001; Alcott and Steenburgh 2013). Similar results are found for other types of precipitation systems (e.g., Mass et al. 2002; Colle et al.

2003; Kain et al. 2003; Weisman et al. 2008; Duda and Gallus 2013). In these simulations, errors in timing, position, and intensity frequently overshadow the physically realistic appearance of precipitation structures. For example, physically realistic warm-season precipitation forecasts sometimes produce timing errors **O** (1 h) and location errors **O** (100 km) (Weisman et al. 2008; Duda and Gallus 2013).

Traditional precipitation verification often compares forecast and observation pairs by constructing a 2x2 contingency table of all possible forecast and observed yes/no counts from which statistics and skill scores are derived (Fig. 2.1; Wilks 2006). One traditional verification score is the equitable threat score (ETS; Wilks 2006). Typical ETS values for short-range (<36 h) forecasts of warm-season precipitation generated at 4-km grid spacing are 0.1–0.3 (e.g., Gallus 2002; Aligo et al. 2009; Schwartz et al. 2009; Clark et al. 2010, Stratman et al. 2013). Colle et al. (2000) found ETS of 0.15–0.35 for Pacific Northwest cool-season precipitation forecasts with 6-h lead time at 4-km grid spacing. ETS values from simulations of atmospheric rivers over California at 3-km grid spacings and lead times of 48 hours or less range from 0.25–0.45 (Jankov et al. 2009). Finally, Hart et al. (2005) assessed 12–36 h cool-season precipitation simulations at 4-km grid spacing during the 2002 Olympic and Paralympic Winter Games over northern Utah and found ETS ranging from 0.1–0.4.

Traditional verification scores and trends guide model improvement (Kain et al. 2003), but do not provide information to aid the modeler or forecaster in understanding the causes of errors (Davis et al. 2006a). They also penalize convection-permitting forecasts for small timing and placement errors (Mass et al. 2002; Ebert 2009). To overcome these drawbacks, a variety of object-based approaches have been developed (e.g., Ebert and McBride 2000; Nachamkin 2004, 2009; Nachamkin et al. 2005; Marzban and Sandgathe 2006, 2008; Marzban et al. 2008; Wernli et al. 2008, 2009; Ebert and Gallus 2009; Gallus 2010). The Method for Object-based Diagnostic Evaluation (MODE) developed by Davis et al. (2006a,b, 2009) attempts to objectively identify and characterize precipitation objects that a human forecaster would consider significant. Object characteristics, called attributes in MODE, are quantified and can be used to identify errors that contribute to poor traditional verification scores. In the case of GSLE precipitation, these object attributes can reveal information about how well the simulations represent different GSLE morphological features and identify possible sources of model error.

GSLE occurs in three distinct morphologies: banded [as defined by Alcott et al. (2012), a.k.a. shoreline bands (Laird et al. 2003a,b; Laird and Kristovich 2004) or midlake bands (Steenburgh et al. 2000)], nonbanded, and mixed mode [when banded and nonbanded features occur simultaneously (Alcott et al 2012)]. However, research simulations of GSLE have focused only on banded events (Onton and Steenburgh 2001; Steenburgh and Onton 2001; Alcott and Steenburgh 2013), despite the fact that nonbanded events are more common (Alcott et al. 2012). These research simulations produced precipitation features and precipitation distributions that subjectively match observations, but their accuracy and reliability remains unquantified. In addition their ability to produce nonbanded GSLE features is unknown.

In this chapter we evaluate the fidelity of Weather Research and Forecast (WRF) model simulations of banded and nonbanded GSLE events using subjective, traditional, and object-based verification. To stack the deck, the simulations use analyzed rather than forecast lateral boundary conditions, which reduces (but does not eliminate) the influence of large-scale error growth on model skill. The data and methods used are described in section 2.3. In section 2.4 we show that WRF has little skill simulating GSLE in general, but more skill simulating banded versus nonbanded events. We use MODE to quantify the tendency in WRF to displace precipitation southward (rightward and downstream relative to the flow) in all simulations. We conclude with a discussion of our findings and implications for operational forecasting and model development in section 2.5.

2.3 Data and Methods

2.3.1 Event Selection

Using lowest-tilt (0.5°) radar reflectivity imagery from the Weather Surveillance Radar-1988 Doppler (WSR–88D) at Promontory Point, Utah (KMTX; Fig. 2.2), we identified and classified GSLE events during the 2006/07–2012/13 cool seasons (16 September–15 May) following the approach of Alcott et al. (2012). The radar data were obtained from the National Climatic Data Center Hierarchical Data Storage System in level III format (Crum et al. 1993). The study period was chosen to ensure model initialization analyses were from a common dynamic core [the WRF nonhydrostatic mesoscale model core used by the North American Mesoscale (NAM) model starting 20 June 2006]. Since GSLE can occur concurrently with synoptic precipitation or other non-lake-effect precipitation features (Alcott et al. 2012), we selected 11 primarily banded and eight primarily nonbanded GSLE events (Table 2.1). We also omit mixed-mode events that feature both banded and nonbanded characteristics to highlight differences between banded and nonbanded GSLE morphologies.

2.3.2 Numerical Simulation

The Advanced Research core of the WRF model version 3.5.1 (Skamarock and Klemp 2008) was used to simulate the 11 banded and eight nonbanded GSLE events. Following Alcott and Steenburgh (2013) we configure the WRF with three one-way nested domains with 12-, 4-, and 1.33-km grid spacings. The outer domain encompasses the western United States, the 4-km domain stretches from central Nevada to western Colorado and from the Snake River Plain to southern Utah, and the inner domain covers most of the Great Salt Lake (GSL) basin and surrounding region (Fig. 2.2). All simulations use the Yonsei University planetary boundary layer parameterization (Hong et al. 2006), the Rapid Radiative Transfer Model longwave and shortwave radiation parameterizations (Iacono et al. 2008), the Noah land surface model (Chen and Dudhia 2001), and the Thompson et al. (2008) microphysics parameterization scheme on all three domains. We use the Kain-Fritsch 2 cumulus parameterization (Kain 2004) on the outer two domains, but neglect the cumulus parameterization in the 1.33-km domain to avoid precipitation sensitivity to cumulus parameterization choice (e.g., Jankov et al. 2005).

All simulations are cold-start initialized at least 6 hours prior to the first observed GSLE radar features during each event and run for at least 24 h (the longest simulation was 36 h). This allows for appropriate spin up time for the model to represent convective scale processes (Sun et al. 2014) and results in forecast lead times of 6–11.5 h for event onsets and 14.5–32 h for event ends. Initial atmospheric, land-surface, and lateral boundary conditions derive from 6-hourly operational NAM model analyses obtained from the NOAA National Operational Model Archive and Distribution System at 12-km horizontal and 25-hPa vertical grid spacing. The use of NAM analyses for lateral boundary conditions helps to limit large-scale error growth. Thus, the accuracy of the simulations presented here may be somewhat higher than one would expect when lateral boundary conditions are obtained from a model forecast.

The GSL temperature for each case was set to that obtained from the Alcott et al. (2012) lake-temperature climatology. Given a lack of in situ GSL temperature observations and challenges using remotely sensed lake-temperature data, this represents a best estimate of the actual lake temperature in practice, with errors expected to be largest in the spring (Crosman and Horel 2010; Alcott et al. 2012). Nevertheless, this represents an important source of uncertainty for these and real-time forecasts given the sensitivity of GSLE to lake temperature (Onton and Steenburgh 2001). The saturation vapor pressure over the GSL was also adjusted to account for salinity effects following Steenburgh and Onton (2001).

2.3.3 Validation Data Sets

The radar-estimated precipitation (REP) was calculated using a reflectivity–snow-water-equivalent (Z–S) relationship of $Z = 75S^2$ (Rasmussen et al. 2003) applied to 0.5° radar reflectivity data mapped to a 0.005°x0.005° lat-lon grid. Potential sources of error in the REP include the use of a fixed rather than dynamic Z–S relationship, ground-clutter contamination, partial or total beam blockage, sublimation and evaporation below the elevated radar beam (especially over lowland regions), hydrometeor drift, and the partial or total overshooting of shallow precipitation features, especially at longer ranges (Rasmussen et al. 2003; Germann and Joss 2004). To help limit the influence of some of these error sources, the REP from each event was manually quality controlled to remove spurious precipitation amounts caused by recurring reflectivity returns from mountain peaks, traffic along Interstates 15 and 80, and railroad traffic [see Slemmer (1998) for discussion of these nonmeteorological returns].

Quality controlled observations from precipitation gauges were also obtained from the MesoWest cooperative networks (Horel et al. 2002) for model validation. However, the number of observations with fine (0.01 in) data resolution and less than 24-h accumulation periods was very limited and precluded insightful validation of fine-scale precipitation structures. Therefore, analysis of these comparisons is not presented here.

2.3.4 Validation Methodology

Three verification approaches were used to evaluate WRF performance: subjective, traditional, and object-based. Subjective approaches involved the visual comparison of simulated reflectivity and precipitation to observed reflectivity and REP. Emphasis was placed on the occurrence or nonoccurrence of GSLE, GSLE morphology based on precipitation features, and the coverage, locations, and amount of event total precipitation. For traditional verification, WRF simulated precipitation and surface observations were bilinearly interpolated to the REP grid and statistics were generated using the Model Evaluation Tools software suite developed by the National Center for Atmospheric Research. Object-based verification used the MODE tool to compare precipitation objects from WRF and REP data.

2.3.4.1 Traditional Verification

The traditional verification statistics are based on a 2x2 contingency table with precipitation thresholds of 1, 3, 5, 10, and 15 mm (Fig. 2.1). ETS was then calculated following Wilks (2006) where

$$ETS = \frac{HIT - CHANCE}{HIT - CHANCE + FALSE\ ALARM + MISS},$$

and

$$CHANCE = \frac{(HIT + FALSE\ ALARM)(HIT + MISS)}{HIT + MISS + FALSE\ ALARM + CORRECT\ NEGATIVE}.$$

Bias was also calculated following Wilks (2006) where

$$BIAS = \frac{HIT + FALSE\ ALARM}{HIT + MISS}.$$

An ETS of 1 represents a perfect forecast while an ETS less than or equal to 0 shows no skill greater than chance. A bias equal to 1 indicates that there are an equal number of forecasts and observations of precipitation greater than or equal to a given threshold. When the number of forecasts (HIT + FALSE ALARM) is greater than (less than) the number of observations (HIT + MISS) at or above a given threshold, the bias is greater than (less than) 1, indicating overforecasting (underforecasting). We also used a neighborhood method to calculate ETS. The neighborhood method compares the tested grid point against all grid points in a 9, 17, and 33 grid point (5.06, 9.55, and 18.55 km) square stencil centered on the tested grid point. If the tested grid point is forecast at or above a given threshold, a HIT will be recorded if any grid point in the square is observed at or above the threshold, whereas a FALSE ALARM will be recorded if no grid point in the square is observed at or above the threshold. If the tested grid point is not forecast at or above a given threshold, a CORRECT NEGATIVE will be recorded if no grid points in the square are observed at or above the threshold, but a MISS will be recorded if any grid point in the square is observed at or above the threshold.

2.3.4.2 Object-Based Verification

We use MODE to identify WRF precipitation objects and REP objects that are associated with GSLE. MODE processes data in three major steps: 1) identifying objects, 2) measuring attributes of the identified objects, and 3) using a fuzzy-logic algorithm to quantify how similar objects are based on their attributes (Davis et al. 2006a,b; 2009). MODE identifies objects by smoothing the WRF and REP data with a circular convolution function of radius R [we used R = 4 REP grid points (~ 2 km) for both the WRF and REP data]. After convolution, a threshold, T [we used $T \geq 1$ mm to identify all possible GSLE objects and $T \geq 3$ or 5 mm to highlight intense GSLE objects], is applied to the smoothed data leaving a binary data set composed of objects $\geq T$ and values of zero elsewhere. Objects smaller than 100 grid points (~ 32 km^2) were filtered out.

MODE measures the centroid location, aspect ratio, orientation angle, object area, and object boundary attributes to allow for comparisons between WRF and REP objects

(Davis et al. 2006a,b; Davis et al. 2009). The centroid location is the geometric center of the object determined by its boundary. The aspect ratio is the long axis divided by the short axis of a rectangle surrounding the object boundary. The orientation angle is the angle of the long axis of the aspect ratio rectangle relative to east. Positive object angles represent the north of east angle between the long axis and east while negative angles are the south of east angle between the long axis and east. The object area is simply the areal coverage of the object.

MODE quantifies the similarity between WRF and REP objects with a fuzzy-logic algorithm to calculate a value called total interest, *I*, which ranges from 0 to 1, with 0 indicating no match and 1 indicating a perfect match between objects pairs (Davis 2009). *I* is calculated by comparing the WRF and REP object attributes. The attributes compared are centroid separation, minimum object boundary distance, orientation angle difference, object area ratio, and object area intersection. The function for *I* is

$$I_j = \frac{\sum_{i=1}^{M} F_{i,j} w_i c_i}{\sum_{i=1}^{M} w_i c_i},$$

where *I* is the total interest of the *j*th object pair, *F* is the interest function for the *i*th attribute and *j*th object pair, *w* is the weight of the *i*th attribute, *c* is the interest function confidence of the *i*th attribute, and M is the total number of attributes used to compare each object pair. *F* is the primary component of *I* and also varies from 0 to 1, with 0 indicating no match and 1 indicating a perfect match between object pairs [i.e., the *F* for the centroid separation attribute comparison increases as the centroid separation decreases, indicating the objects are a better match]. *w* is set to determine which attributes are most important in the calculation of *I*, with attributes assigned a larger value of *w* contributing more to *I*. *c* ranges from 0 to 1 and is 1 for all attributes except orientation angle and centroid separation that may be ambiguous when objects are spherical or when objects have greatly different areas, respectively.

We made adjustments to several of the components of the total interest function to identify how well GSLE precipitation objects matched. We adjusted *F* for centroid separation and minimum object boundary distance to maximize *I* when objects were close to one another. We also adjusted *F* for object area ratio to maximize *I* when the smaller of the two objects was at least 30 percent of the size of the larger object. We increased *w* for centroid separation and object area ratio to increase the influence of the distance between objects and their relative size on *I*.

2.4 Results

2.4.1 Subjective Verification

We examined the simulated and observed reflectivity at 30-minute increments for the duration of each GSLE event and found that the WRF produced banded precipitation features in seven of the 11 banded GSLE events [20071018, 20080115, 20080411, 20081105, 20101027, 20101231, and 20110427 (Figs. 2.3a,c; 2.4a,b,d; 2.5b,c; we present a mature representative time from each event for brevity)]. The structure and general evolution of the simulated bands appear physically realistic in these seven events, although the simulated band in the 20101231 event developed 6 h late. Displacement of the simulated bands to the south of observed (rightward and downstream relative to the flow) is seen at times in the 20071018, 20080411, 20101027, 20101231, and 20110427 events. Of the four remaining banded events, the WRF produced only weak, disorganized convection over or near the lake in the 20071227 and 20100407 events and no precipitation near the lake in the 20080226 and 20101129 events (Figs. 2.3b,d, 2.4c, and 2.5a).

In contrast, the WRF generated nonbanded GSLE precipitation features in only one of eight nonbanded GSLE events (20061129; Fig. 2.6a) and, for that event, the simulated precipitation feature was south of observed (rightward and downwind relative to the flow). In the remaining seven simulations of nonbanded events, the WRF produced *banded* precipitation features in the 20070105, 20080316, and 20100430 events (Figs. 2.6c,d and 2.7b); weak, disorganized convection in the 20061202, 20110403 and 20111203 events (Figs. 2.6b and 2.7c,d); and no precipitation features near the lake in the 20100319 event (Fig. 2.7a). These results are broadly consistent with operational forecast experience, which indicates that the WRF nearly always generates banded precipitation features (T. Alcott, National Weather Service, personal communication, 2014), whereas nonbanded features are most commonly observed (Alcott et al. 2012).

Subjective comparison of WRF simulated event total precipitation and REP reveals a fair representation of precipitation by WRF in banded GSLE events. The seven simulations of banded events that produced banded precipitation features (20071018,[2] 20080115, 20080411, 20081105, 20101027, 20101231, and 20110427) produced physically realistic total precipitation distributions in terms of the aspect ratio (i.e., length

---

[2] Precipitation < 1 mm has been removed from the 20071018 REP (Fig. 2.8) to remove spurious precipitation caused by widespread nonprecipitation 5 dBZ echoes within the KMTX beam coverage.

to width) and the orientation of the axis of the maximum precipitation (Figs. 2.8a,c, 2.9a,b,d, and 2.10b,c). The two simulations that produced weak and disorganized precipitation features (20071227 and 20100407) produced maximum event total precipitation amounts that were similar to the REP, but these maxima occurred further south of the REP maxima [rightward and downwind relative to the flow (Figs. 2.8b and 2.9c)]. The forecasts of the remaining events (20080226 and 20101129) produced no precipitation near the lake, in contrast with the REP, which reveals precipitation over the Oquirrh Mountains (Figs. 2.8d and 2.10a).

In the seven simulations of banded events that produced banded precipitation features (20071018, 20080115, 20080411, 20081105, 20101027, 20101231, and 20110427), subjective comparison suggests a southward bias (rightward and downwind relative to the flow) in the WRF forecast compared to the REP (Figs. 2.8a,c, 2.9a,b,d, and 2.10b,c). A similar rightward bias has been noted previously in simulations of GSLE (Steenburgh and Onton 2001; Onton and Steenburgh 2001; Alcott and Steenburgh 2013) and simulations of lake effect over the Great Lakes (Ballentine and Zaff 2007; Arnott 2010; Shi et al. 2010; Theeuwes et al. 2010; Reeves and Dawson 2012) using a variety of model configurations and parameterizations. Further, the WRF generally produced more precipitation over terrain than found in the REP. For example, precipitation amounts over the Oquirrh Mountains in the 20080411, 20100407, and 20110427 simulations were higher than found in the REP, and the 20081105 simulation produced excessive precipitation over both the Central Wasatch Mountains and the Salt Lake Valley (cf. Figs. 2.8c, 2.9a,c, and 2.10c). The large WRF precipitation amounts over terrain are not necessarily an overforecast, however, because the REP tends to underestimate precipitation over the mountains due to terrain blockage and overshooting (e.g., Westrick et al. 1999; Alcott and Steenburgh 2013).

WRF event total precipitation during the nonbanded GSLE events did not compare well against the REP. The simulation that produced nonbanded precipitation features (20061129) compared best with the REP with errors in precipitation amount and location (Fig. 2.11a). The three simulations of nonbanded GSLE that produced weak and disorganized precipitation features (20061202, 20110403, and 20111203) produced smaller precipitation coverage than the REP (Figs. 2.11b and 2.12c,d). The 20100319 simulation produced no precipitation near the lake (Fig. 2.12a). The remaining three simulations that produced *banded* precipitation features (20070105, 20080316, and 20100430) were generally poor, producing much more precipitation than the REP (Figs. 2.11c,d and 2.12b).

Simulations of nonbanded GSLE events appeared to produce similar biases in precipitation location and amount as seen in simulations of banded GSLE events. A southward (rightward and downwind relative to the flow) bias in precipitation location was seen in seven of eight simulations [20061129, 20061202, 20070105, 20080316, 20100430, 20110403, and 20111203 (Figs. 2.11a,b,c,d and 2.12b,c,d)]. The WRF also produced more precipitation than the REP over higher terrain in all three of the simulations that produced banded precipitation features (20070105, 20080316, and 20100430) and the one simulation that produced nonbanded precipitation features [20061129 (Figs. 2.11a,c,d and 2.12b)], although this at least partly reflects the REP underestimate.

To summarize, physically realistic banded precipitation features were generated in simulations of seven of the 11 banded GSLE events, whereas nonbanded precipitation features were generated in only one of the eight simulations of nonbanded GSLE events. Banded features were also produced in three simulations of nonbanded GSLE events. Despite some success in banded GSLE events, simulations of both banded and nonbanded events revealed a tendency to generate precipitation southward (rightward and downstream relative to the flow) of observed and a propensity to produce higher precipitation amounts over higher terrain than seen in the REP, although this at least partially reflects a REP bias. We now employ traditional verification measures to further evaluate the fidelity of the simulations.

2.4.2 Traditional Grid Verification

Traditional objective statistics reveal low skill in the majority of the WRF simulations, but higher skill was recorded in simulations of banded events. The seven simulations of banded GSLE events that produced banded precipitation features (20071018, 20080115, 20080411, 20081105, 20101027, 20101231, and 20110427) recorded ETS ranging from 0.04–0.4 and biases of 0.45–6.37 at the $\geq$ 1 mm precipitation threshold (Table 2.2). The 0.04 ETS from the 20080115 simulation reflects a significant overforecast as shown by the high bias (6.37). In general, ETS is lower and bias higher for larger thresholds (cf. Fig. 2.13; Table 2.2). The rapid decline in ETS with increasing precipitation threshold indicates that these simulations are most skillful in a yes/no sense and struggle with accurate prediction of amount and/or location of larger precipitation amounts. Not surprisingly, simulations of the remaining four banded events (20071227, 20080226, 20100407, and 20101129), which failed to produce realistic precipitation features, show less skill with ETS ≤ 0.11 at all thresholds.

ETS for simulations of nonbanded GSLE events are generally much lower than simulations of the banded events (cf. Tables 2.2 and 2.3). The simulation that produced nonbanded precipitation features (20061129) achieved an ETS of 0.2 and bias of 1.15 at the 1-mm threshold, with lower ETS and higher bias at higher thresholds (Table 2.3; Fig. 2.14). The four simulations that failed to produce realistic precipitation features (20061202, 20110403, 20100319, and 20111203) recorded ETS ≤ 0.05 at all thresholds. One of the simulations that produced *banded* precipitation features (20100430) recorded an ETS (0.17) at the 1-mm threshold, but bias rapidly increased and ETS decreased with precipitation threshold. The remaining two simulations of nonbanded events that produced *banded* precipitation signatures (20070105 and 20080316) recorded ETS of 0.04 and 0.05, respectively, both with a bias > 1.

Neighborhood ETS at the ≥ 1 mm precipitation threshold from simulations of banded GSLE events showed mixed trends (uncorrelated with the type of precipitation feature produced by the model) as neighborhood size increases (Table 2.4). The 20071018, 20071227, 20080115, 20100407, and 20110427 simulations show minor skill improvement with increasing neighborhood size, implying that displacement of precipitation between the simulations and REP contributed to the low skill. The skill of the two simulations that produced no precipitation features near the lake (20080226 and 20101129) remains low at every neighborhood size. The remaining four simulations (20080411, 20081105, 20101027, and 20101231) reveal a small decrease in skill as neighborhood size increases.

Simulations of nonbanded GSLE events verified with the neighborhood method at the ≥ 1-mm precipitation threshold showed minor improvement as neighborhood size increased (Table 2.5). Despite the minor improvement with increasing neighborhood size, four simulations did not record ETS > 0.1 even at the largest neighborhood size, (20061202, 20070105, 20100319, and 20111203). The 20061129 and 20110403 simulations produced slightly higher ETS with increasing neighborhood size, and this improvement implies that displacement of precipitation between the simulation and REP caused the simulation's low skill. The remaining two simulations (20080316 and 20100430) scored ETS of 0.17 and 0.22, respectively, at the largest neighborhood despite significantly overforecasting precipitation (cf. Table 2.3; Figs. 2.11d and 2.12b).

Although skill is low overall, simulations of banded events record higher ETS than simulations of nonbanded events. For the ≥ 1-mm threshold, the aggregated ETS and bias for the banded GSLE events are 0.24 and 0.90, respectively, compared to only 0.15 and 1.28 recorded for the nonbanded GSLE events. The aggregate ETS from simulations of banded GSLE events is similar to ETS recorded by simulations of warm-season convection (Gallus 2002; Aligo et al. 2009; Clark et al. 2010; Stratman et al. 2013). Biases in the WRF do contribute to the generally low skill. For example, high bias and low ETS at thresholds greater than the ≥ 3-mm threshold imply an overforecast of precipitation coverage. In addition, the minor increase in skill with increasing neighborhood size in many of the simulations implies precipitation location bias reduces the skill of these WRF simulations.

2.4.3 Object-Based Verification

Precipitation object images from the seven simulations of banded GSLE events that produced banded precipitation features (20071018, 20080115, 20080411, 20081105, 20101027, 20101231, and 20110427) show WRF event total precipitation objects that are visually similar in orientation and aspect ratio to REP objects, but are displaced generally southward (rightward and downstream relative to the flow) of the REP objects (Figs. 2.15a,c, 2.16a,b,d, and 2.17b,c). The two simulations that produced weak disorganized precipitation features in simulated reflectivity produce precipitation objects far from the lake. The 20071227 simulation produced weak disorganized precipitation features and the simulated precipitation object is shifted downstream from the REP object (Fig. 2.15b). The 20100407 simulation also produced weak disorganized precipitation features and the event total precipitation object is much smaller than the REP object (Fig. 2.16c). The remaining two simulations (20080226 and 20101129) produce no event total precipitation in the vicinity of the lake to compare against the REP objects (Figs. 2.15d, and 2.17a).

MODE allows us to compare the attributes of the simulated precipitation and REP object pairs to quantify how well the simulations match the REP. The total interest, I, from the seven simulations of banded GSLE events that produced banded precipitation features is on average 0.90, indicating a good match (Table 2.6). During these events, the mean aspect ratio and orientation angle of the simulated precipitation objects (1.88 and -42.71) are similar to the mean for the REP objects (2.07 and -41.27). However, the average object centroid distance error in these events is 25.0 km (about 70% of the length of the Salt Lake Valley) on a bearing of 171.1°, consistent with the subjective identification of a southward (rightward and downstream relative to the flow) displacement of WRF precipitation. This location bias reduces the skill of the simulations of the banded GSLE events.

MODE also illustrates some of the shortcomings of the simulations of nonbanded events. The simulation that produced nonbanded precipitation features (20061129) produced a simulated precipitation object that was similar to the REP object in terms of aspect ratio and to a lesser degree orientation angle, but exhibited significant southward displacement (rightward and downstream relative to the flow, Fig. 2.18a). In the three simulations of nonbanded events that produced *banded* precipitation features (20070105, 20080316, and 20100430) the simulated precipitation objects were significantly displaced southward (rightward and downstream relative to the flow) of the REP objects (Figs. 2.18c,d and 2.19b). Weak, disorganized convection was simulated in the 20061202, 20110403, and 20111203 events and the precipitation objects not only revealed large displacement from the REP objects, but precipitation coverage was very underforecast (Figs. 2.18b; 2.19c,d). The remaining simulation produced no precipitation near the lake (20100319), and no comparison with REP object was possible (Fig. 2.19a).

The only simulation to successfully recreate nonbanded precipitation features (20061129) scored $I = 0.85$, but the simulated precipitation centroid was 37.91 km from the REP object centroid on a bearing of 226.43°. The mean I of the seven simulations of nonbanded GSLE events that produced any precipitation features was 0.42, much less than found in the banded event simulations (Table 2.7). This value is greatly reduced by $I = 0$ in the 20061202 event. Removing this simulation increases the mean I to 0.84, closer but still smaller than found in the simulations of banded GSLE events that produced banded precipitation features. The mean simulated precipitation object aspect ratio (1.98) and mean REP object aspect ratio (2.09) are similar, but the mean simulated precipitation object orientation angle (13.55) is quite different from the mean REP object orientation angle (-18.68). This indicates poor simulation of the precipitation object orientation by the WRF. Displacement of simulated precipitation objects in nonbanded GSLE events is on average 30.59 km at a bearing of 203.18° from REP objects, which is rightward and downstream relative to the flow.

2.5 Conclusions

Overall, the convection-permitting WRF simulations of GSLE events examined here are most skillful in a yes/no sense, but struggle with the prediction of amount and/or location and the generation of nonbanded events. The ETS produced by WRF was 0.4 at the $\geq$ 1 mm threshold from a simulation of the 20101027 banded GSLE event. In aggregate, simulations of banded GSLE events produced an ETS of 0.24 at the $\geq$ 1 mm threshold, similar to other convection simulations (Gallus 2002; Aligo et al. 2009; Clark et al. 2010; Stratman et al. 2013). Lower ETS were produced by simulations of nonbanded events with an aggregate ETS of only 0.15 at the $\geq$ 1 mm threshold. Furthermore, three out of eight simulations of nonbanded GSLE events produced *banded* precipitation features, a result that is broadly consistent with operational forecast experience that indicates a propensity of WRF to generate banded precipitation features (T. Alcott, National Weather Service, personal communication, 2014). Skill in simulations of both banded and nonbanded GSLE events dropped fairly rapidly at higher precipitation thresholds casting doubt on the reliability of predicting GSLE precipitation amounts with WRF.

Biases in precipitation location, coverage, and amount contribute to the low skill of WRF simulations of both banded and nonbanded GSLE events. Subjectively, the precipitation in WRF simulations of both banded and nonbanded GSLE events appeared to be displaced southward (rightward and downstream relative to the flow) from the REP. MODE quantifies this bias and showed that the WRF displaced precipitation object centroids generally south of REP centroids by ~25 km. This displacement is large enough that neighborhood ETS calculations did not improve even for our largest neighborhood stencil [18.5 km, which is almost the width of the southwest arm of the lake (20–25km)]. Although this result could be sensitive to the model, parameterization suite, or local environment, similar band position errors have been noted in other lake effect papers, including some that have used different parameterization suites to examine events in both Utah and the Great Lakes region (Steenburgh and Onton 2001; Onton and Steenburgh 2001; Ballentine and Zaff 2007; Arnott 2010; Shi et al. 2010; Theeuwes et al. 2010; Reeves and Dawson 2012; Alcott and Steenburgh 2013). Identification of the causes of this bias, although left for future work, would likely improve lake-effect prediction in general.

WRF simulations of banded and nonbanded events also overforecast precipitation coverage, especially at and above the ≥ 3-mm threshold, as shown by the bias values from the WRF and REP comparisons. However, this at least partly reflects an underestimate of precipitation over higher elevations by the REP due to terrain blockage and overshooting (e.g., Westrick et al. 1999; Alcott and Steenburgh 2013).

These results suggest that reliable prediction of GSLE is very challenging with current convection-permitting modeling systems. In operations, skill would likely be lower than indicated by our results because we limited large-scale error growth by using 6-hourly NAM analyses as lateral boundary conditions. Pessimism about the skill of the operational forecast is also warranted because we did not include any model "false alarms" (i.e., situations in which the WRF generates GSLE precipitation, but none is observed), which would lower overall skill and reliability.

MODE provided useful attribute information about GSLE-related precipitation objects in the REP for every event, revealing its potential as a tool for objectively classifying radar characteristics of observed events. For example, MODE could be applied to NEXRAD reflectivity imagery to identify and classify GSLE morphological structures as was done subjectively by Alcott et al. (2012). Such an approach, combined with other atmospheric analyses, might help to better identify the environmental conditions that lead to banded and nonbanded events.

Finally, the WRF precipitation location bias (i.e., right and downstream relative to the flow) and tendency to generate banded GSLE features warrant further investigation to improve both deterministic and ensemble modeling system reliability. The former appears to be an issue in other regions, including the Great Lakes (Ballentine and Zaff 2007; Arnott 2010; Shi et al. 2010; Theeuwes et al. 2010; Reeves and Dawson 2012) and has been shown by Arnott (2010) to negatively affect the ensemble mean in WRF-ARW simulations of lake effect over Lake Ontario.

Table 2.1. Banded and nonbanded GSLE event dates (yyymmdd), start times (UTC), end times (UTC), WRF model run start date and time (yyyymmdd xxxx UTC hour), and WRF integration time (h).

Event	**Start**	**End**	**WRF Start**	**WRF Integration Time (h)**
Banded				
20071018	0430	1130	20071017 1800	24
20071227	20071227 0700	20071228 0000	20071227 0000	30
20080115	20080115 2100	20080116 2000	20080115 1200	36
20080226	0500	0830	20080225 1800	24
20080411	0430	1800	20080410 1800	30
20081105	0600	2230	20081105 0000	24
20100407	0300	0700	20100406 1800	24
20101027	0230	1700	20101026 1800	24
20101129	1130	1530	20101129 0000	24
20101231	20101231 1230	20110101 0400	20101231 0600	24
20110427	0300	1000	20110426 1800	24
Nonbanded				
20061129	0630	1900	20061129 0000	24
20061202	1100	2000	20061202 0000	24
20070105	1130	2030	20070105 0000	24
20080316	0900	1800	20080315 1800	30
20100319	1230	1800	20100319 0000	24
20100430	0200	1900	20100429 1800	30
20110403	1330	1800	20110403 0600	24
20111203	0730	1530	20111203 0000	24

Table 2.2. ETS and bias (parentheses) for simulations of banded GSLE events compared with REP ≥ 1-, 3-, 5-, 10-, and 15-mm thresholds. Symbols indicate WRF-simulated precipitation feature type: * = banded, # = weak, disorganized, $ = no precipitation feature near the lake.

Event	Precipitation Threshold (mm)				
	1	3	5	10	15
20071018 *	0.19 (0.97)	0.12 (1.11)	0.06 (1.14)	-0.001 (0.70)	0.0 (N/A)
20071227 #	0.11 (1.36)	-0.0007 (5.72)	0.0 (0.0)	N/A	N/A
20080115 *	0.04 (6.87)	-0.001 (14.04)	-0.0004 (7.39)	N/A	N/A
20080226 $	-0.006 (0.87)	-0.00006 (0.06)	N/A	N/A	N/A
20080411 *	0.12 (0.97)	0.08 (1.70)	0.003 (3.2)	0.0 (N/A)	0.0 (N/A)
20081105 *	0.23 (0.60)	0.36 (1.29)	0.29 (1.91)	0.17 (3.47)	0.04 (16.83)
20100407 #	0.04 (0.81)	0.0 (N/A)	N/A	N/A	N/A
20101027 *	0.4 (0.87)	0.33 (1.27)	0.31 (1.49)	0.09 (3.31)	-0.001 (7.58)
20101129 $	-0.0009 (0.06)	0.0 (0.0)	0.0 (0.0)	N/A	N/A
20101231 *	0.38 (1.14)	0.21 (1.10)	-0.0008 (1.76)	N/A	N/A
20110427 *	0.19 (0.45)	0.02 (15.88)	0.0 (N/A)	0.0 (N/A)	N/A

Table 2.3. ETS and bias (parentheses) for simulations of nonbanded GSLE events compared with REP ≥ 1-, 3-, 5-, 10-, and 15-mm thresholds. Symbols indicate WRF-simulated precipitation feature type: * = banded, # = weak, disorganized, $ = no precipitation feature near the lake, ! = nonbanded.

Event	Precipitation Threshold (mm)				
	1	3	5	10	15
20061129 !	0.2 (1.15)	0.19 (1.01)	0.04 (3.81)	-0.0002 (31.18)	0.0 (N/A)
20061202 #	-0.001 (0.04)	0.0 (0.0)	0.0 (0.0)	0.0 (0.0)	0.0 (0.0)
20070105 *	0.04 (1.77)	-0.003 (4.36)	-0.0003 (10.06)	N/A	N/A
20080316 *	0.05 (6.29)	0.03 (27.93)	0.01 (71.01)	0.0 (N/A)	0.0 (N/A)
20100319 $	-0.005 (0.92)	-0.002 (11.98)	-0.0002 (75.73)	0.0 (N/A)	N/A
20100430 *	0.17 (1.03)	0.17 (1.96)	0.11 (2.39)	0.04 (5.72)	-0.0001 (417.13)
20110403 #	0.05 (0.23)	-0.0003 (0.06)	0.0 (0.0)	N/A	N/A
20111203 #	0.003 (1.05)	-0.0006 (2.52)	0.0 (0.0)	N/A	N/A

Table 2.4. Neighborhood ETS (≥1 mm threshold with subscript indicating width of neighborhood in grid points) for simulations of banded GSLE events compared with REP. Symbols indicate WRF-simulated precipitation feature type: * = banded, # = weak, disorganized, $ = no precipitation feature near the lake.

Event	ETS_0	ETS_9	ETS_{17}	ETS_{33}
20071018 *	0.19	0.25	0.29	0.35
20071227 #	0.11	0.14	0.15	0.16
20080115 *	0.04	0.06	0.07	0.13
20080226 $	-0.006	-0.001	0.007	0.03
20080411 *	0.12	0.14	0.12	0.12
20081105 *	0.23	0.20	0.20	0.20
20100407 #	0.03	0.10	0.13	0.17
20101027 *	0.40	0.35	0.32	0.28
20101129 $	-0.0009	-0.002	-0.003	-0.004
20101231 *	0.38	0.38	0.33	0.27
20110427 *	0.19	0.24	0.25	0.26

Table 2.5. Neighborhood ETS (≥1 mm threshold with subscript indicating width of neighborhood in grid points) for simulations of nonbanded GSLE events compared with REP. Symbols indicate WRF-simulated precipitation feature type: * = banded, # = weak, disorganized, $ = no precipitation feature near the lake, and ! = nonbanded.

Event	ETS_0	ETS_9	ETS_{17}	ETS_{33}
20061129 !	0.20	0.25	0.26	0.27
20061202 #	-0.001	-0.003	-0.006	0.003
20070105 *	0.04	0.06	0.06	0.06
20080316 *	0.05	0.08	0.11	0.17
20100319 $	-0.005	0.04	0.07	0.09
20100430 *	0.17	0.12	0.21	0.22
20110403 #	0.05	0.1	0.15	0.2
20111203 #	0.003	0.02	0.03	0.03

Table 2.6. MODE data for simulations of banded GSLE events compared with REP ≥ 1 mm precipitation threshold except for 20081105, which uses ≥ 5 mm threshold. Averages calculated from simulations that produced banded precipitation features. Symbols indicate WRF-simulated precipitation feature type: * = banded, # = weak, disorganized, $ = no precipitation feature near the lake.

Event	GSLE Pair *I*	REP Object Aspect Ratio	REP Object Orientation Angle (Deg)	Simulated Object Aspect Ratio	Simulated Object Orientation Angle (Deg)	Centroid Distance (km)	Bearing From REP Object (Deg)
20071018 *	0.94	1.54	-30.95	2.14	-27.58	28.16	163.63
20071227 #	0.92	1.27	-51.08	1.36	-60.77	30.70	185.65
20080115 *	0.78	1.45	-70.30	1.43	-38.34	32.27	151.56
20080226 $	N/A	4.07	-52.73	N/A	N/A	N/A	N/A
20080411 *	0.92	2.30	-51.98	2.27	-52.00	26.33	244.41
20081105 *	0.83	2.26	-24.21	1.38	-30.53	31.47	139.76
20100407 #	0.64	2.69	-60.16	1.89	84.07	19.92	269.52
20101027 *	0.96	2.67	-32.46	1.87	-35.55	19.56	152.49
20101129 $	N/A	1.12	71.01	N/A	N/A	N/A	N/A
20101231 *	0.99	2.33	-43.51	2.13	-47.55	21.16	138.34
20110427 *	0.87	1.91	-35.45	1.97	-67.44	16.21	207.61
Average *	0.90	2.07	-41.27	1.88	-42.71	25.02	171.11

Table 2.7. MODE data for simulations of nonbanded GSLE events compared with REP ≥ 1 mm precipitation threshold except for 20100430, which uses ≥ 5 mm threshold. Averages calculated from all simulations that produced precipitation. Symbols indicate WRF-simulated precipitation feature type: * = banded, # = weak, disorganized, $ = no precipitation feature near the lake, and ! = nonbanded.

Event	GSLE Pair *I*	REP Object Aspect Ratio	REP Object Orientation Angle (Deg)	Simulated Object Aspect Ratio	Simulated Object Orientation Angle (Deg)	Centroid Distance (km)	Bearing From REP Object (Deg)
20061129 !	0.85	1.31	-10.19	1.09	-51.20	37.91	226.43
20061202 #	0.0	1.23	-55.26	1.26	66.86	41.40	281.94
20070105 *	0.80	1.49	-70.66	1.10	-13.22	38.90	201.89
20080316 *	0.87	1.75	15.29	1.96	-8.62	21.79	140.93
20100319 $	N/A	2.38	1.88	N/A	N/A	N/A	N/A
20100430 *	0.85	1.48	-17.27	1.40	-8.07	35.00	156.50
20110403 #	0.75	1.64	-23.29	1.12	30.27	28.08	205.60
20111203 #	0.91 (0.46)	1.26 (1.81)	47.35 (25.26)	2.49	78.89	11.07 (32.45)	209.00 (161.30)
Average	0.42	2.09	-18.69	1.98	13.55	30.59	203.18

		REP	
		YES	NO
WRF	YES	HIT	FALSE ALARM
	NO	MISS	CORRECT NEGATIVE

Fig. 2.1. 2x2 contingency table where HITS, MISSES, FALSE ALARMS, and CORRECT NEGATIVES represent the number of occurrences of each category contingent on WRF and REP precipitation matching or exceeding a given precipitation threshold.

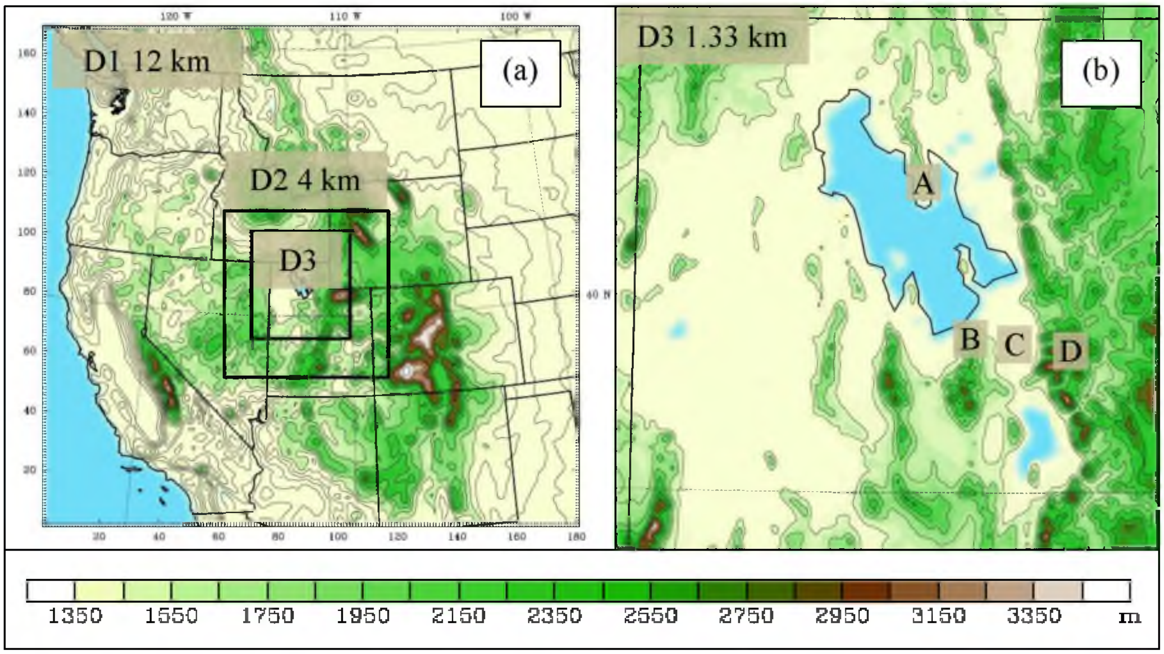

Fig. 2.2. Maps of the Western United States and Northern Utah showing (a) WRF model domains (labeled with grid spacing) and terrain (shaded and contoured) and (b) the inner domain (labeled with grid spacing) with major features including: KMTX (A), Oquirrh Mountains (B), Salt Lake Valley (C), and central Wasatch Mountains (D). Elevation (m) contoured and shaded following scale below.

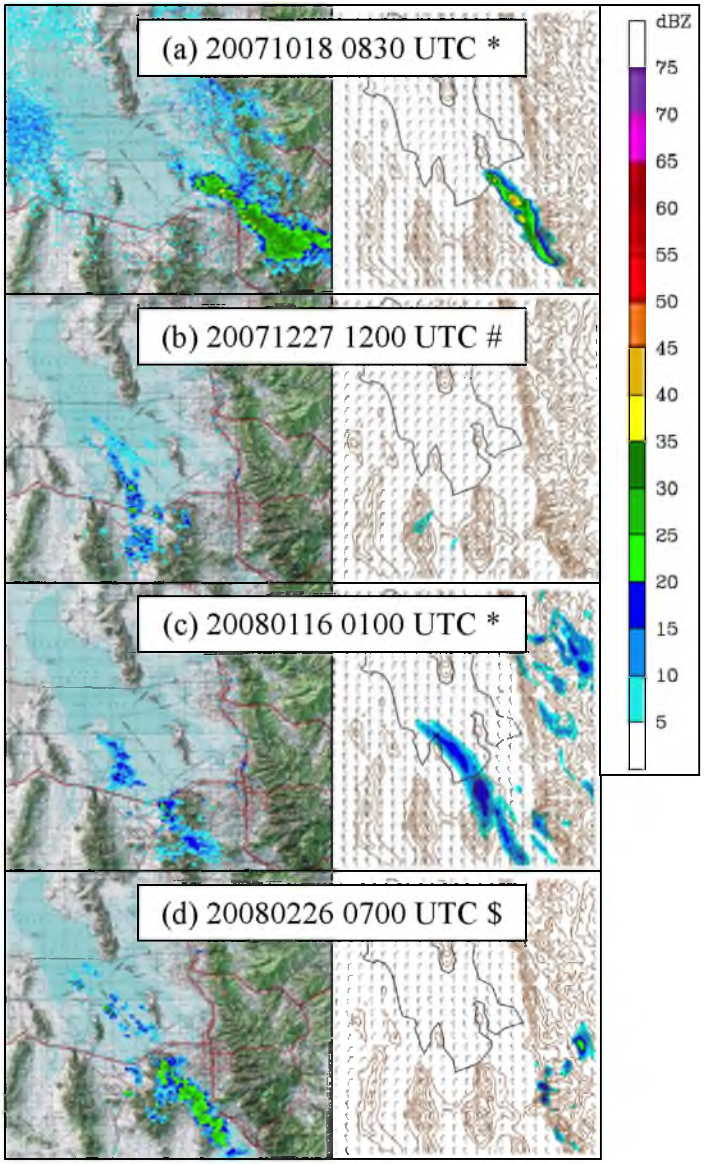

Fig. 2.3. NEXRAD lowest elevation angle reflectivity (left column, dBZ, shaded following scale at right); simulated 2.5 km MSL reflectivity (middle column, dBZ, shaded following scale at right) and winds (full and half barb denote 5 and 2.5 m s^{-1}, respectively) at times noted in the inset for the (a) 20071018, (b) 20071227, (c) 20080115, and (d) 20080226 banded GSLE events. Symbols indicate WRF-simulated precipitation feature type: * = banded, # = weak, disorganized, $ = no precipitation feature near the lake.

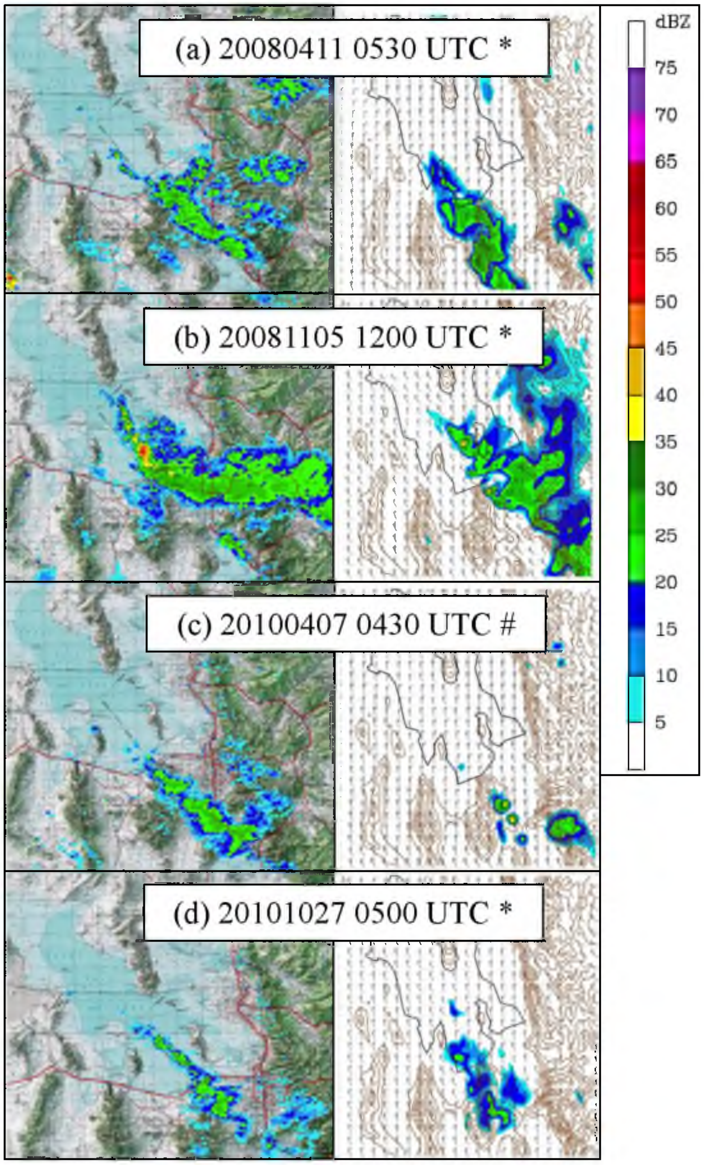

Fig. 2.4. Same as Fig. 2.3 for the (a) 20080411, (b) 20081105, (c) 20100407, and (d) 20101027 banded GSLE events.

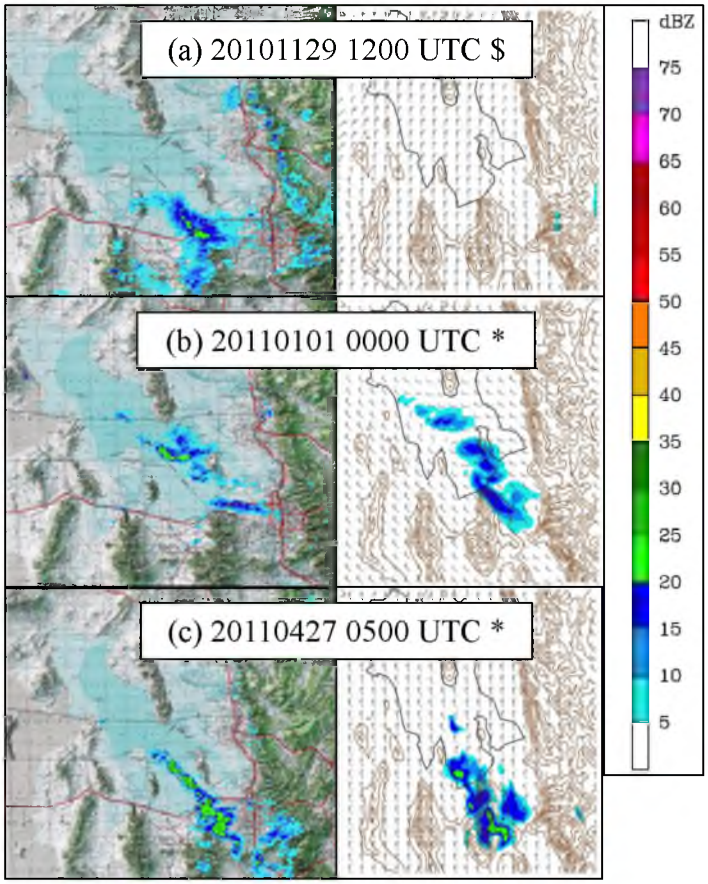

Fig. 2.5. Same as Fig. 2.3 for the (a) 20101129, (b) 20101231, (c) 20110427 banded GSLE events.

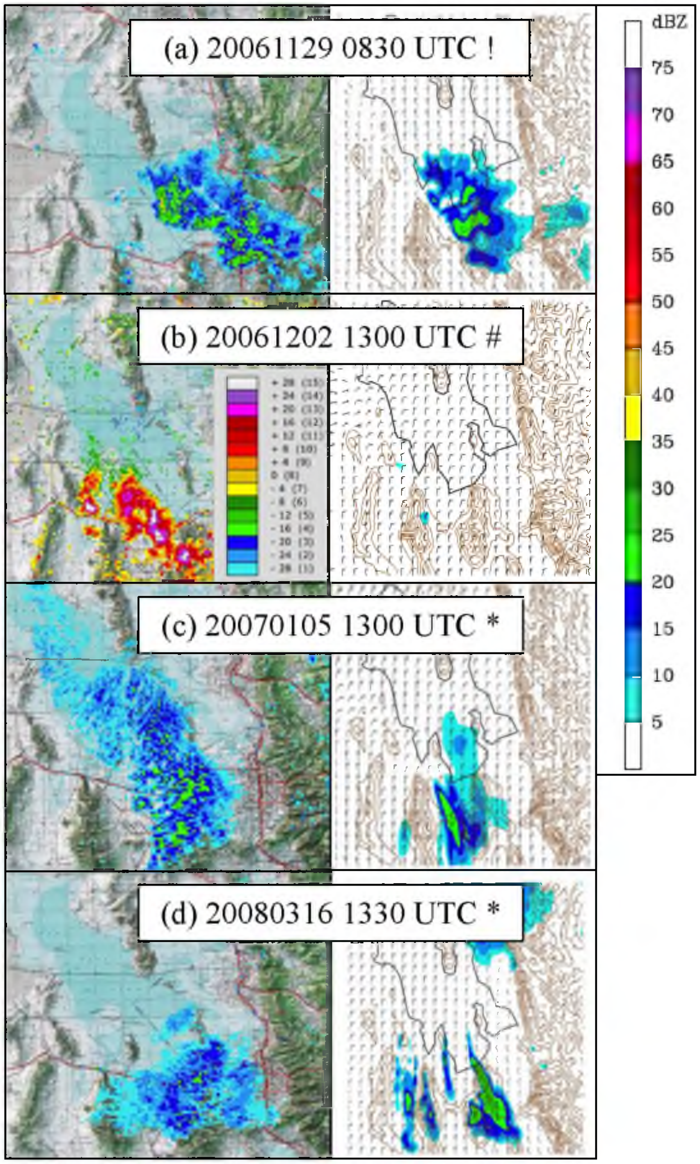

Fig. 2.6. NEXRAD lowest elevation angle reflectivity (left column, dBZ, shaded following scale at right); simulated 2.5 km MSL reflectivity (middle column, dBZ, shaded following scale at right) and winds (full and half barb denote 5 and 2.5 m s^{-1}, respectively) at times noted in the inset for the (a) 20061129, (b) 20061202, (c) 20070105, and (d) 20080316 nonbanded GSLE events. Note inset legend for 20061202 event. Symbols indicate WRF-simulated precipitation feature type: * = banded, # = weak, disorganized, $ = no precipitation feature near the lake, and ! = nonbanded.

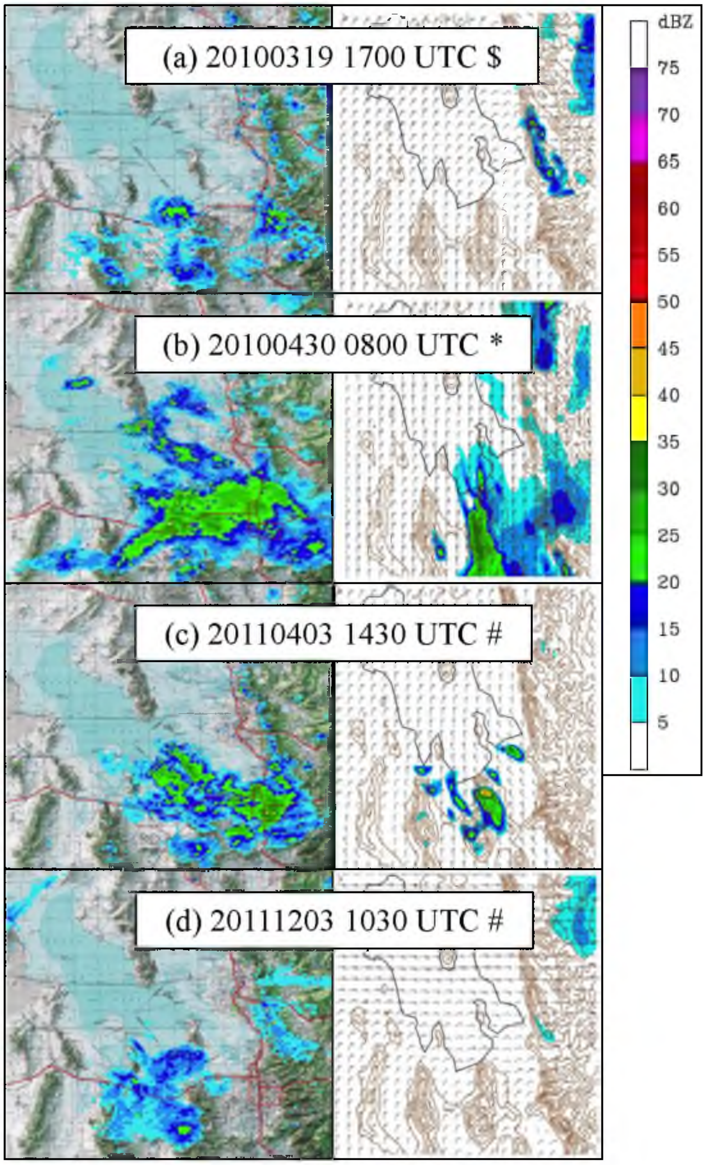

Fig. 2.7. Same as Figure 2.6 for the (a) 20100319, (b) 20100430, (c) 20110403, and (d) 20111203 nonbanded GSLE events.

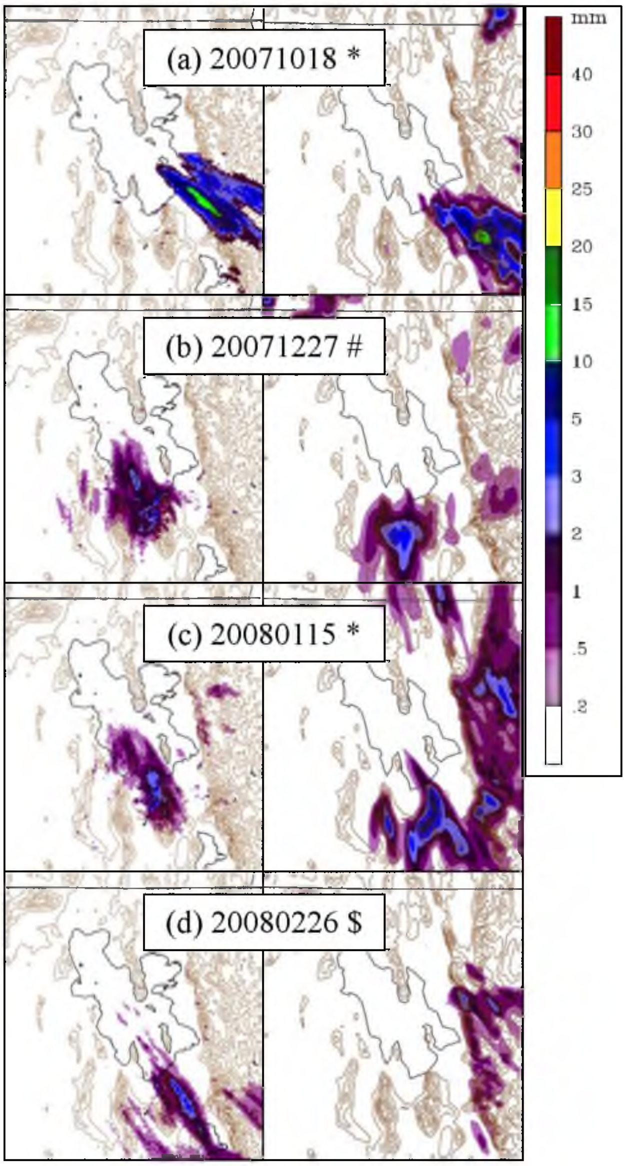

Fig. 2.8. REP (left column, shaded following scale at right) and WRF simulated precipitation (center column, shaded following scale at right) for the (a) 20071018, (b) 20071227, (c) 20080115, and (d) 20080226 banded GSLE events. Symbols indicate WRF-simulated precipitation feature type: * = banded, # = weak, disorganized, $ = no precipitation feature near the lake.

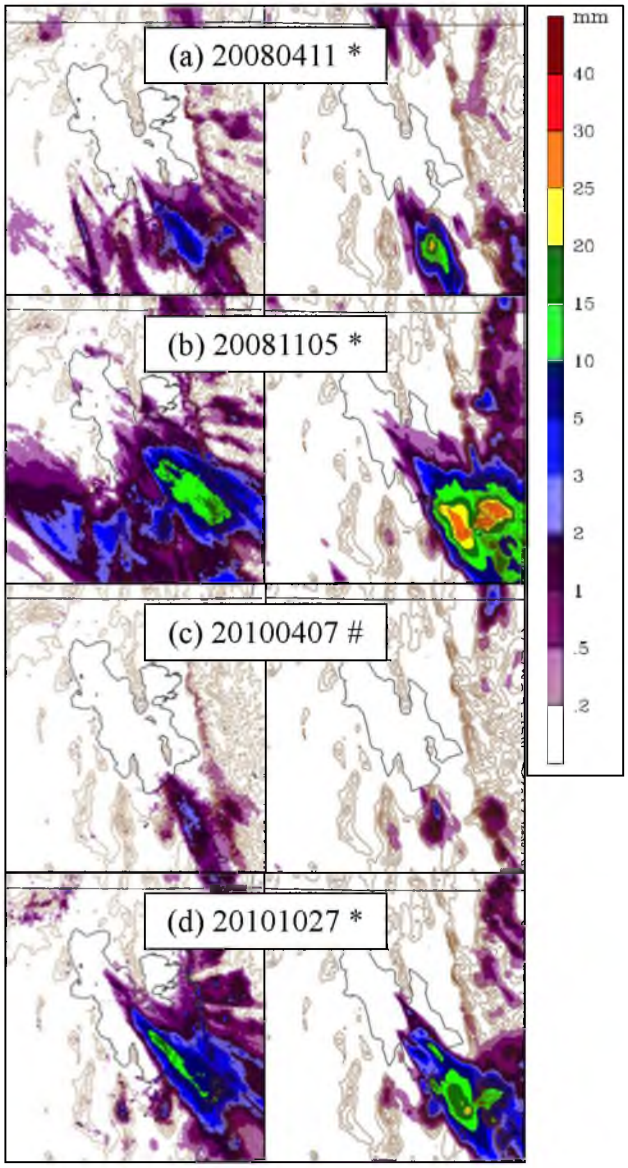

Fig. 2.9. Same as Fig. 2.8 for the (a) 20080411, (b) 20081105, (c) 20100407, and (d) 20101027 banded GSLE events.

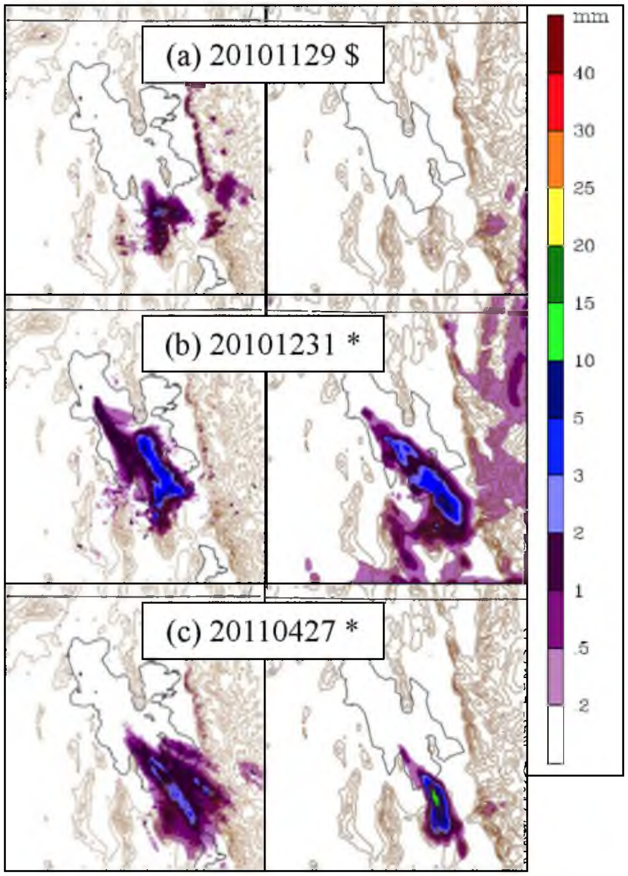

Fig. 2.10. Same as Fig. 2.8 for the (a) 20101129, (b) 20101231, and (c) 20100427 banded GSLE events.

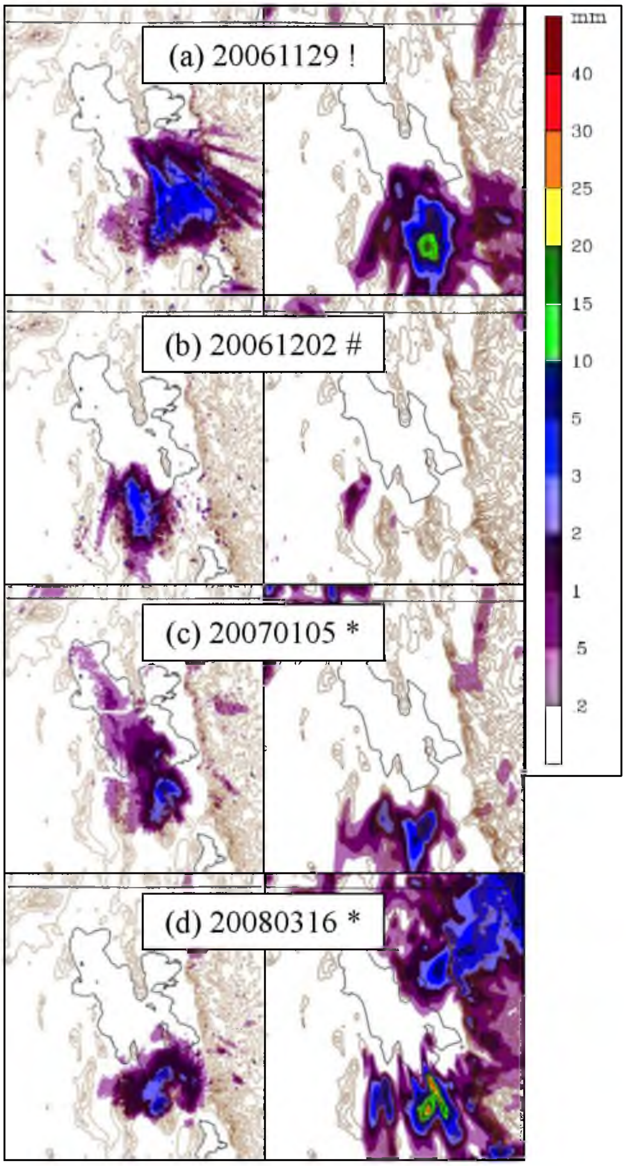

Fig. 2.11. REP (left column, shaded following scale at right) and WRF simulated precipitation (center column, shaded following scale at right) for the (a) 20061129, (b) 20061202, (c) 20070105, and (d) 20080316 nonbanded GSLE events. Symbols indicate WRF-simulated precipitation feature type: * = banded, # = weak, disorganized, $ = no precipitation feature near the lake, and ! = nonbanded.

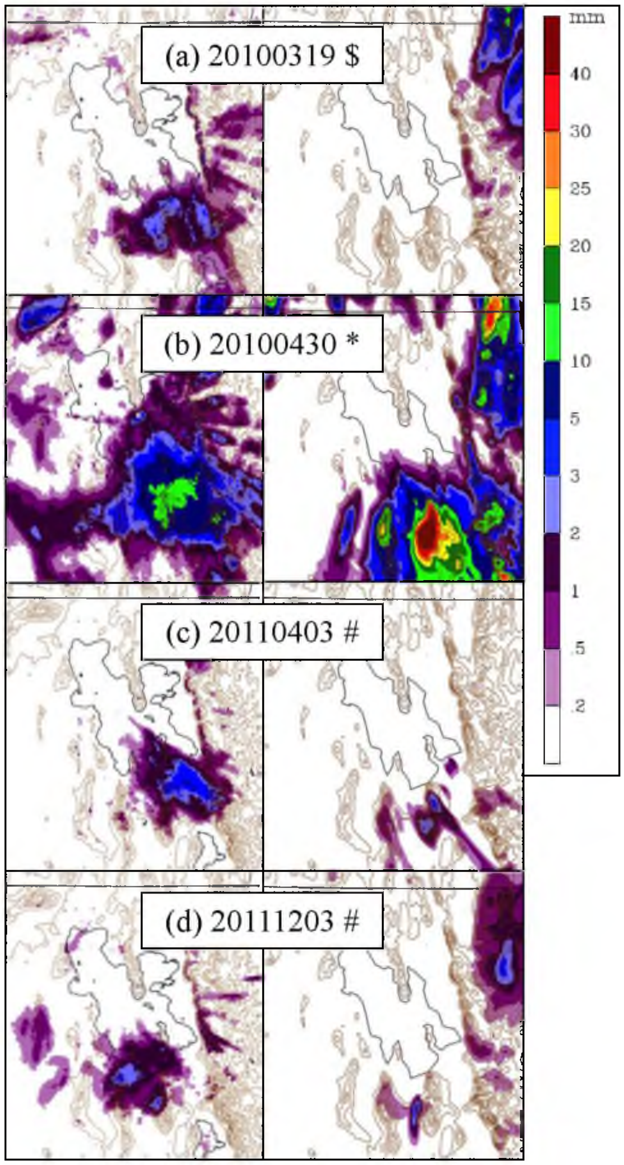

Fig. 2.12. Same as Fig. 2.11 for the 20100319, 20100430, 20110403, and 20111203 nonbanded GSLE events.

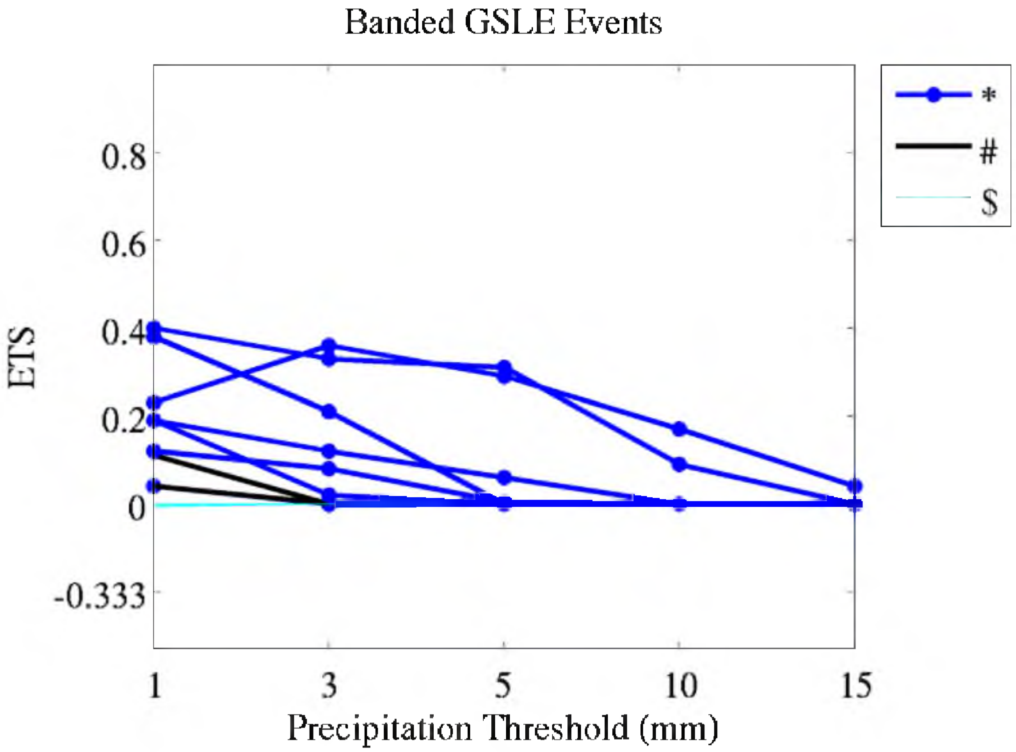

Fig. 2.13. ETS versus precipitation threshold for simulations of banded GSLE events. Symbols indicate WRF-simulated precipitation feature type: * = banded, # = weak, disorganized, $ = no precipitation feature near the lake.

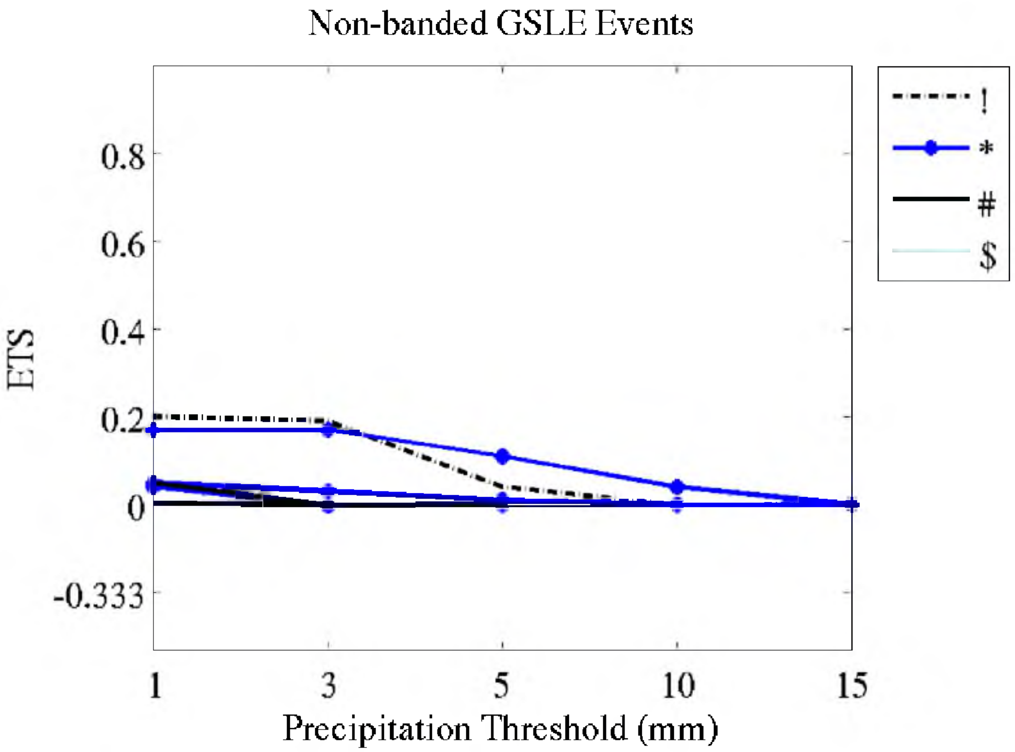

Fig. 2.14. ETS versus precipitation threshold for simulations of nonbanded GSLE events. Symbols indicate WRF-simulated precipitation feature type: * = banded, # = weak, disorganized, $ = no precipitation feature, and ! = nonbanded.

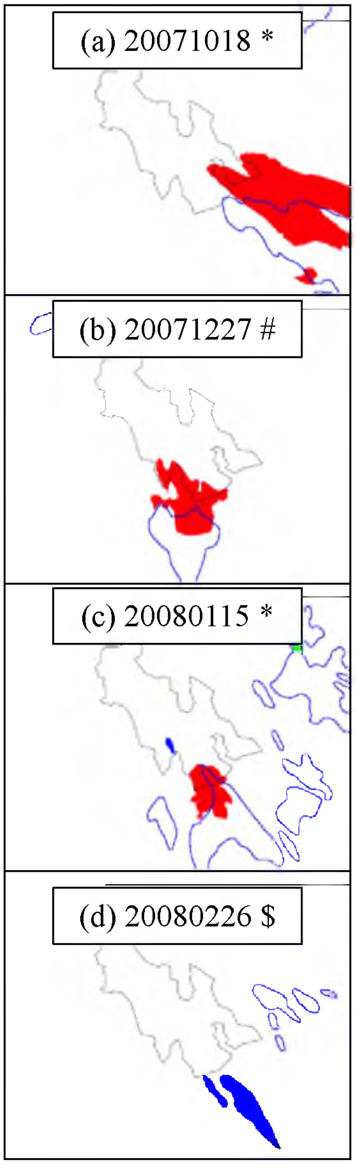

Fig. 2.15. MODE precipitation objects from REP (solid) and WRF simulation (contoured) for the (a) 20071018, (b) 20071227, (c) 20080115, and (d) 20080226 banded GSLE events. Objects identified at ≥ 1 mm threshold unless otherwise noted. Symbols indicate WRF-simulated precipitation feature type: * = banded, # = weak, disorganized, $ = no precipitation feature.

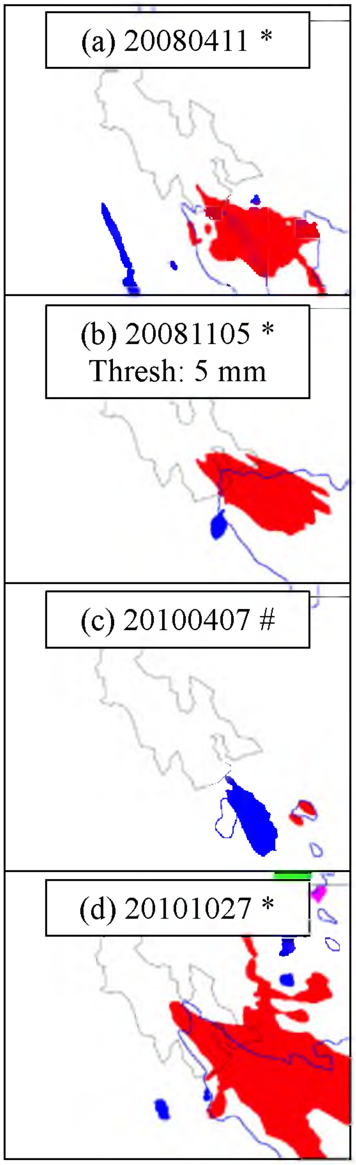

Fig. 2.16. Same as Fig. 2.15 for the (a) 20080411, (b) 20081105, (c) 20100407, and (d) 20101027 banded GSLE events.

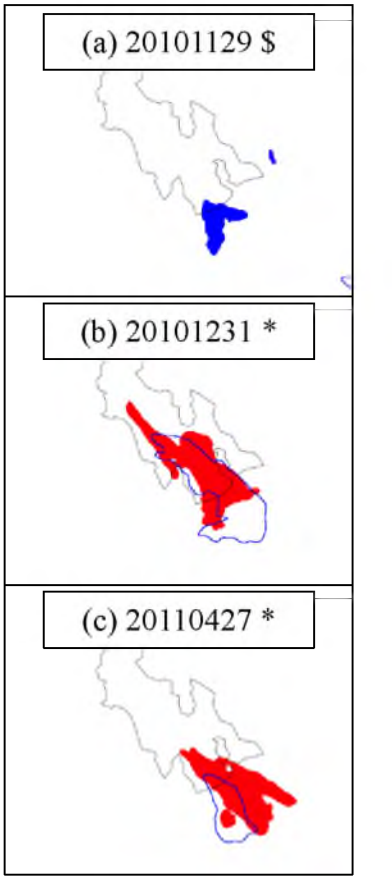

Fig. 2.17. Same as Fig. 2.15 for the (a) 20101129, (b) 20101231, and (c) 20100427 banded GSLE events.

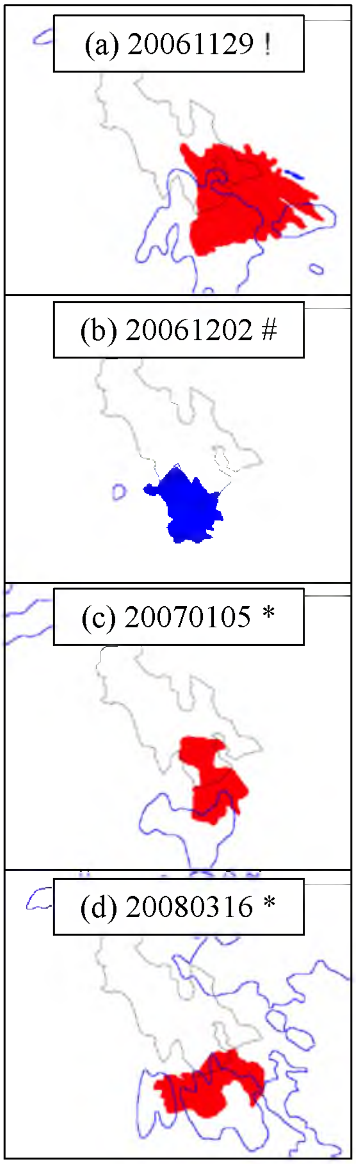

Fig. 2.18. MODE precipitation objects from REP (solid) and WRF simulation (contoured) for the (a) 20061129, (b) 20061202, (c) 20070105, and (d) 20080316 nonbanded GSLE events. Objects identified at ≥ 1 mm threshold unless otherwise noted. Symbols indicate WRF-simulated precipitation feature type: * = banded, # = weak, disorganized, $ = no precipitation feature, and ! = nonbanded.

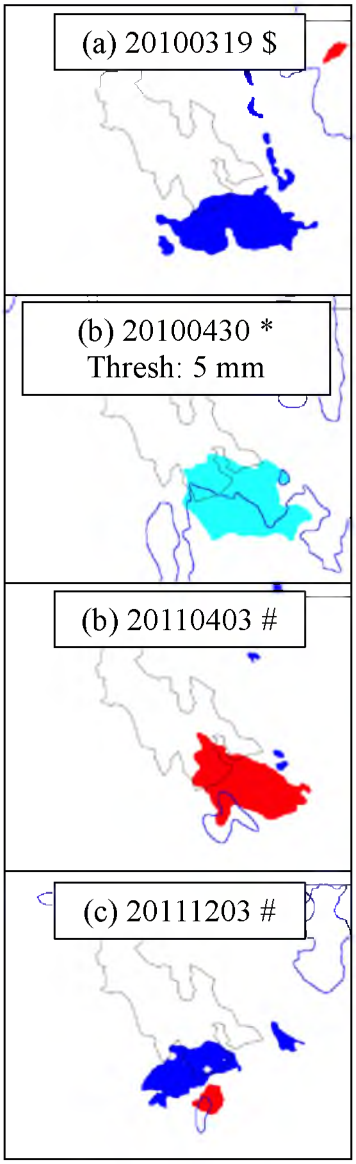

Fig. 2.19. Same as Fig. 2.18 for the (a) 20100319, (b) 20100430, (c) 20110403, and (d) 20111203 nonbanded GSLE events.

CHAPTER 3[3]

IMPACT OF MICROPHYSICS PARAMETERIZATION ON THE SIMULATION OF THE GREAT SALT LAKE EFFECT

3.1 Abstract

Simulations of convection at convection-permitting grid spacings are sensitive to the parameterization of microphysical processes, posing a challenge for operational weather prediction. Here we use the WRF model to examine the sensitivity of simulations of the Great Salt Lake Effect (GSLE) snowstorm of 27 October 2010 to the choice of microphysics parameterization (MP). We find that the simulated precipitation from four MP schemes varies in areal coverage, amount, and position. The Thompson scheme (THOM) verifies best against radar-derived precipitation estimates and gauge observations. The Goddard, Morrison, and WRF double-moment 6-class microphysics (WDM6) schemes produce more precipitation than THOM, with WDM6 producing the largest overprediction relative to radar-derived precipitation estimates and gauge observations. Analyses of hydrometeor mass tendencies show that WDM6 creates more graupel, less snow, and more total precipitation than the other schemes. These results indicate that the rate of graupel and snow production can strongly influence the

---

[3] Prof. Steenburgh and I submitted this chapter to *Weather and Forecasting* for publication. The manuscript is currently assigned to the editor for peer review.

precipitation efficiency in simulations of lake-effect storms, but further work is needed to evaluate MP scheme accuracy across a wider range of events, including the use of aircraft and ground-based hydrometeor sampling to validate MP hydrometeor categorization.

3.2 Introduction

The Great Salt Lake (GSL) basin of northern Utah is one of many areas around the world where lake-, sea-, or ocean-effect precipitation (hereafter simply lake effect) occurs when cold air flows over a relatively warm body of water and generates moist convection (Mitchell 1921; Peace and Sykes 1966; Estoque and Ninomya 1975; Andersson and Nilsson 1990; Carpenter 1993; Niziol et al. 1995; Steenburgh et al. 2000; Juga 2010; Kindap 2010; Alcott et al. 2012; Yeager et al. 2013). Peaking in frequency from October–November and March–April (Alcott et al. 2012), Great Salt Lake Effect (GSLE) snowstorms impact four counties with a combined population of ~1.6 million (U.S. Census 2010), three major Interstate highways, and the Salt Lake City International Airport. The light accumulations and visibility reductions associated with smaller storms affect road and airport transportation, whereas major storms have generated snowfall accumulations of up to 129 cm and have caused major societal impacts in the densely populated lowlands to the south and east of the GSL (Carpenter 1993; Steenburgh et al. 2000; Alcott et al. 2012; Yeager et al. 2013).

Banded GSLE events [as defined by Alcott et al. (2012); a.k.a. shoreline bands (Laird et al. 2003a,b; Laird and Kristovich 2004) or midlake bands (Steenburgh et al. 2000)] have been successfully simulated and examined using Numerical Weather Prediction (NWP) models. Steenburgh and Onton (2001) and Onton and Steenburgh

(2001) used the Pennsylvania State University–National Center for Atmospheric Research fifth generation Mesoscale Model to illustrate the importance of thermally driven circulations in producing a banded GSLE event. More recently, Alcott and Steenburgh (2013) used numerical simulations to reveal a strong synergy between GSL-induced thermal circulations and circulations influenced by the surrounding orography during a banded GSLE event. Nevertheless, despite capturing the morphology of banded events, these studies noted errors in the simulated timing, location, and amount of precipitation that could prove problematic for operational forecasting. In fact, GSLE forecasts generated by operational and locally run real-time modeling systems at grid spacings of 4-km or less have proven unreliable in practice (R. Graham, National Weather Service, personal communication, 2013).

Although there are many potential sources of error in NWP precipitation forecasts, a major contributor can be the Microphysics Parameterization (MP). In modern NWP models, precipitation is generated by the MP scheme and/or convective parameterization. The MP scheme calculates grid-scale tendencies of moist microphysical processes, whereas the convective parameterization attempts to account for sub-grid-scale convective processes (Stensrud 2007). We focus on MP differences by neglecting the convective parameterization, which is possible when using convection-permitting grid spacings [$\mathbf{O}$(1 km)] that resolve some of the convective motions (Weisman et al. 1997; Bryan et al. 2003; Stensrud 2007; Langhans et al. 2012). This approach removes a source of precipitation uncertainty and aids our simulation because convection-permitting grid spacings can better resolve mesoscale topographic effects in simulations over complex terrain (Steenburgh and Onton 2001; Garvert et al. 2005; Colle et al. 2008; Alcott and Steenburgh 2013).

Most MP schemes used for mesoscale modeling are bulk schemes that predict hydrometeor mass mixing ratios and/or number concentrations but assume size distributions based on empirical exponential or gamma distributions (e.g., Lin et al. 1983; Tao et al. 1989; Ferrier 1994; Thompson 2008; Milbrandt and Yao 2005; Morrison et al. 2009; Lim and Hong 2010; Lin and Colle 2011). Single-moment-bulk MP schemes predict the mass of hydrometeors, whereas dual-moment schemes predict both the mass and number concentration. Some MP schemes are hybrids, meaning that some hydrometeors are handled as single moment while others are handled as dual moment. Increasing the number of moments can improve precipitation forecasts, the simulated behavior of convective systems, and orographic precipitation (Morrison et al. 2009; Lim and Hong 2010; Milbrandt et al. 2010; Van Weverberg et al. 2012). The inclusion and treatment of ice hydrometeors (e.g., cloud ice, snow, graupel, hail) improves simulations of squall lines, supercells, and bow echoes (Nicholls 1987; Fovell and Ogura 1988; Tao and Simpson 1989; Szeto and Cho 1994; Liu and Moncrieff 2007; Adams-Selin et al. 2013), and differences in the parameterization of ice behavior influence the accuracy of surface precipitation forecasts (Rutledge and Hobbs 1983; Thompson et al. 2004). As a result, simulations of phenomena such as orographic precipitation, arctic mixed-phase stratus, and squall lines are sensitive to the choice of MP (Colle and Mass 2000; Gilmore et al. 2004; Morrison and Pinto 2005; Lim and Hong 2010; Lin and Colle 2011; Liu et al. 2011; Morrison and Milbrandt 2011; Bryan and Morrison 2012). Simulations of lake-effect precipitation over the Great Lakes are also sensitive to the choice of MP (Theeuwes et al. 2010; Reeves and Dawson 2013).

In this chapter we illustrate the sensitivity of convection-permitting simulations of the GSLE event of 27 October 2010 first described by Alcott and Steenburgh (2013) to the choice of MP. We find significant differences in the amount and coverage of precipitation generated by the MP schemes tested, with the Thompson et al. (2008) MP scheme (THOM) best matching radar estimated precipitation (REP) and gauge data. The other MP schemes produce more precipitation than THOM (and the observed event), with the WRF Double-Moment 6-Class (WDM6; Lim and Hong 2010) scheme generating the largest overprediction. Hydrometeor mass mixing ratios and tendencies implicate the excessive production of graupel as the primary cause of this overprediction. Although based on a single case, these results show that the rate of graupel and snow production strongly influence model quantitative precipitation forecasts of lake-effect storms. The data and methods used for this analysis are summarized in section 3.3, with results presented in section 3.4. Conclusions and a discussion of the implications for operational forecasters and future model evaluation and development are provided in section 3.5.

3.3 Data and Methods

Numerical simulations of the 27 October 2010 GSLE event use the Advanced Research core of the WRF model version 3.4 (Skamarock and Klemp 2008). Following Alcott and Steenburgh (2013), we configure the WRF with three one-way nested domains with 12-, 4-, and 1.33-km grid spacings. The outer domain encompasses the western United States, the 4-km domain stretches from central Nevada to western Colorado and from the Snake River Plain to southern Utah, and the inner domain covers most of the

GSL Basin and surrounding region [see Fig 2.2 of this dissertation or Fig. 2 of Alcott and Steenburgh (2013) for plot of model domains]. The simulations use the Yonsei University planetary boundary layer parameterization (Hong et al. 2006), the Rapid Radiative Transfer Model longwave and shortwave radiation parameterizations (Iacono et al. 2008), and the Noah land surface model (Chen and Dudhia 2001) on all three domains. We use the Kain-Fritsch 2 cumulus parameterization (Kain 2004) on the outer two domains, but neglect the cumulus parameterization in the innermost (1.33-km grid spacing) domain to avoid precipitation sensitivity to cumulus parameterization choice (e.g., Jankov et al. 2005).

We use a similar WRF configuration to Alcott and Steenburgh (2013), but newer versions of the WRF and THOM yield slightly different precipitation results (within 1% for domain-wide mean precipitation and 12% for the areal coverage of precipitation ≥ 10 mm). THOM is then tested against the WDM6, Milbrandt-Yao (MY; Milbrandt and Yao 2005), Goddard (GODD; Tao et al. 1989), Stonybrook University Lin (SBYULIN; Lin and Colle 2011), and Morrison (MORR; Morrison et al. 2009) MP schemes. SBYULIN and MY produced much lower moisture upstream of the GSL than the other MP schemes, which appeared to be caused by greater precipitation fallout over and in the vicinity of mountain ranges to the northwest of the GSL. Because this drier environment represents a nonlocal effect that alters storm dynamics and structure (Onton and Steenburgh 2001; Alcott and Steenburgh 2013), we elected not to include SBUYLIN and MY in the analysis.

All simulations are cold-start initialized at 1800 UTC 26 October 2010 and run for 24 hours. Initial atmospheric and land-surface conditions, as well as lateral boundary conditions, derive from 6-hourly operational North American Mesoscale (NAM) model analyses obtained from NOAA National Operational Model Archive and Distribution System at 12-km horizontal and 25-hPa vertical grid spacing. Following Alcott and Steenburgh (2013), we modified the NAM snow cover and GSL temperature analyses to better match those of the observed event. The saturation vapor pressure over the GSL was also adjusted to account for salinity effects.

Simulations are validated against precipitation observations obtained from the MesoWest cooperative networks (Horel et al. 2002) and radar estimated precipitation (REP) from Weather Surveillance Radar-1988 Doppler (WSR–88D) at Promontory Point, Utah (KMTX; Fig. 2.2b of this dissertation) data downloaded from the National Climatic Data Center NEXRAD archive in level III format (Crum et al. 1993). Precipitation observations were rejected if they failed to meet the quality control standards of the MesoWest network. Ben Lomond Trail in the northern Wasatch Mountains was also rejected subjectively due to unrealistic precipitation data. The GSLE period extended from 0230–1700 UTC 27 October 2010, with precipitation stations reporting at intervals ranging from 5 min to 3 h. GSLE period accumulations are for 0230–1700 UTC for stations reporting at 5-, 10-, and 15-min intervals, and 0200–1700 or 0153–1653 UTC for stations reporting at 1-h intervals. These heterogeneous reporting periods should not strongly influence results since precipitation was light at the beginning and end of the GSLE period.

The REP was calculated from the lowest elevation angle reflectivity based on a reflectivity to liquid equivalent snowfall rate (Z–S) relationship of $Z = 75S^2$ (Rasmussen et al. 2003). Potential sources of error in this estimate include but are not limited to the use of a fixed rather than dynamic Z–S relationship, ground-clutter contamination, partial or total beam blockage, sublimation and evaporation below the elevated radar beam (especially over lowland regions), hydrometeor drift, and the partial or total overshooting of shallow precipitation features, especially at longer ranges (Rasmussen et al. 2003; Germann and Joss 2004). Therefore, the REP provides a benchmark for model comparison, but should not be viewed as ground truth.

Since a convective parameterization is not used, surface precipitation from the 1.33-km grid spacing domain is the sum of hydrometeor species that fall out of the lowest model level. In all MP schemes used this includes rain, snow, graupel, and cloud ice, with MORR adding cloud liquid water. Rain, snow, and graupel dominate the accumulated precipitation. In addition to comparing simulated precipitation with the REP and observed surface precipitation, we extracted time- and space-averaged hydrometeor mass mixing ratio profiles from WRF within the MP subdomain defined in Fig. 3.1 to determine what hydrometeor species contributed to the surface precipitation. To better understand why there were distinct hydrometeor differences between the most and least realistic MP schemes (THOM and WDM6, respectively), the WRF code was modified to output the values of the snow and graupel hydrometeor mass tendency equation source and sink variables. Each source and sink variable parameterizes the hydrometeor mass tendency of a single microphysical process, and each MP scheme has a unique set of variables (Tables 3.1 and 3.2).

3.4 Results

3.4.1 Observed Event

The 27 October 2010 GSLE event occurred in the wake of a baroclinic trough that passed over northern Utah ~0000 UTC 27 October 2010. The trough produced light precipitation that was followed by a cold, moist, northwesterly flow that led to GSLE development after 0230 UTC. From 0230–1200 UTC, the KMTX 0.5° elevation angle reflectivity revealed persistent lake-effect precipitation with a predominantly banded structure [see Fig. 2.4d of this dissertation or Fig. 5 of Alcott and Steenburgh (2013)] and embedded convective cells that reached 40–45 dBZ. The axis of convection remained oriented along the major lake axis just west of Promontory Point and Antelope Island until after 0900 UTC when it shifted westward (see Fig. 3.1 for these and other geographic locations). Reflectivity echoes weakened after 1200 UTC, and no further GSLE precipitation was observed in KMTX data after 1659 UTC.

Observed precipitation (liquid precipitation equivalent) during the GSLE period was between 5 and 15 mm at gauge stations in the northern and eastern Salt Lake Valley and more than 20 mm in the Wasatch Mountains (Fig. 3.2). The REP was comparable (i.e., within 5 mm) to that observed by the gauges in the northern and eastern Salt Lake Valley, but suggested that the largest precipitation amounts extended down the center of the valley where the band was more intense and persistent but no gauge observations were available. The REP underrepresented the precipitation in the central Wasatch Mountains, which could be the result of partial beam blockage, partial beam filling, or the use of a fixed Z–S relationship. Despite this caveat, the REP appears adequate for evaluating the simulations in the Salt Lake Valley.

3.4.2 THOM Simulation

In THOM, simulated GSLE precipitation developed at ~0230 UTC 27 October 2010, continued until ~1700 UTC, and featured a predominantly banded structure oriented from northwest to southeast along the long axis of the GSL, as seen in observations (Fig. 2.4d of this dissertation). The total precipitation from THOM during the GSLE period (Fig. 3.3a) generally compares well with the REP (Fig. 3.2), although the distribution is broader since at times the simulated band drifted further southwest than observed. In addition, the simulated precipitation did not extend as far upstream as indicated by REP.

The maximum accumulation and areal coverage of precipitation ≥ 10, 15, and 20 mm produced by THOM in the GSLE subdomain during the GSLE period are 18.43 mm and 709, 141, and 0 km^2, respectively (Table 3.3). The maximum accumulation compares well with the REP maximum of 19.31, although the THOM maximum is shifted downstream (cf. Figs.. 3.2 and 3.3a).[4] The areal coverage ≥ 10 and 15 mm is somewhat larger than the 317 and 47 km^2 in the REP, respectively, which leads to a larger mean precipitation for THOM (1.22 mm) compared to the REP (0.79 mm). These positive biases, however, partly reflect the poor performance of the REP in the central Wasatch Mountains where THOM produces more precipitation and compares better with gauge observations (Fig. 3.3a). Thus, THOM generally reproduces the total precipitation produced in the GSLE subdomain, but with slight positive bias in the amount and coverage of precipitation over the Salt Lake Valley. The precipitation maximum (≥ 15

---

[4] The absolute REP maximum of 24.43 mm (see Table 3.3) occurred over high terrain in the northern Wasatch Mountains, appeared to be the result of ground clutter, and is considered spurious.

mm) in THOM is shifted downstream over the Salt Lake Valley, whereas the REP maximum is over the southern GSL. However, the REP does not account for hydrometeor drift beneath the radar beam (~1.6 km AGL for the centroid over the south shore of the GSL). Hydrometeor drift could shift the REP maximum ~8 km downstream, close to that of THOM, if we assume a wind speed of 5 m s^{-1} (based on analyzed winds) and a hydrometeor fall speed of 1 m s^{-1}.

3.4.3 Sensitivity to MP Scheme

The GODD, MORR, and WDM6 schemes produce larger maximum, mean, and areal coverage of precipitation than the REP and THOM, with some errors in positioning (Table 3.3; Figs. 3.3b,c,d). GODD generates a modest overprediction of precipitation compared to REP with a maximum and areal coverage of precipitation ≥ 10, 15, and 20 mm of 20.95 mm and 1023, 359, and 33 km^2, respectively (Table 3.3). These values yield a mean precipitation of 1.35 mm, which is only ~10% larger than THOM, but the precipitation area is shifted unrealistically downstream with more precipitation falling over the Utah Valley than observed (cf. Figs. 3.2 and 3.3a,b). MORR overpredicts the maximum precipitation compared to REP and generates a larger areal coverage of precipitation ≥ 15 and 20 mm than the REP, THOM, or GODD (Table 3.3; Fig. 3.3c). The mean precipitation from MORR (1.32 mm) is, however, slightly less than GODD because the area of precipitation ≥ 10 mm is smaller. The precipitation maximum in MORR is also located over the southern portion of the Salt Lake Valley, downstream of the maximum in the REP and THOM (cf. Figs. 3.2 and 3.3a,c). WDM6 produces the largest overprediction with a maximum of 51.5 mm and a large area of precipitation ≥ 40 mm over the northwest Salt Lake Valley (Table 3.3; Fig. 3.3d). WDM6 also produces the largest mean (1.5 mm) and areal coverage of precipitation ≥ 15 and 20 mm (667 and 456 km^2, respectively), although the coverage of precipitation ≥ 10 mm is slightly less than GODD.

3.4.4 Hydrometeor Comparison

To better understand the differences in surface precipitation produced by each MP scheme we produced time- and area-averaged profiles of hydrometeor mixing ratios (i.e., cloud liquid water, cloud ice, rain, snow, and graupel) and total condensate (i.e., cloud liquid water+cloud ice+rain+snow+graupel) within the MP subdomain during the GSLE period. This time and space domain focuses on hydrometeors generated over the GSL and excludes hydrometeors from the pre-GSLE period and orographic precipitation over the surrounding terrain. We also produced cross sections averaged across 8 grid points (~11 km) centered on the bold line segments in Fig. 3.4 at 0600 UTC to illustrate the cloud and precipitation hydrometeor structures within the lake-effect band.

3.4.4.1 Cloud Liquid Water and Cloud Ice

In THOM, cloud liquid water is present from 2–6 km MSL with a maximum near 3 km (Fig. 3.5a). MORR is generally similar to THOM with cloud liquid water present from 2–6 km and a maximum near 3 km (Fig. 3.5a). The GODD profile reveals cloud liquid water present from 1.5–5 km, although values near and above 4 km are much lower than found in THOM and MORR (Fig. 3.5a). The cloud liquid water profiles from the WDM6 simulation extend from 1.5–6 km with the weakest maximum of the three schemes (Fig. 3.5a). Overall, the total mean integrated cloud liquid water in the MP subdomain during the GSLE period is relatively high for THOM and MORR (0.053 and 0.057 kg m^{-2}, respectively) and relatively low for GODD and WDM6 (0.029 and 0.018 kg m^{-2}, respectively).

There is little cloud ice in THOM, and it is restricted to 4–7 km MSL with a maximum that is at least 10 times smaller than seen in the other simulations (Fig. 3.5b; low values from 4–7 km barely discernable from zero at this scale). Cloud ice in MORR is also restricted to 4–7 km, with a maximum near 6 km. In contrast, cloud ice in GODD extends through a deeper layer (3–7 km), and the maximum is the largest of all the schemes (Fig. 3.5b). Cloud ice is distributed broadly from 2–7 km in WDM6 with maxima at 2.5 and 5 km (Fig. 3.5b). Overall and in contrast to the total mean integrated cloud water, the total mean integrated cloud ice in the MP subdomain during the GSLE period is lowest for THOM (0.0006 kg m^{-2}), increases in MORR (0.0095 kg m^{-2}), and is largest for GODD and WDM6 (0.025 and 0.017 kg m^{-2}, respectively).

The 0600 UTC cross section from THOM reveals clouds extending in discreet convective plumes from ~2.5–6 km over the GSL (Fig. 3.6a). Cloud base lowers and cloud depth and coverage increase near and over the southern shore of the GSL (right side of the figure). The lack of significant cloud ice in this cross section and the profiles presented in Fig. 3.5 is consistent with the THOM scheme's use of the Cooper (1986) ice nucleation approach, which was chosen over the Meyers et al. (1992) approach because it produces less cloud ice (Thompson et al. 2004).

The GODD cross section similarly reveals convective towers over the GSL with the cloud base lowering and cloud depth and coverage increasing near and over the southern shore of the GSL (Fig. 3.6b). However, cloud ice is the dominant cloud hydrometeor at temperatures near or below -15° C. The dominance of cloud ice at temperatures below -15° C is consistent with the GODD saturation adjustment technique, which allows cloud ice to form but prevents condensation of cloud liquid water at temperatures < -15° C (Tao et al. 2003). The temperature restriction in GODD explains the abrupt transition in the cloud ice and cloud liquid water profiles near 3.5km and the -15° C level (Figs. 3.5a,b).

The cross section from MORR reveals convective towers over the lake stretching from ~2.5–6.5 km with cloud ice mostly above 4.5 km at temperatures below ~-20° C (Fig. 3.7a). As in the other schemes, the cloud depth and coverage increase over the southern shore of the GSL. MORR and THOM use the Cooper (1986) ice nucleation approach and freeze cloud liquid water into cloud ice following the calculations of Bigg (1953), although the THOM implementation of Bigg (1953) may generate less cloud ice via this pathway than MORR, as suggested by Liu et al. (2011). MORR also uses the Meyers et al. (1992) cloud ice contact nuclei concentration relationship to freeze cloud liquid water drops via contact nucleation, and collectively the additional pathway for cloud ice production plus the different calculation of Bigg (1953) result in more cloud ice in MORR than THOM.

The cross section from WDM6 shows a similar tendency for cloud base to lower and depth to increase near the GSL shore, but cloud liquid water coverage and amounts are generally lower than the other schemes (Fig. 3.7b, see also Fig. 3.5a). Cloud ice is found throughout the cloud depth and therefore occurs in a broader range of temperatures than in any other scheme. This occurs because WDM6 allows cloud ice to form at temperatures as high as 0°C, and the assumed ice nuclei number concentration is fairly constant with temperature so that more (less) ice can be produced at higher (lower) temperatures than other schemes (Hong et al. 2004).

3.4.4.2 Rain

Rain concentrations are very small in all of the schemes but, as will be shown later, can contribute to the creation and growth of snow and graupel. In THOM, rain is present at low concentrations (< 0.003 g kg^{-1}) from the lowest model level up to ~5.5 km with a weak maximum near the surface and a very broad maximum at ~3.5 km (Fig. 3.5c). The rain profiles in GODD and MORR exhibit similar maxima near the surface and at 3 and 4 km, respectively (not distinguishable in Fig. 3.5c). This bimodal structure is also evident in WDM6, although the maximum near the surface is much stronger. Two processes produce the bimodal rain profile in all four schemes: the autoconversion of cloud liquid water to rain within updrafts creating rain aloft, and the melting of snow and graupel near the surface where temperatures are > 0°C (see Figs. 3.6, 3.7, 3.8, 3.9). The much larger near-surface maximum in WDM6 likely reflects the larger precipitation rates and higher melt efficiency in the scheme, which in turn leads to greater rain mixing ratios below the freezing level.

3.4.4.3 Snow and Graupel

Snow and graupel account for most of the total condensate and precipitation in all four schemes, with differences in snow and graupel production strongly influencing the amount and distribution of precipitation. In THOM, snow extends from 1.5–7.5 km, with the majority of the snow mass above 3.5 km and a broad maximum at ~5–6 km (Fig. 3.5d). The large mass of snow aloft coupled with a relative lack of cloud ice at similar altitudes (cf. Figs. 3.5a,d) implies that THOM is very efficient at increasing snow mass through the collection of cloud ice, depositional growth, and/or the conversion of cloud ice to snow, as evaluated in section 3.4.5.1. Snow is also present throughout the depth of the snowband in GODD with a maximum near 5 km, although snow concentrations are much larger than THOM at all altitudes (Fig. 3.5d). MORR also produces snow through the depth of the snowband with a maximum of snow mixing ratio at 5.5 km and a profile similar to THOM and GODD, but with less snow overall (Fig. 3.5d). The least amount of snow is produced by WDM6, which generates a bimodal snow profile with maxima at 2.5 and 4.5 km (Fig. 3.5d).

Graupel in THOM extends from the lowest model level to 7 km, reaches a maximum at 5 km (Fig. 3.5e), and represents 22.5% of the total frozen hydrometeor mass (i.e., snow+graupel+cloud ice) in the MP subdomain. GODD produces the least amount of graupel with relatively consistent mixing ratios ~0.0025 g kg^{-1} from the surface to 7 km (Fig. 3.5e) contributing only 5.1% of the total frozen hydrometeor mass in the MP subdomain. Graupel in MORR is present through the depth of the snowband, has a maximum near 5 km, and comprises 42.4% of total frozen hydrometeor mass (Fig. 3.5e). WDM6 produces the most graupel in terms of the profile maximum (Fig. 3.5e) and percentage of total frozen hydrometeor mass in the MP subdomain 58.1%. The maximum in WDM6 is slightly lower (~4–4.5 km) with much larger mixing ratios at lower levels. The dominance of graupel mass in WDM6 compared to the other schemes, especially THOM and GODD, implies that WDM6 is more efficient at graupel creation, collection, and growth, as discussed in section 3.4.5.2.

The relative production of graupel and snow strongly influences the amount and distribution of precipitation. MORR and WDM6 produce more graupel than THOM and GODD, as well as larger precipitation maxima and areas of precipitation ≥ 20 mm (Table 3.3; Fig. 3.3). They also produce more elliptically shaped precipitation regions with smaller aspect ratios (i.e., length/width). In contrast, THOM and GODD produce more snow with smaller precipitation maxima and areas of precipitation ≥ 20 mm that are either nonexistent or very small. The precipitation areas produced by THOM and GODD are more elongated with larger aspect ratios.

3.4.4.4 Total Condensate and Precipitation

Total condensate from all MP schemes extends from the lowest model level to nearly 8 km (Fig. 3.5f). THOM exhibits secondary and primary maxima near 3 and 5 km, the former due primarily to the cloud liquid water maximum at 3 km (Fig. 3.5a) and the latter due primarily to the more elevated snow maximum (Fig. 3.5d). GODD reaches a pronounced maximum at 5 km with snow as the primary contributor (cf. Figs. 3.5d,f). The amount of total condensate in GODD is larger than the other schemes from 3–7 km. MORR also exhibits a maximum near 5 km, which is primarily a result of snow and graupel (cf. Figs. 3.5d,e,f). WDM6 has primary and secondary maxima at 2.5 and 4.5 km, with the former maximum occurring at the lowest height of the four schemes (Fig. 3.5f). WDM6 also has larger total condensate values below 2.5 km, which reflects a more rapid generation and fallout of precipitation compared to the other schemes (e.g., Fig. 3.3).

Cross sections of rain, snow, and graupel reveal the structure of the simulated GSLE band at 0600 UTC. The THOM cross section shows graupel, snow, and rain extending from the southern GSL over the Salt Lake Valley (Fig. 3.8a). Over the southern GSL and northern Salt Lake Valley, snow is primarily above 1.5 km, but is carried downstream and falls out over the southern Salt Lake Valley and Wasatch Mountains (see Alcott et al. 2013). The rain found above the freezing level at heights from 2.5–5 km over the GSL and northern Salt Lake Valley is generated in updrafts and contributes to graupel generation as shown in section 3.4.5.2.

The majority of precipitation in GODD is found further downstream than in THOM and near and downstream of the southern shore of the GSL (Fig. 3.8b). Over the Salt Lake Valley, there is generally more snow than the other schemes. Large snow mixing ratios (> 0.54 g kg^{-1}) extend downstream over the Utah Valley (~120 km) where GODD produces more precipitation than the other schemes (see also Fig. 3.3).

Most precipitation in MORR is also found near and downstream of the southern shore of the GSL, with generally lower snow and greater graupel mixing ratios than in THOM or GODD (Fig. 3.9a). Although characterized by lower mixing ratios than found in THOM, MORR generates some rain in storm updrafts that likely converts to graupel. In addition, a significant amount of snow and graupel is present over the southern Salt Lake Valley that result in the downstream displacement of the surface precipitation maximum found in MORR compared to THOM and GODD (see also Fig. 3.3).

Graupel, snow, and rain in WDM6 extend from the southern GSL over the Salt Lake Valley (Fig. 3.9b). Although similar in horizontal extent to THOM, the depth of precipitation is shallower. Over the Salt Lake Valley, snow mixing ratios are lower and rain mixing ratios higher than found in the other schemes. Peak graupel concentrations (> 0.54 g kg^{-1}) over the Salt Lake Valley are comparable to those in MORR but cover a smaller area. At this time, the coverage and peak simulated reflectivity in WDM6 is smaller than in MORR (Fig. 3.4), but graupel production and mixing ratios are larger at times in WDM6 during the simulation, resulting in a larger total precipitation maximum (Fig. 3.3).

3.4.5 Hydrometeor Mass Tendencies

THOM and WDM6 represent two ends of the spectrum of precipitation outcomes from the four MP schemes. THOM produces the most realistic precipitation forecast compared to the REP and gauge observations, whereas WDM6 produces the least realistic precipitation forecast. In addition, THOM generates more snow, whereas WDM6 generates more graupel. To understand these two contrasting solutions, we examined the source and sink variables for snow and graupel in THOM and WDM6 (Tables 3.1 and 3.2) averaged over the MP subdomain during the GSLE period. We grouped these variables into creation, growth (negative growth implies mass loss), and melt categories and identified which variables (i.e., parameterized physical processes) are responsible for the contrasting solutions.

3.4.5.1 Snow

Snow creation in THOM occurs from ~4–7 km with a pronounced maximum at ~6 km (Fig 3.10a). The primary creation term is snow conversion from ice (prs_iau), with snow from deposition (prs_ide) negligible[5]. In contrast, WDM6 creates snow from ~2–7.5 km with maxima at 3 and 4.5 km. Snow conversion from ice (psaut) and snow from rain collecting cloud ice (praci) contribute to this snow creation, with the former larger at most model levels. In WDM6, rain collecting cloud ice can produce snow or graupel depending on the mixing ratio of rain. In this case, rain collecting cloud ice results in snow. In contrast, THOM does not include this process as a snow creation term. Despite a larger amount of cloud ice available to WDM6 (Fig. 3.5b), creation of snow by conversion of ice to snow is smaller than in THOM, implying lower efficiency of conversion of cloud ice to snow in WDM6.

Snow growth is also quite different between THOM and WDM6 (Fig. 3.10b). In THOM, snow growth occurs within the simulated cloud layer from ~2.5–7 km, with a maximum ~5 km and small losses below cloud base and above cloud top (Fig. 3.10b). Water vapor deposition (prs_sde) is the largest contributor to snow growth within the cloud layer above ~5 km, whereas snow collecting liquid water (prs_scw) dominates near and below 4 km. Sublimation (i.e., prs_sde < 0) produces the losses above and below cloud base. The WDM6 profile is similar to THOM, but with much weaker growth from 3.5–7 km, stronger growth from 2–3.5 km, and weak growth from the lowest model level to ~1.8 km where THOM has losses. The largest contributor to snow growth within the WDM6 cloud layer is snow collecting liquid water (paacw) at and below 5.5 km. Water vapor deposition (psdep) and snow collecting cloud ice (psaci) are secondary contributors except near cloud top. The weak growth from the lowest model level to ~1.8 km is

---

[5] To avoid ambiguities, we use WRF variable names (e.g., prs_iau) in this discussion. See Tables 3.1 and 3.2 for variable names cross-referenced with the physical processes they parameterize.

produced by snow collecting rain (psacr), which for clarity is not included in Fig. 3.10b. This contribution to snow growth is overwhelmed by melting, which results in a net loss of snow and increase in rain below the freezing level (see Fig. 3.9b).

3.4.5.2 Graupel

Graupel creation in THOM occurs from 2–6 km with a maximum just above 5 km produced primarily by the freezing of rain into graupel [prg_rfz (Fig. 3.11a)]. At other levels, the freezing of rain into graupel is less important, and graupel creation results from other processes (i.e., prg_scw, prg_rci, prg_rcs). Graupel creation by WDM6 occurs in a shallower layer (~4–6.5 km), is much larger than in THOM, and is due almost exclusively to the freezing of rain into graupel [pfrzdtr (Fig. 3.11b)]. Despite the smaller graupel creation rates, THOM has more rain available above 2 km than WDM6 (Fig. 3.5c), illustrating the less efficient creation of graupel in THOM compared to WDM6.

In THOM graupel growth occurs from 2.5–6.5 km with a maximum at 5 km (Fig 3.11b). Graupel collecting cloud liquid water (prg_gcw) is the primary growth term. Loss of graupel mass occurs below 2.5 km and reflects losses due to sublimation (prg_gde), rain collecting graupel (prg_rcg), and, to a lesser extent, the Hallet and Mossop process (prg_ihm). Graupel growth in WDM6 is much larger than THOM and occurs from 2–6.5 km with a broad maximum from 3.5–4.5 km (Fig. 3.11b). The primary graupel growth terms are graupel collecting cloud liquid water (paacw) and graupel collecting rain (pgacr). Graupel collecting rain (pgacr) is also responsible for the secondary maximum near the model's lowest half sigma level, although it is partially offset by melting (see Fig. 3.9b).

Ultimately, the disparity in graupel mass between THOM and WDM6 occurs primarily because graupel creation from the freezing of rain is much larger in WDM6 than THOM. The remaining physical processes that create and grow graupel are larger in WDM6 than THOM, but not nearly as disparate as the freezing rain into graupel. This result is broadly consistent with Liu et al. (2011), who suggested that high graupel production by several MP schemes (including WDM6) in regional climate simulations over Colorado reflects an improper implementation of the Bigg (1953) temperature and volume dependence for droplet freezing. In contrast, THOM uses a lookup table that more closely matches the approach of Bigg (1953), yielding smaller graupel concentrations.

3.5 Conclusions

Simulations of the 27 October 2010 GSLE event show considerable sensitivity to the choice of MP. The THOM scheme produces a precipitation distribution and amount that best matches radar-derived precipitation estimates and gauge observations. The other MP schemes produce larger maximum precipitation values than THOM, with the WDM6 producing the largest overprediction. In addition, the areal coverage of precipitation ≥ 10, 15, and 20 mm produced by the MORR, GODD, and WDM6 schemes were larger than THOM at every threshold, with WDM6 the largest outlier.

The relative production of snow and graupel strongly influence the distribution and amount of precipitation. THOM and GODD produce more snow and the most realistic (i.e., banded) precipitation features, although GODD shifts precipitation too far downstream. MORR and WDM6 produce more graupel and less realistic (i.e., more elliptical) precipitation features. Source and sink terms for snow and graupel show that WDM6 creates graupel at a rate 10 times larger than THOM near the top of the simulated cloud layer and grows graupel mass at a rate four times larger than THOM at lower altitudes in the cloud layer. Liu et al. (2011) asserted the WDM6 (and several other MP schemes) improperly applied Bigg's (1953) temperature and volume dependence for drop freezing to create graupel by freezing raindrops. Our results further support the Liu et al. (2011) assertion and the approach used by THOM.

These findings suggest that THOM is the best choice for simulating this GSLE case and may be a good choice for other events. More GSLE events need to be simulated, however, to determine the overall reliability of THOM relative to other schemes. In addition, as suggested by Reeves and Dawson (2013), improved knowledge and observations of the degree of riming and hydrometeor fall speeds is needed to validate snow and graupel production, growth, and fallout. Aircraft, polarimetric radar, and ground-based microphysical samples collected during the 2013–2014 Ontario Winter Lake-effect Systems (OWLeS) field campaign east of Lake Ontario, as well as polarimetric radar data from KMTX and ice crystal observations from the Multi-Angle Snowflake Camera in the Wasatch Mountains southeast of the GSL (Garrett et al. 2012), may provide a foundation for future MP scheme improvements.

Table 3.1. Snow source and sink variables in THOM and WDM6.

	MP Source/Sink Variables		Physical Process
	THOM	WDM6	
Creation	prs_iau	psaut	Snow converted from ice
	prs_ide	N/A	Snow from deposition of water vapor onto cloud ice
	N/A	piacr	Snow from cloud ice collecting rain
	N/A	praci	Snow from rain collecting cloud ice
Growth	prs_sde	psdep	Water vapor deposition to/sublimation from snow
	prs_scw	paacw	Snow collecting cloud water
	prs_sci	psaci	Snow collecting cloud ice
	prs_rcs	psacr	Snow collecting rain
		pracs	Rain collecting snow
	N/A	pgacs	Graupel collecting snow
	N/A	pseml	Enhanced snow melt
	N/A	psevp	Evaporation of melting snow
	N/A	pgaut	Graupel conversion to snow
	prs_ihm	N/A	Hallet and Mossop process snow loss
Melt	prr_sml	psmlt	Snow melt

Table 3.2. Graupel source and sink variables in THOM and WDM6.

	MP Source/Sink Variables		Physical Process
	THOM	WDM6	
Creation	prg_scw	pgaut	Graupel converted from snow
	prg_rci	praci	Graupel from rain collecting cloud ice
		piacr	Graupel from cloud ice collecting rain
	prg_rcs	pracs	Graupel from rain collecting snow
		psacr	Graupel from snow collecting rain
	prg_rfz	pfrzdtr	Freezing of rain into graupel
Growth	prg_gde	pgdep	Water vapor deposition to/sublimation from graupel
	prg_rcg	pgacr	Graupel collecting rain
	prg_gcw	paacw	Graupel collecting cloud water
	prg_ihm	N/A	Hallet and Mossop process graupel loss
	N/A	pgacs	Graupel collecting snow
	N/A	pgevp	Evaporation of melting graupel
	N/A	pgeml	Enhanced graupel melt
	N/A	pgaci	Graupel collecting cloud ice
Melt	prg_gml	pgmelt	Graupel melt

Table 3.3. Precipitation statistics from the GSLE-subdomain during the GSLE period (0230–1700 UTC 27 October 2010). The 24.43 mm REP value occurs over the Northern Wasatch, not within the GSLE band, and is considered spurious. The 19.31 mm REP value occurs over the western shore of Antelope Island and provides a better estimate for comparison.

Precip. Data	Max Precip. (mm)	Mean Precip. (mm)	Percent Change of Mean Precip.	Area ≥ 10 mm Precip. (km^2)	Area ≥ 15 mm Precip. (km^2)	Area ≥ 20 mm Precip. (km^2)
REP	24.4(19.3)	0.8	N/A	317	47	1
THOM	18.4	1.2	N/A	709	141	0
GODD	21.0	1.4	9.4	1023	359	33
MORR	28.1	1.3	7.0	950	530	238
WDM6	51.5	1.5	24.4	996	667	456

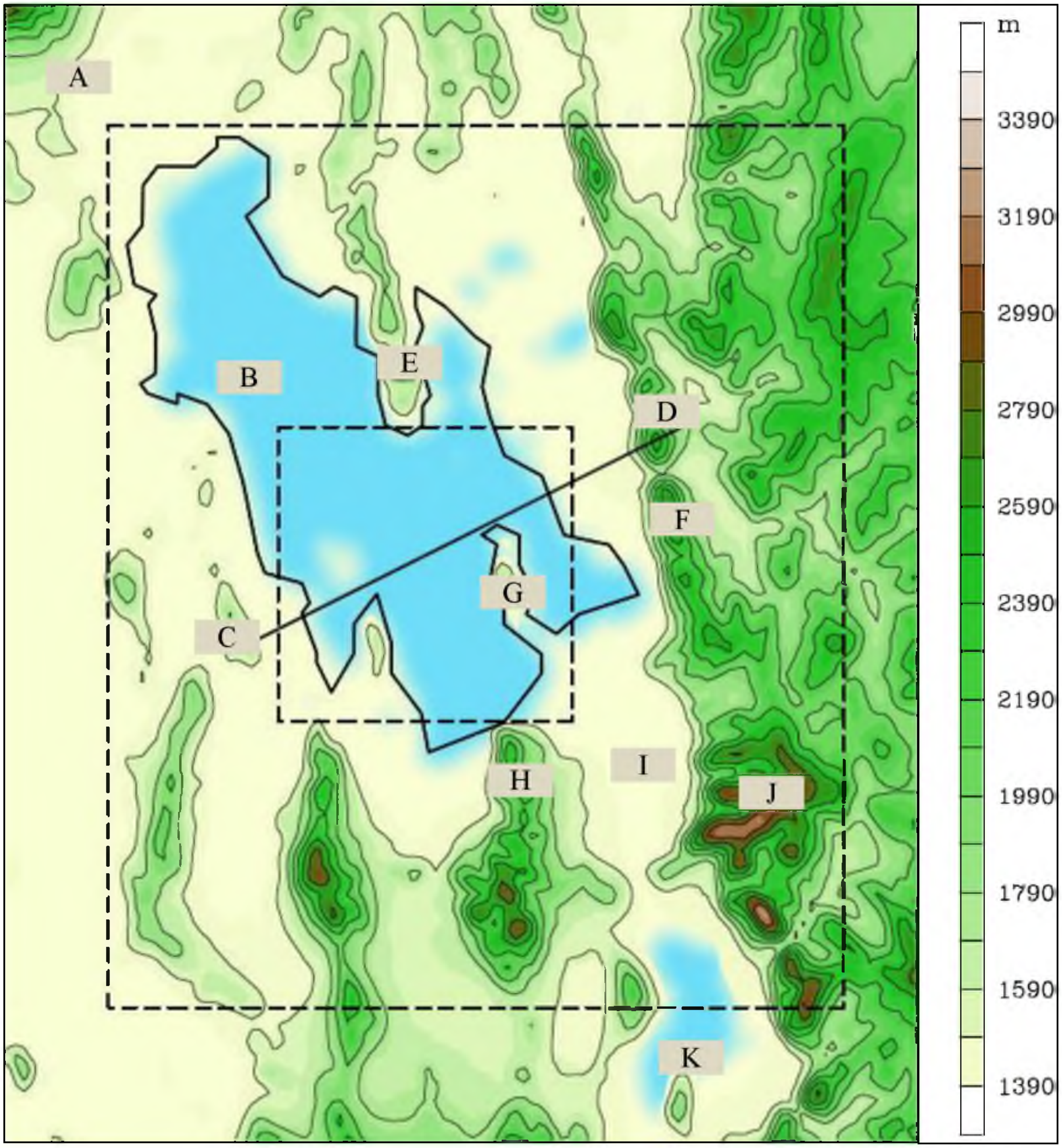

Fig. 3.1. Major geographic features, validation domains, and analysis transects within the study region including the GSLE subdomain (A), MP subdomain (B), cross section CD, Promontory Point (E), northern Wasatch Mountains (F), Antelope Island (G), Oquirrh Mountains (H), Salt Lake Valley (I), central Wasatch Mountains (J), and Utah Valley (K). Elevation (m) contoured and shaded following scale at right.

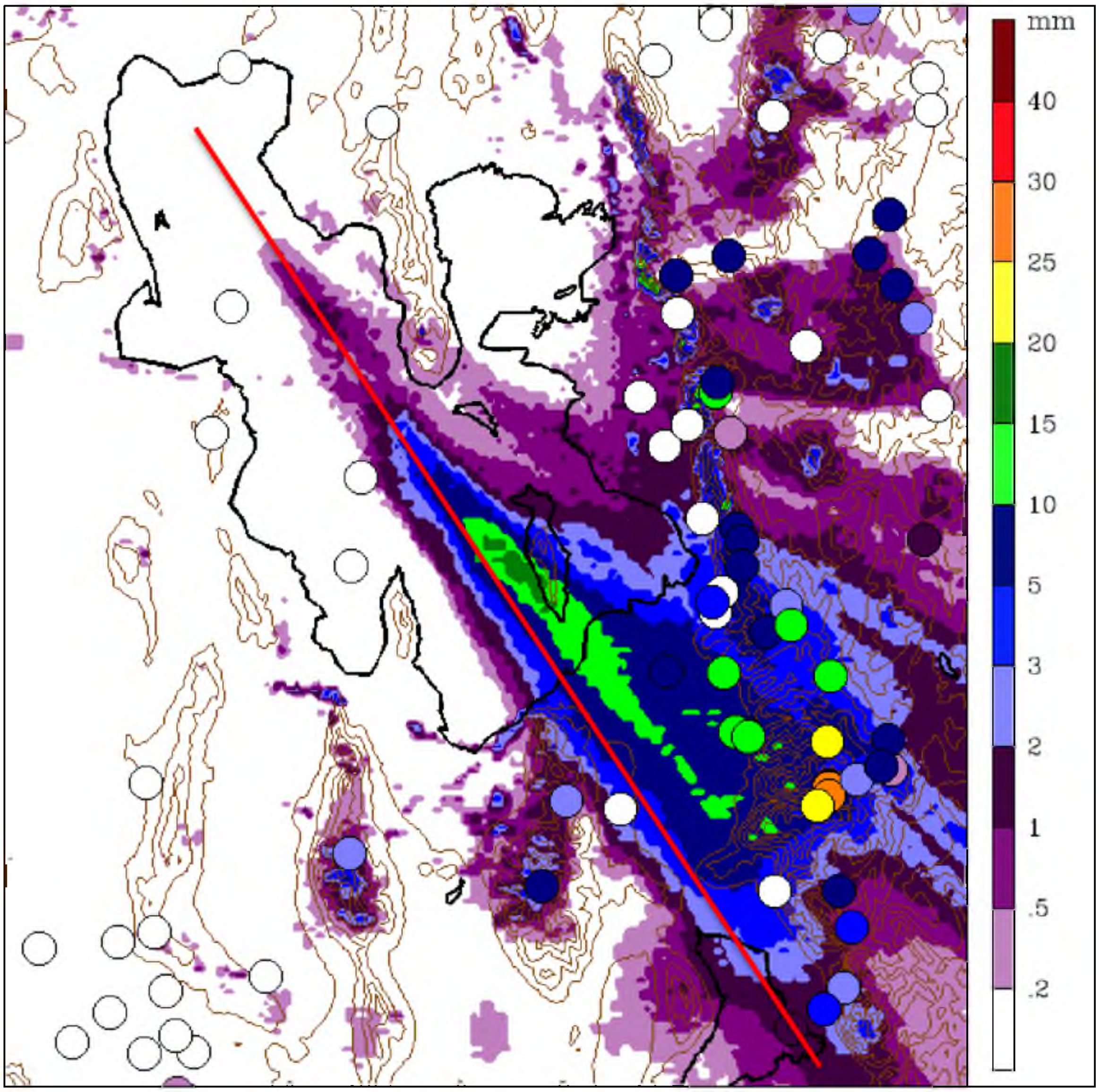

Fig. 3.2. REP (mm, shaded following scale at right) during the GSLE period (0230–1700 UTC 27 October 2010) with gauge-measured precipitation indicated by color-filled dots (see section 3.3, Data and Methods, for accumulation periods). Red line overlaid as reference.

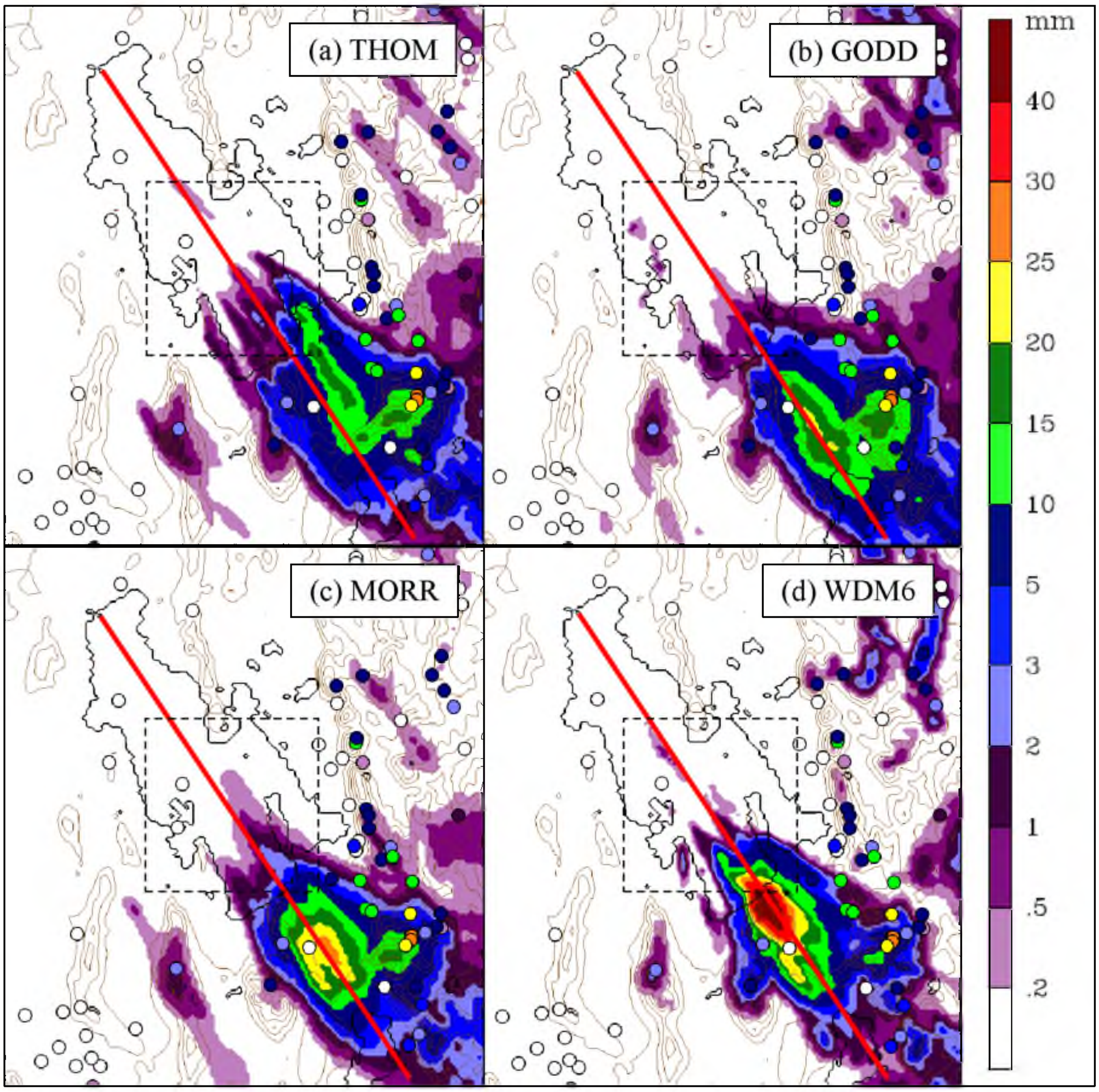

Fig. 3.3. Simulated precipitation (mm, shaded following scale at right) during the GSLE period from (a) THOM, (b) GODD, (c) MORR, and (d) WDM6. Gauge-measured precipitation indicated by color-filled dots. Red line and MP subdomain outline overlaid for reference.

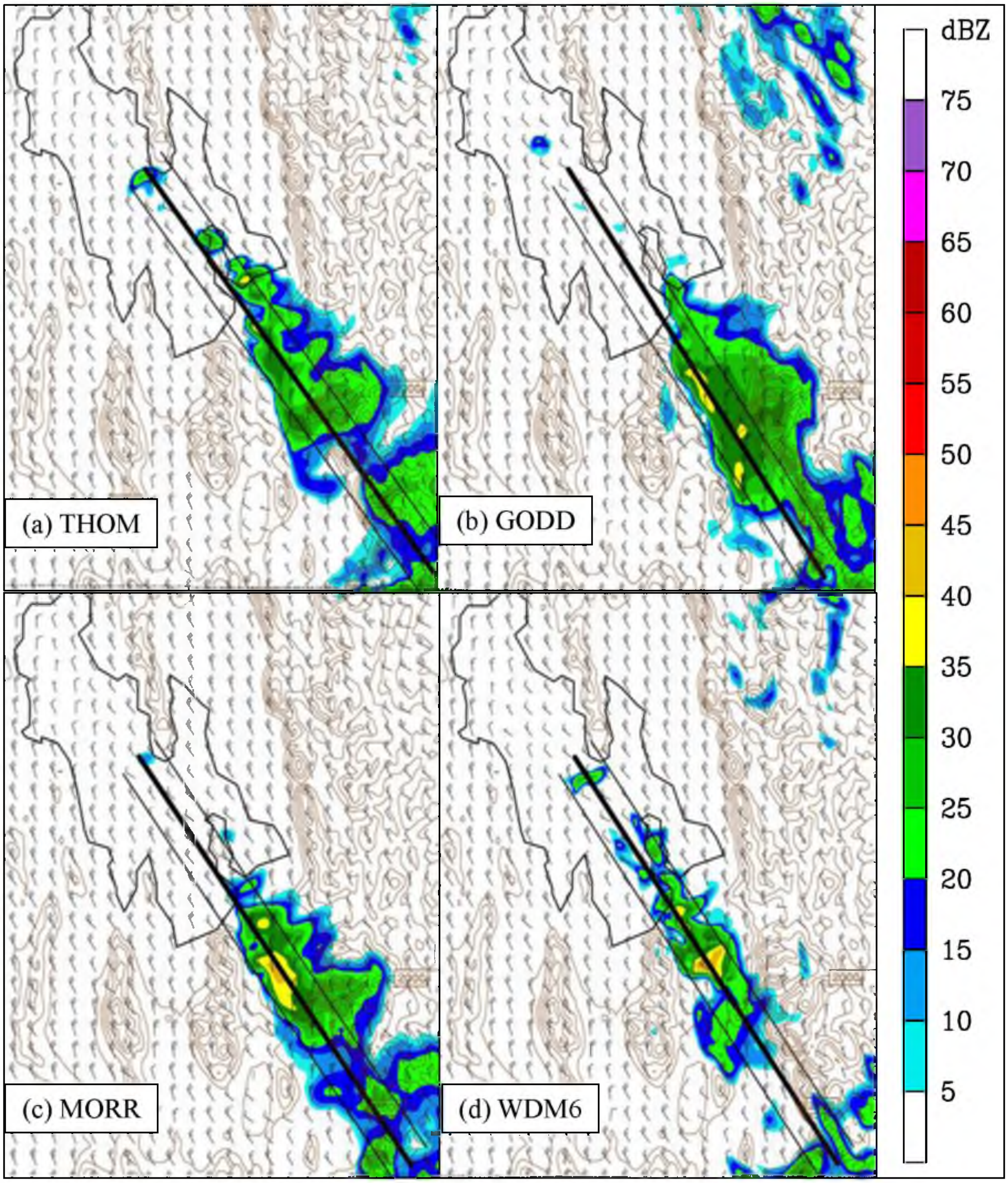

Fig. 3.4. Simulated 2.5-km MSL reflectivity (dBZ, shaded following scale at right) and winds (full and half barb denote 5 and 2.5 m s-1, respectively) at 0600 UTC of 27 October 2010 from (a) THOM, (b) GODD, (c) MORR, and (d) WDM6. Center and horizontal averaging region of cross section used in Figs. 3.6, 3.7, 3.8, and 3.9 indicated by bold and thin lines, respectively.

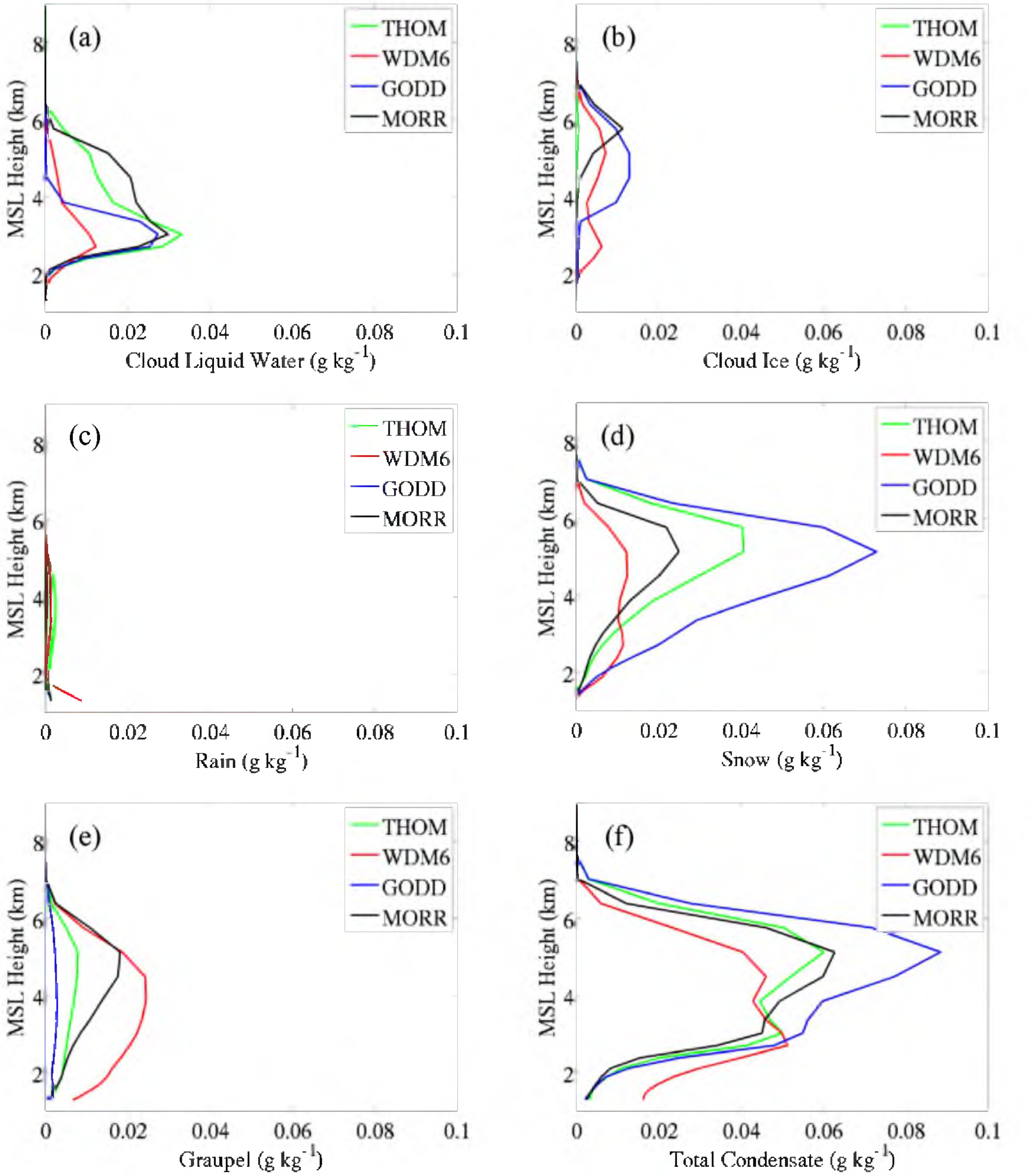

Fig. 3.5. Vertical profiles of MP-subdomain- and GSLE-period-averaged mixing ratio of (a) cloud ice, (b) cloud liquid water, (c) rain, (d) snow, (e) graupel, and (f) total condensate (cloud ice + cloud liquid water + rain + snow + graupel).

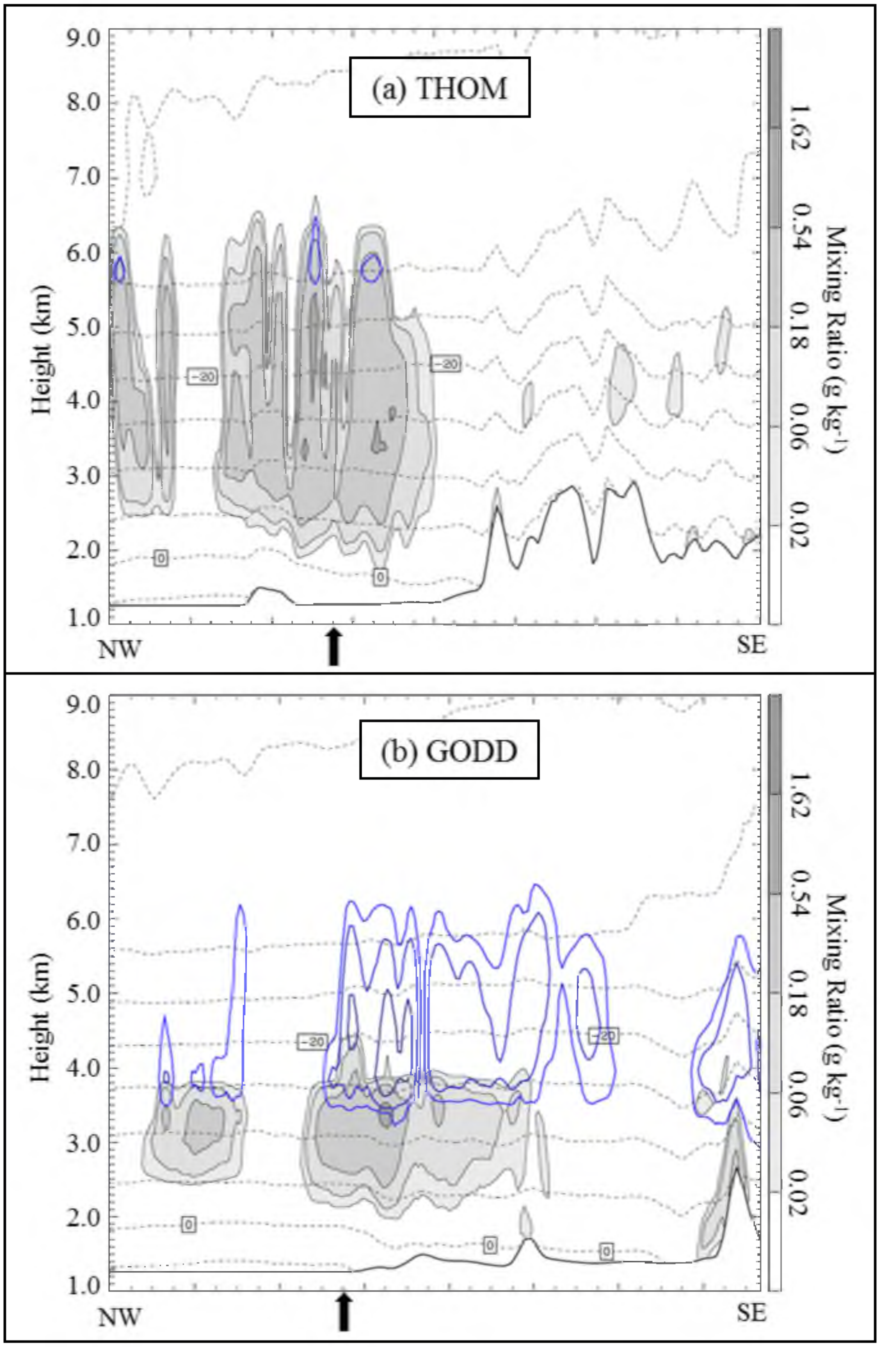

Fig. 3.6. Vertical cross section of cloud liquid water mixing ratio (g kg^{-1} shaded following scale at right), cloud ice mixing ratio (light to dark blue contours at .02, .06, .18, .54, and 1.62 g kg^{-1}), and temperature (° C, black dashed contours every 5° C) averaged in region identified in Fig. 3.4 at 0600 UTC 27 October 2010 for (a) THOM and (b) GODD. Dark arrows indicate the approximate location of the southern shore of the GSL.

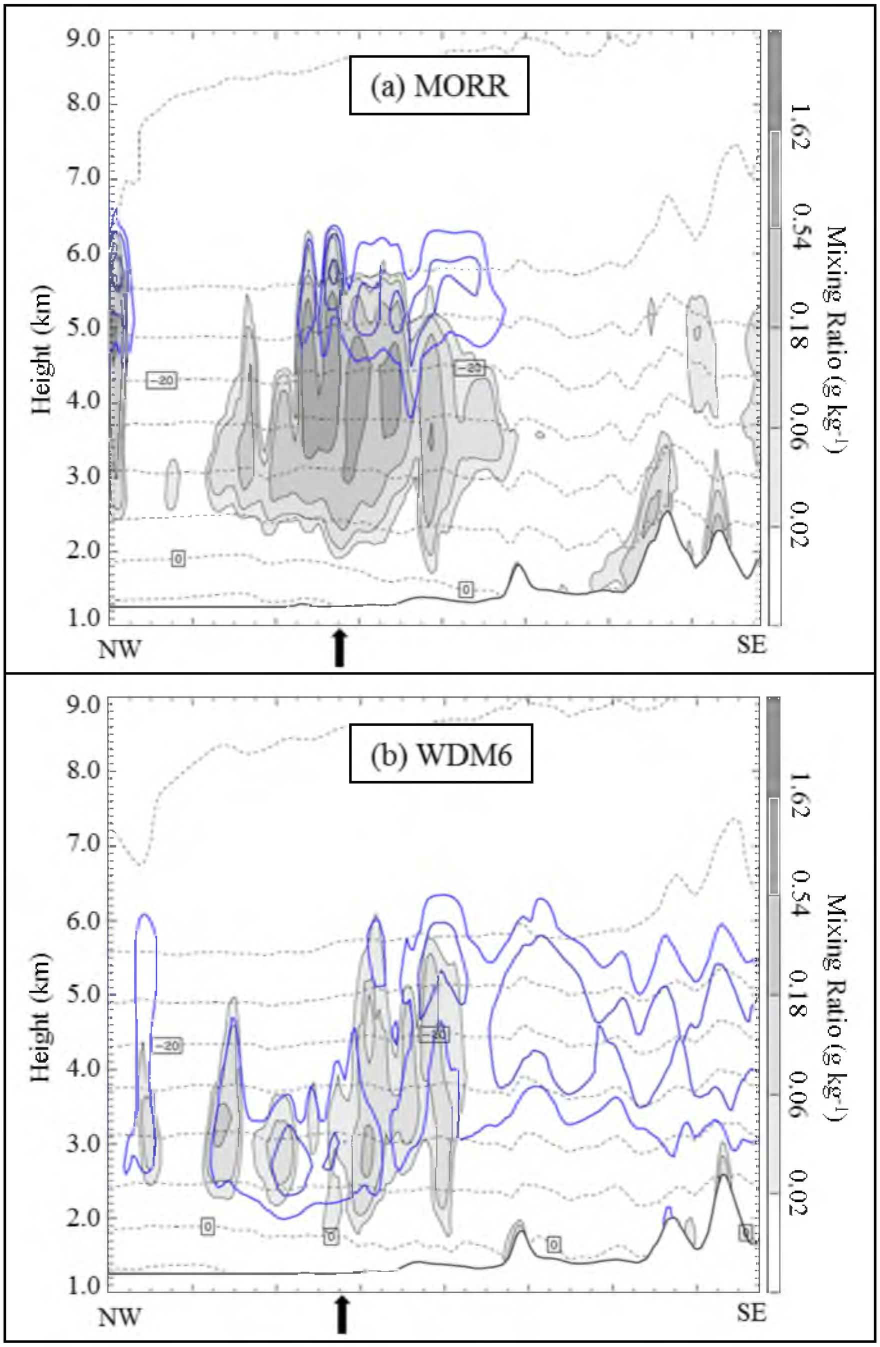

Fig. 3.7. Same as Fig. 3.6 for (a) MORR and (b) WDM6.

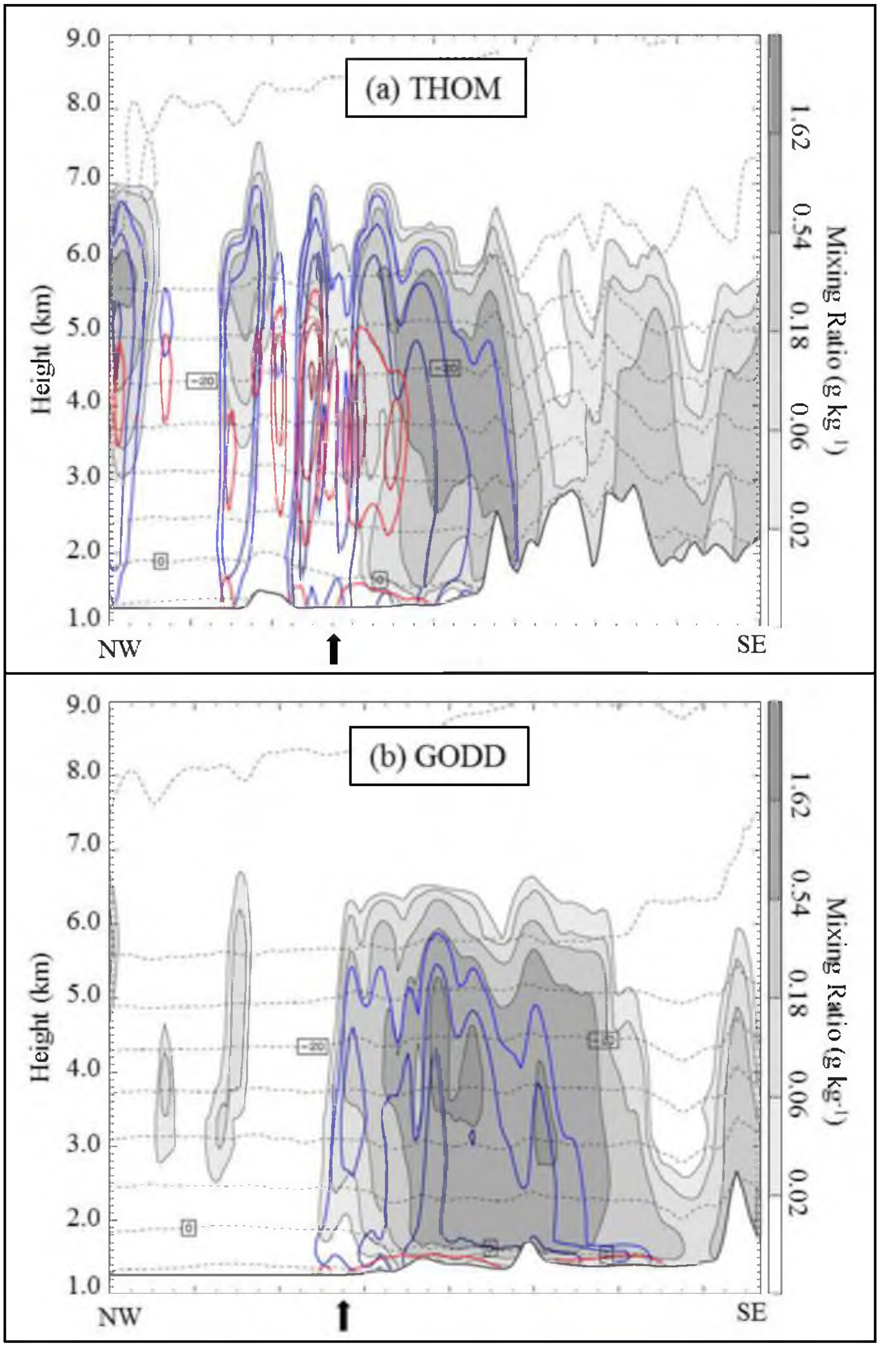

Fig. 3.8. Same as Fig. 3.6 except snow mixing ratio (g kg^{-1}, shaded following scale at right), graupel mixing ratio (light to dark blue contours at .02, .06, .18, .54, and 1.62 g kg^{-1}), and rain mixing ratio (pink to maroon contours at .02, .06, .18, .54, and 1.62 g kg^{-1}) for (a) THOM and (b) GODD. Dark arrows indicate the approximate location of the southern shore of the GSL.

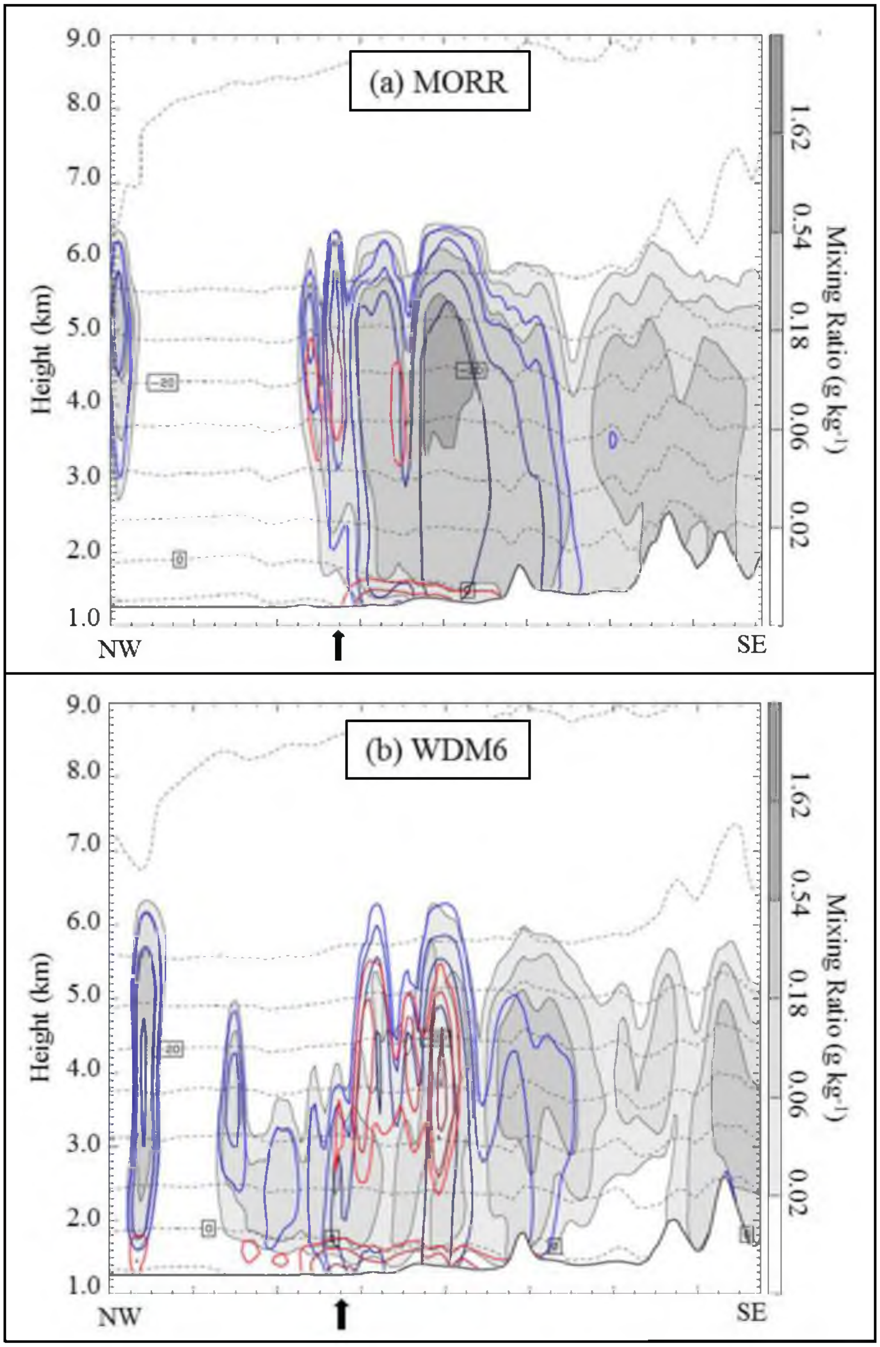

Fig. 3.9. Same as Fig. 3.8 for (a) MORR and (b) WDM6.

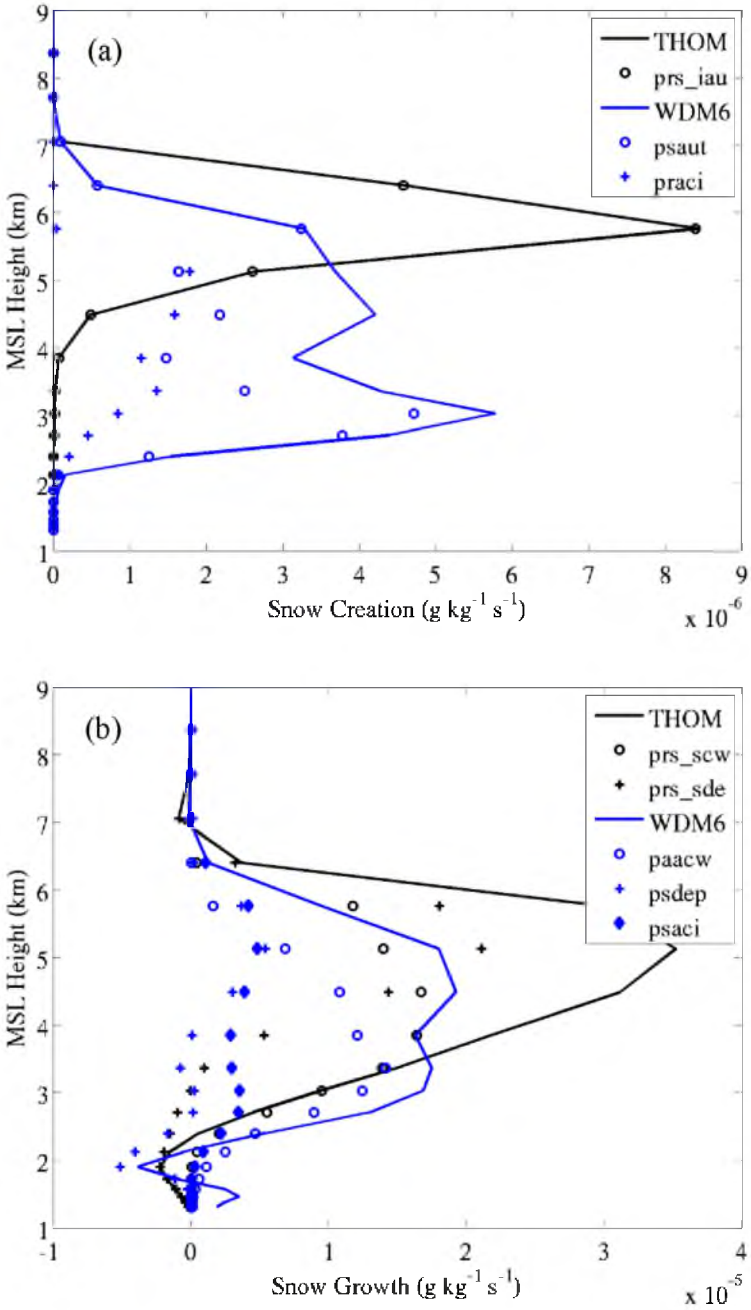

Fig. 3.10. Vertical profiles of MP-subdomain- and GSLE-period-averaged (a) snow creation (sum of all creation variables in Table 1, solid lines) and significant snow creation variables (symbols at upper right) and (b) snow growth (sum of all growth variables in Table 3.1, solid lines) and significant snow growth variables (symbols at upper right) for THOM (black) and WDM6 (blue).

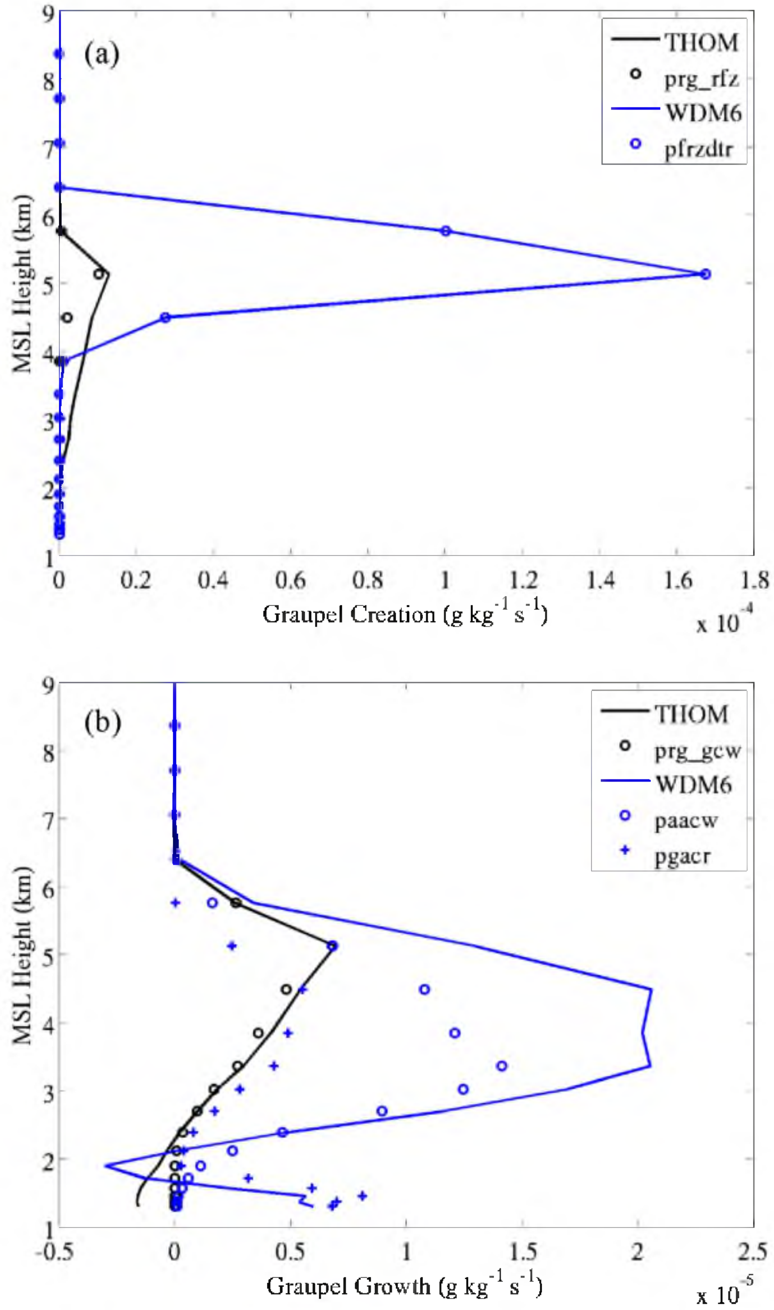

Fig. 3.11. Vertical profiles of MP-subdomain- and GSLE-period-averaged (a) graupel creation (sum of all creation variables in Table 2, solid lines) and significant graupel creation variables (symbols at upper right) and (b) graupel growth (sum of all growth variables in Table 3.2, solid lines) and significant graupel growth variables (symbols at upper right) for THOM (black) and WDM6 (blue).

CHAPTER 4

FACTORS INFLUENCING THE POSITION OF THE 27 OCTOBER 2010 GREAT SALT LAKE EFFECT BAND

4.1 Introduction

The position of the Great Salt Lake Effect (GSLE) band varies in the simulations described in Chapter 3. Here we examine the factors that may contribute to these variations as they may be important for operational forecasting and illustrate that band position may be affected by more than just the ambient upstream flow direction, as suggested by climatological analyses (e.g., Steenburgh et al. 2000).

4.2 Discussion

In the simulation using the Thompson et al. (2008) scheme (THOM), the axis of maximum precipitation extends from Antelope Island into the Salt Lake Valley, east of the overlaid reference line (Fig. 4.1). In contrast, this axis is near or to the west of the reference line in the other simulations. Lake-effect bands are typically produced and collocated with convergence produced by thermally driven land breezes (Hjelmfelt and Braham 1983), although terrain-driven circulations also affect the convergence over the Great Salt Lake (GSL) in this case (Alcott and Steenburgh 2013). The divergence pattern produced in each simulation at the beginning of the GSLE period (0230 UTC 27 October 2010) shows that the axis of maximum precipitation is collocated with low-level convergence (i.e., a divergence minima strip) aligned roughly parallel to the long axis of the lake in each simulation (cf. Figs. 4.1 and 4.2). Since the terrain is identical in all simulations, we hypothesize that differences in the intensity of the land breezes from the eastern and western shores may affect the position of the resulting convergence and lake band.

The 1.5-km (near lake surface) pressure difference relative to THOM for the simulations using the Morrison et al. (2009) (MORR), Goddard (GODD; Tao et al. 1989), and the Weather Research and Forecasting (WRF) Double-Moment 6-Class (WDM6; Lim and Hong 2010) schemes reveals differences in surface pressure that are consistent with the shift in position of the land breeze circulation and convergence associated with the GSLE band (Fig. 4.3). The GODD–THOM difference reveals lower pressure in GODD over the southern end of the lake that is centered on the reference line and west-southwest of the maximum precipitation in THOM (cf. Figs. 4.1 and 4.3). MORR–THOM shows lower pressure in MORR over the western half of the lake, west of the reference line. WDM6–THOM reveals a stronger low pressure anomaly in WDM6 than either GODD or MORR that is consistent with the westernmost GSLE band position in WDM6. One factor potentially contributing to these differences in pressure and the position of the convergence and GSLE band is the thermodynamic structure resident over and around the GSL in the wake of the antecedent baroclinic trough passage. This difference likely arises from contrasts in the evolution of the baroclinic trough from 1800 UTC 26 October 2010–0230 UTC 27 October 2010.

The baroclinic trough in the GODD, MORR, and WDM6 simulations produces less precipitation than THOM over the central west coast of the lake, whereas more precipitation occurs in MORR and WDM6 over the eastern shore (Fig. 4.4). The lack of precipitation and associated evaporative cooling in GODD, MORR, and WDM6 west of the lake causes warmer air near the surface over the western shore (A) than seen in THOM (Fig. 4.5). In addition to surface warming, GODD, MORR, and WDM6 are also warmer aloft. During the same period, MORR and WDM6 produce more precipitation and evaporative cooling over the eastern shore (B) of the lake (Fig. 4.5). The thermal environment (warmer to the west and cooler to the east) at the start of the event favors a stronger land breeze from the eastern shoreline and a weaker land breeze from the western shoreline. In fact circulation vector differences show a westward shift of the surface convergence zone in all three simulations relative to THOM (Fig. 4.5).

Another factor potentially contributing to the position of the convergence is the intensity of precipitation produced by the GSLE band. The westward displacement of the GSLE band, and the simulated maximum precipitation amounts increase from THOM to GODD, then MORR, and finally WDM6 (Fig. 4.1). Onton and Steenburgh (2001) found a feedback between latent heat release and convective circulation in a GSLE event after running a simulation without latent heat release and noting a decrease in convective circulation and precipitation. It is not clear why enhancement of the convective circulation would shift the band westward, but it may be that latent heat release in updrafts within the band interact with the land-breeze modification noted above, altering the position of the band. The differences in precipitation intensity may also be caused by differences in cold pool strength beneath the band, which could theoretically alter storm structure as horizontal vorticity generated by the cold pool interacts with the ambient vorticity akin to vorticity driven circulations in mesoscale convective systems (Rotunno et al. 1988; Weisman 1992).

The THOM simulation may also be influenced by the factors noted above. THOM produces more precipitation over the eastern shore than the radar estimated precipitation (REP) from 1800 UTC 26 October 2010–0230 UTC 27 October 2010 (Fig. 4.6). GSLE precipitation in THOM occurs further west than REP (Fig. 4.7). The pre-GSLE precipitation difference (REP–THOM) is similar to the differences in MORR–THOM and WDM6–THOM, as is the resulting GSLE band displacement.

In summary, all of our simulations reveal a shift westward of the GSLE band compared with radar estimated precipitation suggesting the thermodynamic structure of the environment at GSLE onset and intensity of the GSLE band influence the band position. This is somewhat different than previous work, which showed orographic and land-breeze circulations were responsible for GSLE structure and position (Onton and Steenburgh 2001; Steenburgh and Onton 2001; Alcott and Steenburgh 2013). These simulations indicate that additional physical processes may alter the known forcings and therefore band position (i.e., antecedent thermodynamic structure altering the land breeze), and/or convective dynamics may influence band position by generating GSLE band-centric circulations. Further work is required to better understand the roles of the processes discussed herein and to better understand all processes responsible for GSLE band position.

Finally, forecasters should note our findings because knowing that a shift in simulated convergence may be influenced by simulated GSLE-predecessor precipitation and/or GSLE intensity provides insight for interpreting numerical weather prediction model depictions of a GSLE event. Comparing differences in observed versus simulated convergence may allow the forecaster to diagnose the actual over-lake convergence location and adjust the simulated GSLE band location to more accurately forecast precipitation location.

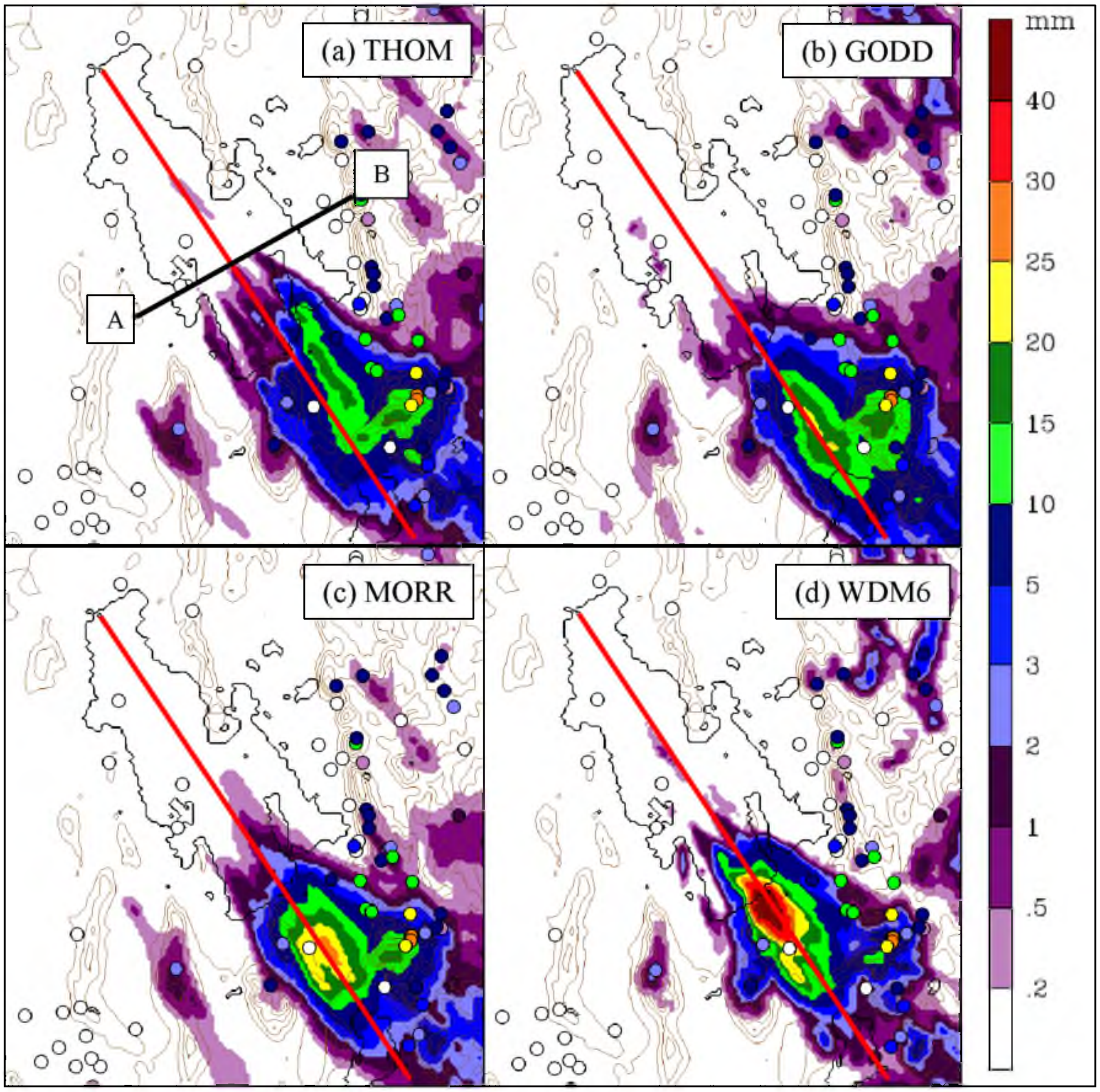

Fig. 4.1. Total precipitation accumulated during the GSLE period for the (a) THOM, (b) GODD, (c) MORR, and (d) WDM6 MP simulations. Color-filled dots indicate gauge-measured precipitation. Red line overlaid as reference. Black Line A-B [in (a)] is the cross section for Fig. 4.4.

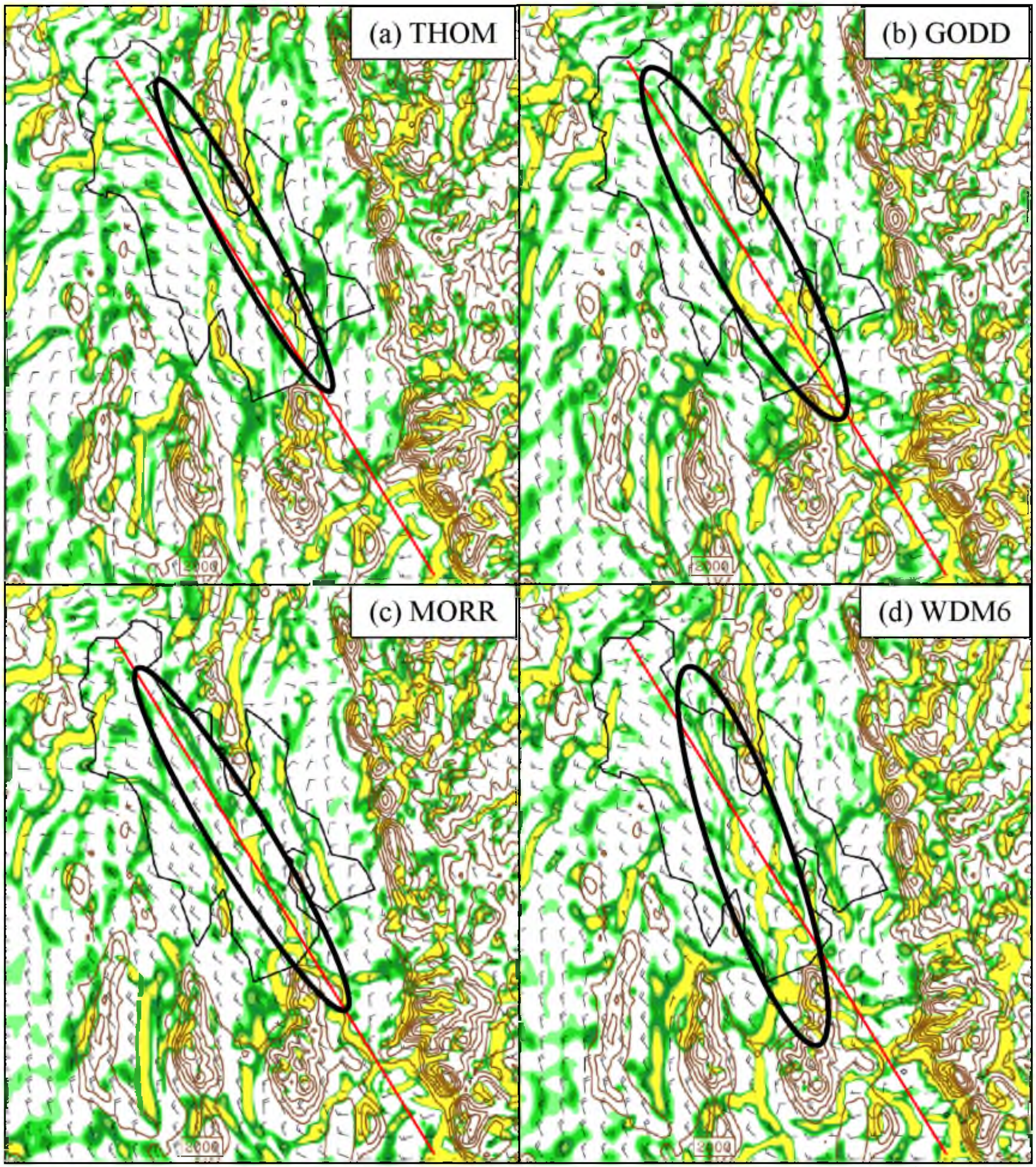

Fig. 4.2. Divergence averaged through the lowest 2 model levels (green < 0 s^{-1}, yellow < -110 s^{-1}, interval -20 s^{-1}, shaded) and lowest model level wind barbs (full barb = 5 m s^{-1}) for the (a) THOM, (b) GODD, (c) MORR, and (b) WDM6 MP simulations at 0230 UTC 27 October 2010. Ovals identify low-level convergence and the red line overlaid as reference.

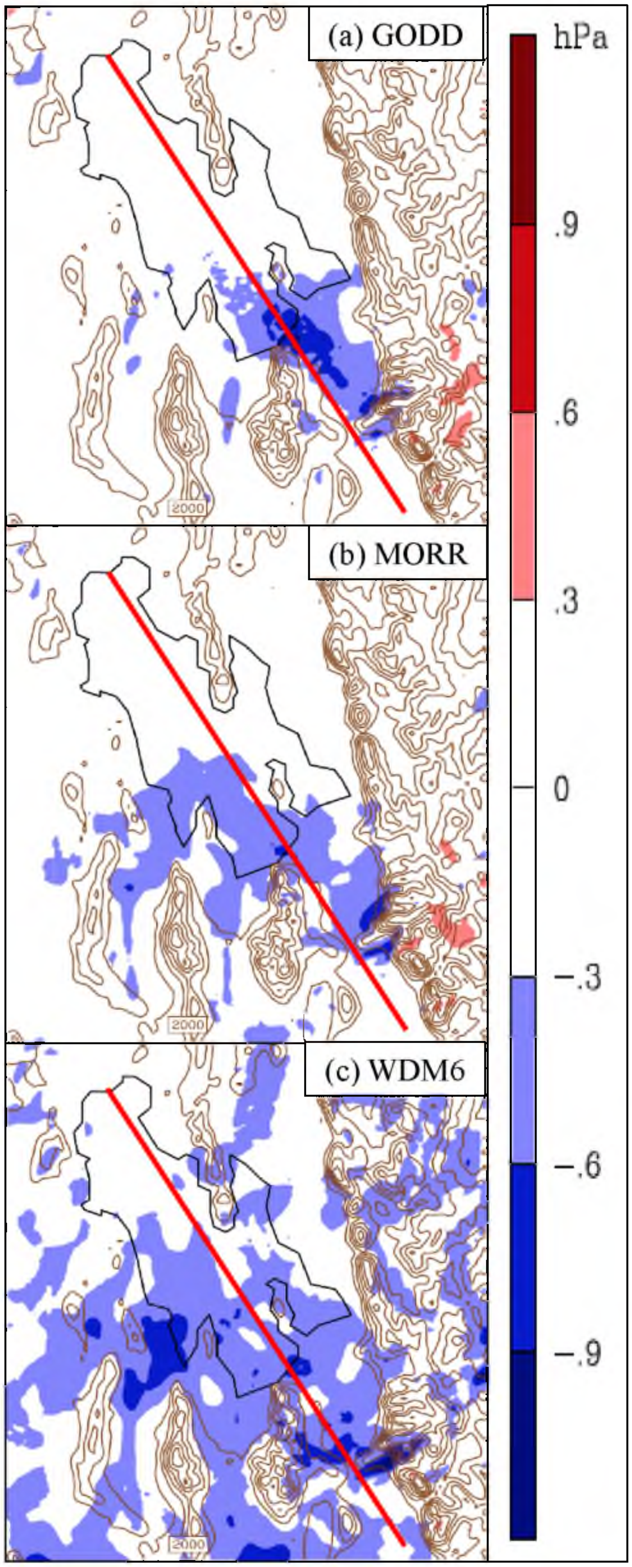

Fig. 4.3. 1.5 km Pressure difference (a) GODD–THOM, (b) MORR–THOM, and (c) WDM6–THOM at 0230 UTC 27 October 2010. Red line overlaid as reference.

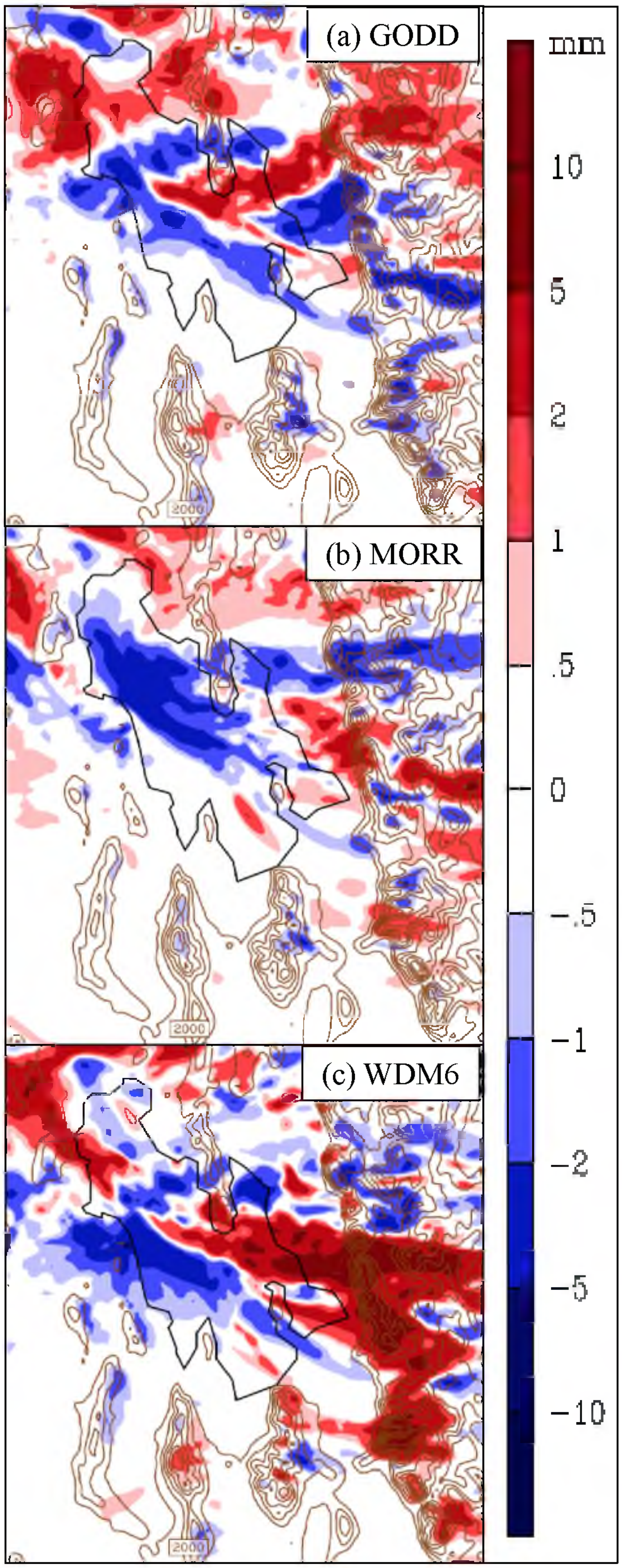

Fig. 4.4. Pre-GSLE period total precipitation difference (a) GODD–THOM, (b) MORR–THOM, and (c) WDM6–THOM.

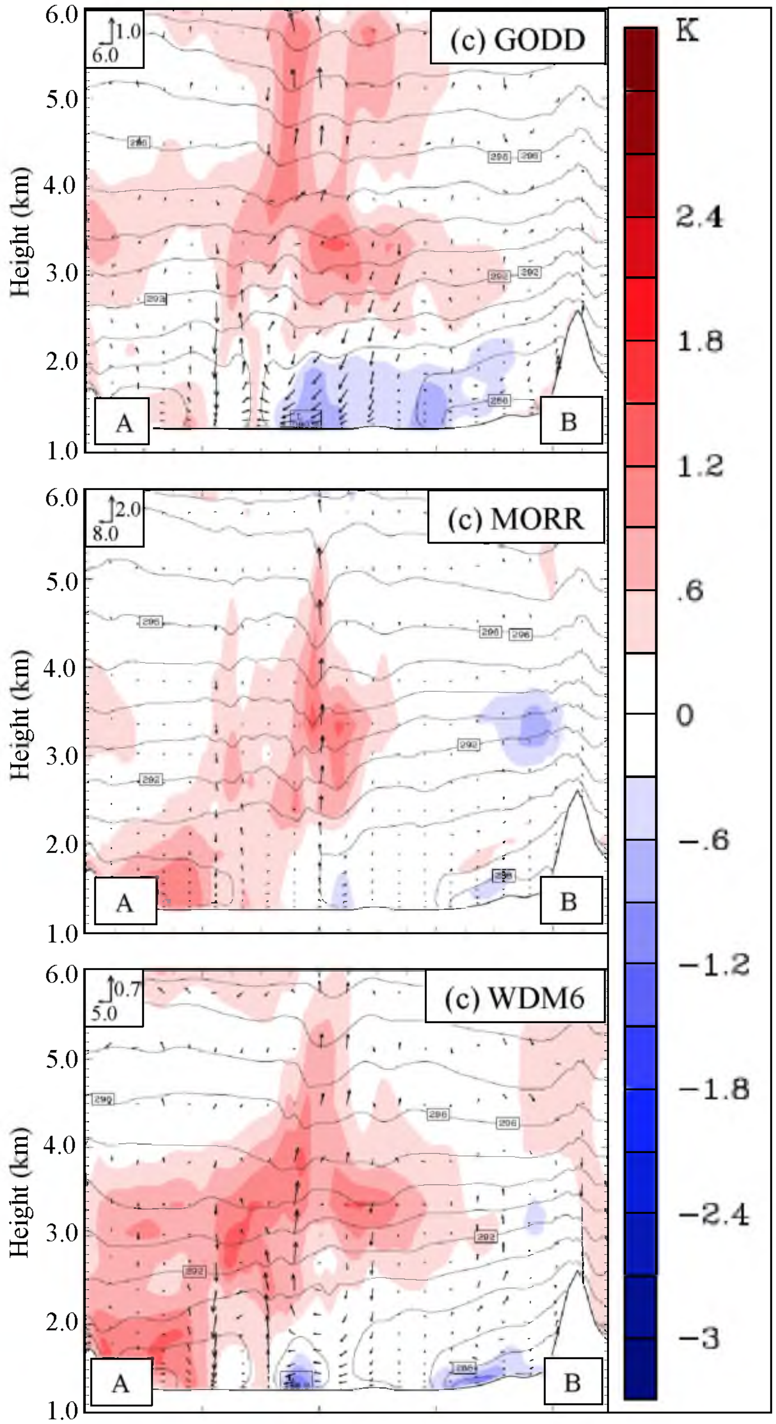

Fig. 4.5. 8-km horizontal average cross section A-B of contoured potential temperature K, contours), scheme minus THOM potential temperature (K, shaded, scale at right), and scheme minus THOM circulation (vectors m s^{-1}, legend inset), and at 0230 UTC 27 October 2010 for the following schemes (a) GODD, (b) MORR, and (c) WDM6.

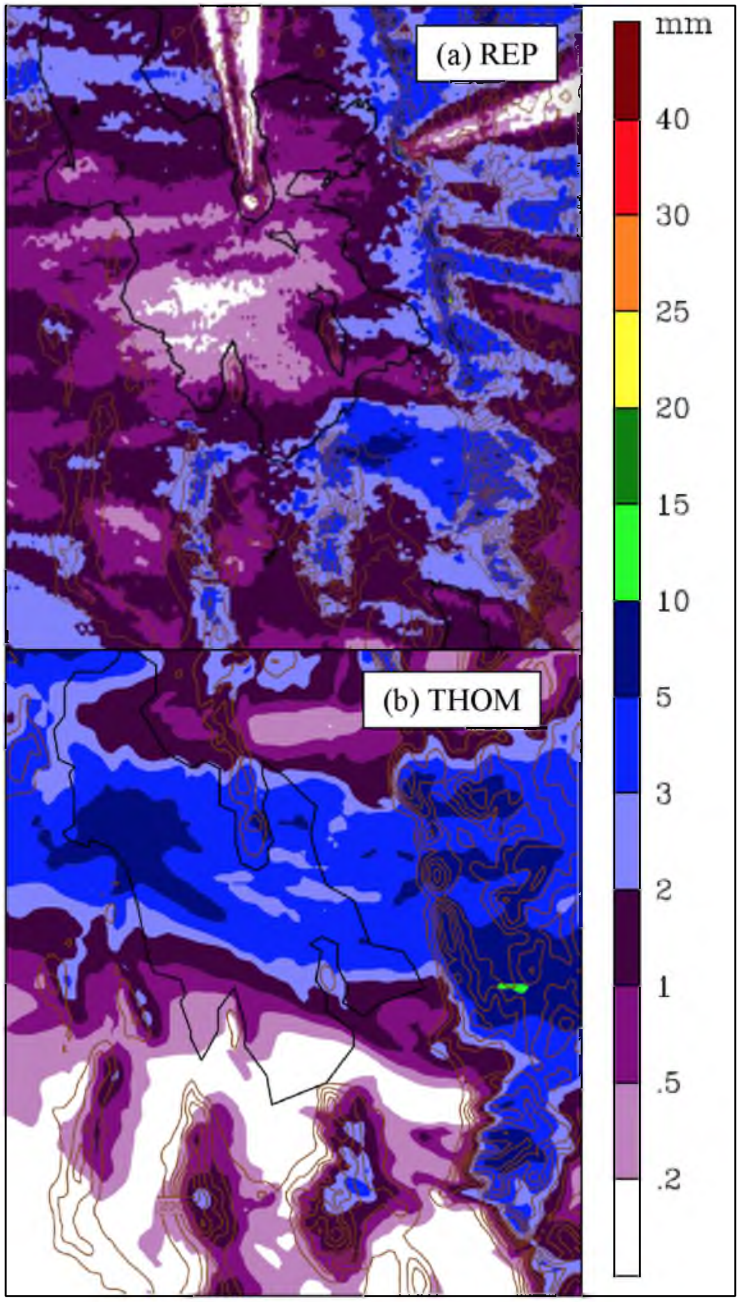

Fig. 4.6. Pre-GSLE period total precipitation from (a) REP, (b) THOM simulation.

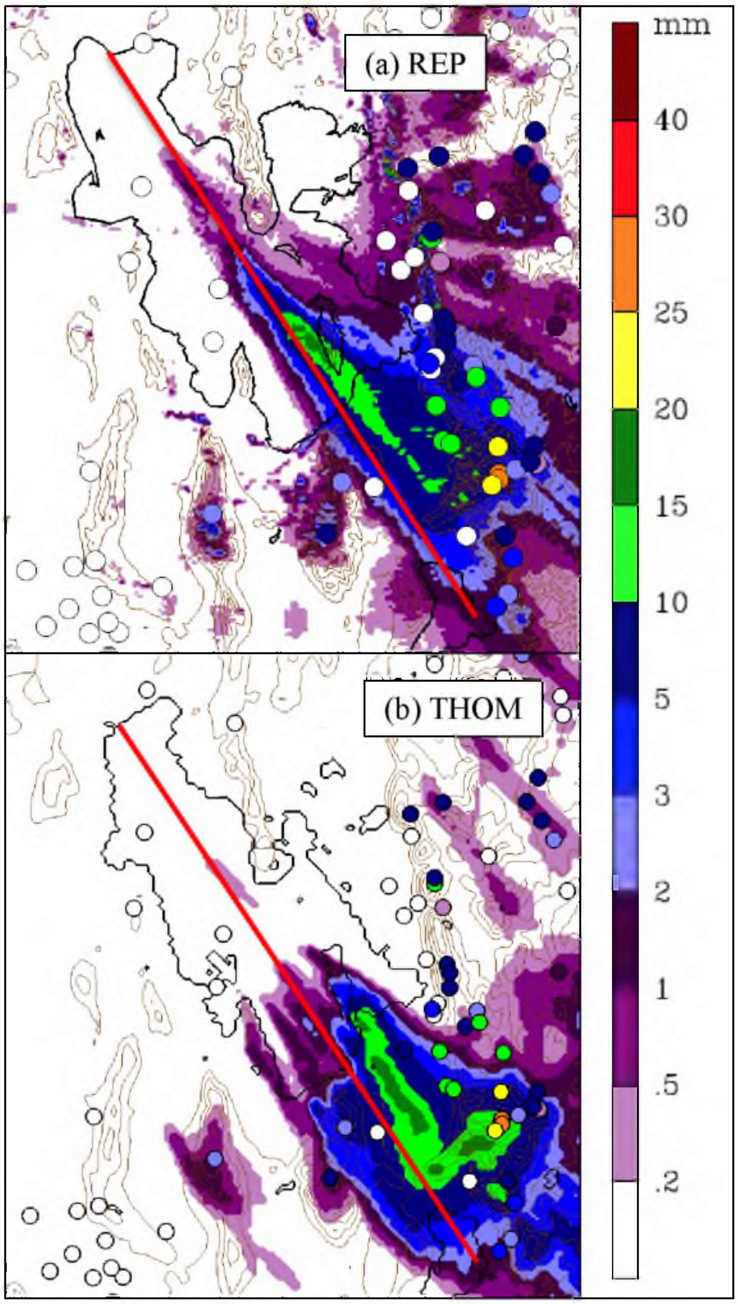

Fig. 4.7. Total precipitation accumulated during the GSLE period for the (a) REP and (b) THOM. Color-filled dots indicate gauge-measured precipitation. Red line overlaid as reference.

CHAPTER 5

CONCLUSION

5.1 Summary of Findings

The Advanced Research Core of the Weather Research and Forecasting (WRF) model shows little skill simulating banded and nonbanded GSLE events, but despite the overall low skill, simulations of banded GSLE events show similar skill as other mesoscale precipitation simulations (Colle et al. 2000; Gallus 2002; Aligo et al. 2009; Clark et al. 2010, Stratman et al. 2013). Simulations of nonbanded GSLE events record lower skill than simulations of banded events, and only one out of eight simulations produced a nonbanded precipitation feature. On average, WRF overpredicts precipitation coverage and amount and produces precipitation southward (rightward and downwind relative to the flow) of radar estimated precipitation (REP) by ~ 25 km. WRF is also biased towards creating banded precipitation features (Three of eight simulations of nonbanded GSLE events produced banded precipitation features and overforecast precipitation amounts.).

Unfortunately for forecasters, the low skill exhibited in our simulations may be an optimistic view of WRF skill in operational GSLE forecasts. Pessimism is warranted because we excluded events where conditions suggested that GSLE was likely but GSLE was not observed. It is likely that in some of these events WRF would have generated

GSLE precipitation and a false alarm. We also limited the influence of large-scale error growth by using North American Mesoscale model analyses for lateral boundary conditions. In an operational setting large-scale error growth is not constrained in this manner, further reducing model skill.

The consistently low skill of the WRF simulations raises questions about GSLE predictability. The mesoscale nature of GSLE likely limits predictability, since small-scale error growth from imprecise initial conditions, as well as land- and lake-surface uncertainty, rapidly decreases simulation skill in mesoscale simulations (Lorenz 1982; Anthes 1986; Stamus et al. 1992; Emanuel 1994; Mullen et al. 1999; Onton and Steenburgh 2001; Holt et al. 2006; Hacker 2010). If low predictability is inherent to GSLE as in other mesoscale processes, improvements to the currently deterministic approach to simulating GSLE [e.g., Microphysics Parameterization (MP) improvements, removing WRF biases], while necessary, may not significantly improve skill. In addition, the inability to consistently create nonbanded GSLE precipitation features when simulating nonbanded GSLE events also hinders GSLE predictability because nonbanded GSLE occurs more frequently than any other morphology (Alcott et al. 2012).

The WRF showed a strong sensitivity to the choice of MP scheme in our simulations of the 27 October 2010 GSLE event. In this event, simulations using the Thompson et al. (2008) (THOM) MP scheme produce a precipitation distribution and amount that best matches REP and gauge observations. The other MP schemes produce larger maximum precipitation values and larger areal coverage of precipitation than THOM, with the WRF Double-Moment 6-Class (WDM6) producing the largest overprediction. Our findings reveal a broad range of precipitation outcomes caused primarily by the choice of MP scheme and suggest that THOM is the best choice for simulating GSLE in this event. This result, combined with results from other cool-season precipitation simulations over the western United States suggest that THOM may be the best choice for simulating GSLE and cool-season precipitation over northern Utah (Liu et al. 2011; Rasmussen et al. 2011; Alcott and Steenburgh 2013; Rasmussen et al. 2014).

The relative production of snow and graupel by the tested MP schemes strongly influence the distribution and amount of precipitation and, therefore, GSLE prediction skill. THOM and the Goddard (GODD; Tao et al. 1989) scheme produce more snow and the most realistic (i.e., banded) precipitation features, although GODD shifts precipitation too far downstream into Utah County. The Morrison et al. (2009) scheme and WDM6 produce more graupel (two and three times more than THOM, respectively) and less realistic (i.e., more elliptical) precipitation features. Hydrometeor mass source and sink terms for snow and graupel show that WDM6 creates graupel at a rate 10 times larger than THOM and grows graupel mass at a rate four times larger. Liu et al. (2011) asserted the WDM6 (and several other MP schemes) improperly applied Bigg's (1953) temperature and volume dependence for drop freezing to create graupel by freezing raindrops. Our results support the Liu et al. (2011) assertion and the approach used by THOM. Unfortunately, we do not know the observed ratio of snow to graupel in observed GSLE snowbands to constrain the uncertainty and guide MP improvements.

5.2 Future Work

To better inform future researchers and local forecasters on WRF performance, we need to verify a broader set of GSLE simulations. Future evaluation of WRF skill at predicting GSLE should consider forecast boundary conditions, null cases, mixed morphology GSLE events and events where GSLE was embedded in or concurrent with larger scale precipitation. We need to understand the skill of WRF at predicting mixed morphology events because if skill is low for these events, as it is for nonbanded GSLE events, skill will be low for the majority of GSLE forecasts. A larger sample of simulations will also confirm or refute the biases we found and may lead to approaches to improve GSLE simulations.

Research should also pursue the inability of WRF to simulate nonbanded GSLE events given that they are the most common GSLE morphology (Alcott et al. 2012). Our simulations tended to produce banded precipitation features in both banded and nonbanded GSLE events. To understand why this occurs, further simulations should be pursued as well as additional study to identify the environmental conditions responsible for the GSLE morphology. Simulations should focus on reducing grid spacing to explicitly represent convective motions that influence the resultant organization of convective elements into the GSLE morphology. Additional knowledge of the environmental conditions leading to the GSLE morphology may help delineate the differences in environmental conditions that result in banded and nonbanded GSLE events and identify weaknesses in the WRF simulations that lead to the banded precipitation feature bias.

Understanding the range of outcomes caused by the choice of MP scheme should be addressed both observationally and through further simulations. As suggested by Reeves and Dawson (2013) improved observations of the microphysical processes within lake effect systems in general and by extension GSLE is needed to validate parameterizations of snow and graupel production, growth, and fallout. A climatology of GSLE events incorporating data from the Multi-Angle Snowflake Camera (Garrett et al. 2012) and polarimetric data from the Weather Surveillance Radar-1988 Doppler (WSR–88D) at Promontory Point, Utah, would help us understand the microphysical aspects of GSLE storms. Analysis of aircraft, polarimetric radar, and ground-based microphysical samples collected during the 2013–2014 Ontario Winter Lake-effect Systems (OWLeS) field campaign east of Lake Ontario may provide insight into the microphysical aspects of lake effect over the Great Lakes that may be applicable to improving GSLE simulations. More GSLE events need to be simulated to determine if the sensitivity to MP choice in the 27 October 2010 event occurs in other GSLE events. The simulations should also examine the impact of grid spacing on MP performance to see if convection-resolving simulations improve MP scheme performance. Bryan and Morrison (2012) found a reduction in squall-line precipitation as grid spacing decreased from 1 to 0.25 km, but the differences between MP schemes remained similar regardless of resolution. It is not clear what effect grid spacing has on MP scheme performance in GSLE simulations, but simulating GSLE at convection-resolving grid spacings may help define an optimal deterministic simulation configuration for GSLE.

Finally our collective results illustrate the need to expand modeling research from a deterministic approach to an ensemble approach. Ensembles have the ability to produce forecasts that are equal to or better than deterministic forecasts; provide probabilistic information about forecast confidence; and ideally represent all possible simulation outcomes no matter how likely the outcome is (e.g., Leith 1974; Toth and Kalnay 1993; Toth et al. 1997; Stensrud et al. 2000; Gallus et al. 2005; Arnott 2010). In addition, testing an ensemble approach for GSLE simulations could improve prediction, illuminate deficiencies in deterministic models (i.e., poorly observed initial conditions, analysis quality, biases), and/or show whether or not GSLE events are predictable at all. A GSLE ensemble study could follow the approach of Gallus et al. (2005) where 25 simulations of a 1999 derecho event were run with varying initial conditions, parameterizations, and model cores to show that the event was not predicted in any simulation and an insufficient observation network contributed to the failure of the simulations.

REFERENCES

Adams-Selin, R., S. Van den Heever, and R. Johnson, 2013: Sensitivity of bow echo simulations to microphysical parameterizations. *Wea. Forecasting*, **141**, 1241–1262.

Alcott, T., W. J. Steenburgh, and N. F. Laird, 2012: Great Salt Lake-Effect precipitation: observed frequency, characteristics, and associated environmental factors. *Wea. Forecasting*, **27**, 954–971.

—–, and —–, 2013: Orographic influences on a Great Salt Lake-Effect snowstorm. *Mon. Wea. Rev.*, **141**, 2432–2450.

Aligo, E. A., W. A. Gallus, and M. Segal, 2009: On the impact of WRF model vertical grid resolution on midwest summer rainfall forecasts. *Wea. Forecasting*, **24**, 575–594.

Andersson, T., and S. Nilsson, 1990: Topographically induced convective snowbands over the Baltic Sea and their precipitation distribution. *Wea. Forecasting*, **5**, 299–312.

Anthes, R. A., 1986: The general question of predictability. *Mesoscale Meteorology and Forecasting*, P. S. Ray, Ed., Amer. Meteor Soc., 636–656.

Arnott, J. 2010: Examining a southward bias in lake-effect snow band forecasts in the northeast regional ensemble. *Nat. Wea. Digest*, **34**, 67–87.

Ballentine, R. J., and D. Zaff, 2007: Improving the understanding and prediction of lake-effect snowstorms in the eastern Great Lakes region. Final report to the COMET outreach program, Award No. S06-58395, September 2007, 41 pp.

Bigg, E. K., 1953: The formation of atmospheric ice crystals by the freezing of droplets. *Quart. J. Roy. Met. Soc.*, **79**, 510–519.

Brier, G. W., and R. A. Allen, 1951: Verification of weather forecasts. *Compendium of Meteorology*, T. F. Malone, Ed., Amer. Meteor. Soc., 841-848.

Bryan, G. H., J. C. Wyngaard, and J. M. Fritsch, 2003: Resolution requirements for the simulation of deep moist convection. *Mon. Wea. Rev.*, **131**, 2394–2416

——, and H. Morrison, 2012: Sensitivity of a simulated squall line to horizontal resolution and parameterization of microphysics. *Mon. Wea. Rev.*, **140**, 202–225.

Carpenter, D. M., 1993: The lake effect of the Great Salt Lake: Overview and forecast problems. *Wea. Forecasting*, **8**, 181–193.

Cha, Y., H. Lee, and S. Lee, 2011: Impacts of the high-resolution sea surface temperature distribution on modeled snowfall formation over the Yellow Sea during a cold-air outbreak. *Wea. Forecasting*, **26**, 487–503.

Chen, F., and J. Dudhia, 2001: Coupling an advanced land surface-hydrology model with the Penn State-NCAR MM5 modeling system. Part II: Preliminary model validation. *Mon. Wea. Rev.,* **129**, 587–604.

Chen, S. H., and W. Y. Sun, 2002: A one-dimensional time dependent cloud model. *J. Met. Soc. Japan*, **80**, 99–118.

Clark, A. J., W. A. Gallus, and M. L. Weisman, 2010: Neighborhood-based verification of precipitation forecasts from convection-allowing NCAR WRF model simulations and the operational NAM. *Wea. Forecasting*, **25**, 1495–1509.

Colle, B. A., K. J. Westrick, and C. F. Mass, 1999: Evaluation of MM5 and Eta-10 precipitation forecasts over the Pacific Northwest during the cool season. *Wea. Forecasting*, **14**, 137–154.

——, and C. F. Mass, 2000: The 5–9 February 1996 flooding event over the Pacific Northwest: sensitivity studies and evaluation of the MM5 precipitation forecasts. *Mon. Wea. Rev.*, **128**, 593–617.

——, ——, and K. J. Westrick, 2000: MM5 precipitation verification over the Pacific Northwest during the 1997–99 cool seasons. *Wea. Forecasting*, **15**, 730–744.

——, J. B. Olson, and J. S. Tongue, 2003: Multiseason verification of the MM5. Part II: evaluation of high-resolution precipitation forecasts over the northeastern United States. *Wea. Forecasting*, **18**, 458–480.

——, Y. Lin, S. Medina, and B. F. Smull, 2008: Orographic modification of convection and flow kinematics by the Oregon Coast Range and Cascades during IMPROVE-2. *Mon. Wea. Rev.*, **136**, 3894–3916.

Cooper, W. A., 1986: Ice initiation in natural clouds. *Precipitation Enhancement—A Scientific Challenge, Meteor. Monogr.*, No. 43, Amer. Meteor. Soc., 29–32.

Cordeira, J. M., and N. F. Laird, 2008: The influence of ice cover on two lake-effect snow events over Lake Erie. *Mon. Wea. Rev.*, **136**, 2747–2763.

Crosman, E. T., and J. D. Horel, 2010: MODIS-derived surface temperature of the Great Salt Lake, 2008. *Remote Sens. Environ.*, **113**, 73–81.

Crum, T. D., R. L. Alberty, and D. W. Burgess, 1993: Recording, archiving, and using WSR-88D data. *Bull. Amer. Meteor. Soc.*, **74**, 645–653.

Davis, C.A., B.G. Brown, and R.G. Bullock, 2006a: Object based verification of precipitation forecasts, Part I: Methodology and application to mesoscale rain areas. *Mon. Wea. Rev.*, **134**, 1772–1784.

—, ——, ——, 2006b: Object-based verification of precipitation forecasts. Part II: application to convective rain systems. *Mon. Wea. Rev.*, **134**, 1785–1795.

——, ——, ——, and J. Halley-Gotway, 2009: The Method for Object-Based Diagnostic Evaluation (MODE) applied to numerical forecasts from the 2005 NSSL/SPC spring program. *Wea. Forecasting*, **24**, 1252–1267.

Duda, J. D., and W. A. Gallus, 2013: The impact of large-scale forcing on skill of simulated convective initiation and upscale evolution with convection-allowing grid spacings in the WRF. *Wea. Forecasting*, **28**, 994–1018.

Ebert, E. E., and J. L. McBride, 2000: Verification of precipitation in weather systems: Determination of systematic errors. *J. Hydrol.*, **239**, 179–202.

——, 2009: Neighborhood verification: a strategy for rewarding close forecasts. *Wea. Forecasting*, **24**, 1498–1510.

——, and W. A. Gallus, 2009: Toward better understanding of the Contiguous Rain Area (CRA) method for spatial forecast verification. *Wea. Forecasting*, **24**, 1401–1415.

Ellis, A. W., and D. J. Leathers, 1996: A synoptic climatological approach to the analysis of lake-effect snowfall: potential forecasting applications. *Wea. Forecasting*, **11**, 216–229.

Emanuel, K. A., 1994: *Atmospheric Convection.* Oxford University Press, 580 pp.

Estoque, M. A., and K. Ninomiya, 1976: Numerical simulation of Japan Sea-Effect snowfall. *Tellus,* **28**, 243–253.

Ferrier, B., 1994: A double-moment multiple-phase four-class bulk ice scheme. Part I: description. *J. Atmos. Sci.*, **51**, 249–280.

Fovell, R. G., and Y. Ogura, 1988: Numerical simulation of a midlatitude squall line in two dimensions. *J. Atmos. Sci.*, **45**, 3846–3879.

Fujiyoshi, Y., N. Yoshimoto, and T. Takeda, 1998: A dual-doppler radar study of longitudinal-mode snowbands. Part I: a three-dimensional kinematic structure of meso-g-scale convective cloud systems within a longitudinal-mode snowband. *Mon. Wea. Rev.*, **126**, 72–91.

Gallus, W. A., 2002: Impact of verification grid-box size on warm-season QPF skill measures. *Wea. Forecasting*, **17**, 1296–1302.

–––, J. Correia, and I. Jankov, 2005: The 4 June 1999 derecho event: a particularly difficult challenge for numerical weather prediction. *Wea. Forecasting*, **20**, 705–728.

–––, 2010: Application of object-based verification techniques to ensemble precipitation forecasts. *Wea. Forecasting*, **25**, 144–158.

Garrett, T. J., C. Fallgatter, K. Shkurko, and D. Howlett, 2012: Fallspeed measurement and high-resolution multi-angle photography of hydrometeors in freefall. *Atmos. Meas. Tech. Discussions* 5, **4**, 4827–4850.

Garvert, M. F., B. A. Colle, and C. F. Mass, 2005: The 13–14 December 2001 IMPROVE-2 event. Part I: synoptic and mesoscale evolution and comparison with a mesoscale model simulation. *J. Atmos. Sci.*, **62**, 3474–3492.

Germann, U., and J. Joss, 2004: Operational measurement of precipitation in mountainous terrain. *Weather Radar*. Springer Berlin Heidelberg. 52–77.

–––, I. Zawadzki, and B. Turner, 2006: Predictability of precipitation from continental radar images. Part IV: limits to prediction. *J. Atmos. Sci.*, **63**, 2092–2108.

Gilbert, G. K., 1884: Finley's tornado predictions. *Amer. Meteor. J.*, **1**, 166–172.

Hacker, J. P., 2010: Spatial and temporal scales of boundary layer wind predictability in response to small-amplitude land surface uncertainty. *J. Atmos. Sci.*, **67**, 217–233.

Hamill, T. M., F. Yang, C. Cardinali, and S. J. Majumdar, 2013: Impact of targeted winter storm reconnaissance dropwindsonde data on midlatitude numerical weather predictions. *Mon. Wea. Rev.*, **141**, 2058–2065.

Hart, K. A., W. J. Steenburgh, and D. J. Onton, 2005: Model forecast improvements with decreased horizontal grid spacing over finescale intermountain orography during the 2002 Olympic Winter Games. *Wea. Forecasting*, **20**, 558–576.

Hjelmfelt, M. R., and R. R. Braham, 1983: Numerical simulation of the airflow over Lake Michigan for a major lake-effect snow event. *Mon. Wea. Rev.*, **111**, 205–219.

——,1990: Numerical study of the influence of environmental conditions on lake-effect snowstorms over Lake Michigan. *Mon. Wea. Rev.*, **118**, 138–150.

——, 1992: Orographic effects in simulated lake-effect snowstorms over Lake Michigan. *Mon. Wea. Rev.*, **120**, 373–377.

Holt, T. R., D. Niyogi, F. Chen, K. Manning, M. A. LeMone, and A. Qureshi, 2006: Effect of land-atmosphere interactions on the IHOP 24–25 May 2002 convection case. *Mon. Wea. Rev.*, **134**, 113–133

Hong, S.-Y., J. Dudhia, and S.-H. Chen, 2004: A revised approach to ice microphysical processes for the bulk parameterization of clouds and precipitation. *Mon. Wea. Rev.,* **132**, 103–120.

——, and J. O. J. Lim, 2006: The WRF single-moment 6-class microphysics scheme (WSM6). *J. Korean Meteor. Soc.*, **42**, 129–151.

——, Y. Noh, and J. Dudhia, 2006: A new vertical diffusion package with an explicit treatment of entrainment processes. *Mon. Wea. Rev.*, **134**, 2318–2341.

Horel, J., and Coauthors, 2002: Mesowest: cooperative Mesonets in the Western United States. *Bull. Amer. Meteor. Soc.*, **83**, 211–225.

Hozumi, K., and C. Magono, 1984: The cloud structure of convergent cloud bands over the Japan Sea in winter monsoon period. *J. Met. Soc. Japan,* **62**, 522–533.

Iacono, M. J., J. S. Delamere, E. J. Mlawer, M. W. Shepard, S. A. Clough, and W. D. Collins, 2008: Radiative forcing by long lived greenhouse gases: calculations with the AER radiative transfer models. *J. Geophys. Res.,* **113**.

Jankov, I., W. A. Gallus, M. Segal, B. Shaw, and S. E. Koch, 2005: The impact of different WRF model physical parameterizations and their interactions on warm season MCS rainfall. *Wea. Forecasting*, **20**, 1048–1060.

——, J. W. Bao, P. J. Neiman, P. J. Schultz, H. Yuan, and A. B. White, 2009: Evaluation and comparison of microphysical algorithms in ARW-WRF model simulations of atmospheric river events affecting the California coast. *J. Hydrometeor*, **10**, 847–870.

Juga, I., 2010: Sea-effect snowfall – a special hazard for road traffic in the coastal areas of Finland. *15th International Road Weather Conference,* Quebec City, Canada, 5–7 February 2010 Session.

Kain, J. S., 2004: The Kain-Fritsch convective parameterization: an update. *J. Appl. Meteor.*, **43**, 170–181.

——, M. E. Baldwin, P. R. Janish, S. J. Weiss, M. P. Kay, and G. W. Carbin, 2003: Subjective verification of numerical models as a component of a broader interaction between research and operations. *Wea. Forecasting*, **18**, 847–860.

Kindap T., 2010: A severe sea-effect snow episode over the city of Istanbul. *Nat. Hazards*, **54**, 707–723.

Kelly, R. D., 1986: Mesoscale frequencies and seasonal snowfalls for different types of Lake Michigan snow storms. *J. Climate Appl. Meteor.*, **25**, 308–312.

Kristovich, D. A. R., N. F. Laird, 1998: Observations of widespread lake-effect cloudiness: influences of lake surface temperature and upwind conditions. *Wea. Forecasting*, **13**, 811–821.

Laird, N. F., D. A. R. Kristovich, and J. E. Walsh, 2003a: Idealized model simulations examining the mesoscale structure of winter lake-effect circulations. *Mon. Wea. Rev.*, **131**, 206–221.

——, J. E. Walsh, and D. A. R. Kristovich, 2003b: Model simulations examining the relationship of lake-effect morphology to lake shape, wind direction, and wind speed. *Mon. Wea. Rev.*, **131**, 2102–2111.

——, and D. A. R. Kristovich, 2004: Comparison of observations with idealized model results for a method to resolve winter lake-effect mesoscale morphology. *Mon. Wea. Rev.*, **132**, 1093–1103.

——, J. Desrochers, and M. Payer, 2009: Climatology of lake-effect precipitation events over Lake Champlain. *J. Appl. Meteor. Climatol.*, **48**, 232–250.

——, R. Sobash, and N. Hodas, 2010: Climatological conditions of lake-effect precipitation events associated with the New York State Finger Lakes. *J. Appl. Meteor. Climatol.*, **49**, 1052–1062.

Langhans, W., J. Schmidli, and C. Schär, 2012: Bulk convergence of cloud-resolving simulations of moist convection over complex terrain. *J. Atmos. Sci.*, **69**, 2207–2228.

Lavoie, R. L., 1972: A mesoscale numerical model of lake-effect storms. *J. Atmos. Sci.*, **29**, 1025–1040.

Leith, C. E., 1974: Theoretical skill of Monte Carlo forecasts. *Mon. Wea. Rev.*, **102**, 409–418.

Lim, K. S. S., and S. Y. Hong, 2010. Development of an effective double-moment cloud microphysics scheme with prognostic cloud condensation nuclei (CCN) for weather and climate models. *Mon. Wea. Rev.*, **138,** 1587–1612.

Lin, Y.-L., R. D. Farley, and H. D. Orville, 1983: Bulk parameterization of the snow field in a cloud model. *J. Climate Appl. Meteor.*, **22**, 1065–1092.

——, and B. A. Colle, 2011: A new bulk microphysical scheme that includes riming intensity and temperature-dependent ice characteristics. *Mon. Wea. Rev.*, **139**, 1013–1035.

Liu, C., and M. W. Moncrief, 2007: Sensitivity of cloud-resolving simulations of warm-season convection to cloud microphysics parameterizations. *Mon. Wea. Rev.*, **135**, 2854–2868.

——, K. Ikeda, G. Thompson, R. Rasmussen, and J. Dudhia, 2011: High-resolution simulations of wintertime precipitation in the Colorado Headwaters Region: sensitivity to physics parameterizations. *Mon. Wea. Rev.*, **139**, 3533–3553.

Lorenz, E. N., 1982: Atmospheric predictability experiments with a large numerical model. *Tellus*, **34**, 505–513.

Magono, C., K. Kikuchi, T. Kimura, S. Tazawa, and T. Kasai, 1966: A study on the snowfall in the winter monsoon season in Hokkaido with special reference to low land snowfall. *J. Fac. Sci., Hokkaido Univ., Ser. VII,* **11,** 287–308.

Marzban, C., and S. Sandgathe, 2006: Cluster analysis for verification of precipitation fields. *Wea. Forecasting*, **21**, 824–838.

——, and ——, 2008: Cluster analysis for object-oriented verification of fields: a variation. *Mon. Wea. Rev.*, **136**, 1013–1025.

——, ——, and H. Lyons, 2008: An object-oriented verification of three NWP model formulations via cluster analysis: an objective and a subjective analysis. *Mon. Wea. Rev.*, **136**, 3392–3407.

Mass, C. F., D. Ovens, K. Westrick, and B. A. Colle, 2002: Does increasing horizontal resolution produce more skillful forecasts? *Bull. Amer. Meteor. Soc.*, **83**, 407–430.

Mesinger, F., 1996: Improvements in quantitative precipitation forecasts with the Eta regional model at the National Centers for Environmental Prediction: the 48-km upgrade. *Bull. Amer. Meteor. Soc.*, **77**, 2637–2649.

Meyers, M. P., P. J. DeMott, and W. R. Cotton, 1992: New primary ice-nucleation parameterizations in an explicit cloud model. *J. Appl. Meteor.*, **31**, 708–721.

Mitchell, C. L., 1921: Snow flurries along the eastern shore of Lake Michigan. *Mon. Wea. Rev.,* **49**, 502–503.

Milbrandt, J. A., and M. K. Yau, 2005: A multimoment bulk microphysics parameterization. Part II: a proposed three-moment closure and scheme description. *J. Atmos. Sci.*, **62**, 3065–3081.

—–, M. K. Yau, J. Mailhot, S. Bélair, and R. McTaggart-Cowan, 2010: Simulation of an orographic precipitation event during IMPROVE-2. Part II: sensitivity to the number of moments in the bulk microphysics scheme. *Mon. Wea. Rev.*, **138**, 625–642.

Mizukoshi, M., 1977: Climatic Division and Climatography. *The Climate of Japan*, E. Fukui, Ed., Kondasha, 225–270.

Morrison, H., and J. O. Pinto, 2005: Mesoscale modeling of springtime Arctic mixed-phase stratiform clouds using a new two-moment bulk microphysics scheme. *J. Atmos. Sci.*, **62**, 3683–3704.

—–, G. Thompson, and V. Tatarskii, 2009: Impact of cloud microphysics on the development of trailing stratiform precipitation in a simulated squall line: comparison of one- and two-moment schemes. *Mon. Wea. Rev.*, **137**, 991–1007.

—–, and J. Milbrandt, 2011: Comparison of two-moment bulk microphysics schemes in idealized supercell thunderstorm simulations. *Mon. Wea. Rev.*, **139**, 1103–1130.

Mullen, S. L., J. Du, and F. Sanders, 1999: The dependence of ensemble dispersion on analysis-forecast systems: implications to short-range ensemble forecasting of precipitation. *Mon. Wea. Rev.*, **127**, 1674–1686.

Nachamkin, J. E., 2004: Mesoscale verification using meteorological composites. *Mon. Wea. Rev.*, **132**, 941–955.

——, S. Chen, and J. Schmidt, 2005: Evaluation of heavy precipitation forecasts using composite-based methods: a distributions oriented approach. *Mon. Wea. Rev.*, **133**, 2163–2177.

——, 2009: Application of the composite method to the spatial forecast verification methods intercomparison dataset. *Wea. Forecasting*, **24**, 1390–1400.

Nicholls, M. E., 1987: A comparison of the results of a two-dimensional numerical simulation of a tropical squall line with observations. *Mon. Wea. Rev.*, **115**, 3055–3077.

Niziol, T. A., 1987: Operational forecasting of lake-effect snowfall in western and central New York. *Wea. Forecasting*, **2**, 310–321.

——, W. R. Snyder, and J. S. Waldstreicher, 1995: Winter weather forecasting throughout the eastern United States. Part IV: lake-effect snow. *Wea. Forecasting*, **10**, 61–77.

Ohigashi, T., and K. Tsuboki, 2005: Structure and maintenance process of stationary double snowbands along the coastal region. *J. Met. Soc. Japan*, **83**, 331–349.

——, and ——, 2007: Shift and intensification processes of the Japan-Sea polar-airmass convergence zone associated with the passage of a mid-tropospheric cold core. *J. Met. Soc. Japan,* **85**, 633–662.

Ohtake, H., M. Kawashima, and Y. Fujiyoshi, 2009: The formation mechanism of a thick cloud band over the northern part of the Sea of Japan during cold air outbreaks. *J. Met. Soc. Japan*, **87**, 289–306.

Onton, D. J., and W. J. Steenburgh, 2001: Diagnostic and sensitivity studies of the 7 December 1998 Great Salt Lake–Effect snowstorm. *Mon. Wea. Rev.*, **129**, 1318–1338.

Passarelli, R. E., and R. R. Braham, 1981: The role of the winter land breeze in the formation of Great Lake snow storms. *Bull. Amer. Meteor. Soc.*, **62**, 482–492.

Payer, M., J. Desrochers, and N. F. Laird, 2007: A lake-effect snowband over Lake Champlain. *Mon. Wea. Rev.*, **135**, 3895–3900.

Peace, R. L., and R. B. Sykes, 1966: Mesoscale study of a lake-effect snowstorm. *Mon. Wea. Rev.*, **94**, 495–507.

Pease, S. R., W. A. Lyons, C. S. Keen, and M. R. Hjelmfelt, 1988: Mesoscale spiral vortex embedded within a Lake Michigan snow squall band: high resolution satellite observations and numerical model simulations. *Mon. Wea. Rev.*, **116**, 1374–1380.

Petch, J. C., and M. E. B. Gray, 2001: Sensitivity studies using a cloud-resolving model simulation of the tropical west Pacific. *Quart. J. Roy. Meteor. Soc.*, **127**, 2287–2306.

——, A. R. Brown, and M. E. B. Gray, 2002: The impact of horizontal resolution on the simulations of convective development over land. *Quart. J. Roy. Meteor. Soc.*, **128**, 2031–2044.

Petterssen, S., and P.A. Calabrese, 1959: On some weather influences due to warming of the air by the Great Lakes in winter. *J. of Meteor.*, **16**, 646–652.

Rasmussen, R., M. Dixon, S. Vasiloff, F. Hage, S. Knight, J. Vivekanandan, and M. Xu, 2003: Snow nowcasting using a real-time correlation of radar reflectivity with snow gauge accumulation. *J. Appl. Meteor.*, **42**, 20–36.

Reeves, H. D., and D. T. Dawson, 2013: The dependence of QPF on the choice of microphysical parameterization for lake-effect snowstorms. *J. Appl. Meteor. Climatol.*, **52**, 363–377.

Rotunno, R., J. B. Klemp, and M. L. Weisman, 1988: A theory for strong, long-lived squall lines. *J. Atmos. Sci.*, **45**, 463–485.

Rutledge, S. A., and P. V. Hobbs, 1983: The mesoscale and microscale structure and organization of clouds and precipitation in midlatitude cyclones. Part VIII: a model for the ''seeder-feeder'' process in warm-frontal rainbands. *J. Atmos. Sci.,* **40**, 1185–1206.

Saito, K., M. Murakami, T. Matsuo, and H. Mizuno, 1996: Sensitivity experiments on the orographic snowfall over the mountainous region of northern Japan. *J. Met. Soc. Japan,* **74**, 797–813.

Schwartz, C. S., and Coauthors, 2009: Next-day convection-allowing WRF model guidance: a second look at 2-km versus 4-km grid spacing. *Mon. Wea. Rev.*, **137**, 3351–3372.

Scott, R. W., and F. A. Huff, 1996: Impacts of the Great Lakes on regional climate conditions. *J. Great Lakes Res.*, **22**, 845–863.

Shi, J. J., and Coauthors, 2010: WRF Simulations of the 20–22 January 2007 snow events over eastern Canada: comparison with in situ and satellite observations. *J. Appl. Meteor. Climatol.*, **49**, 2246–2266.

Skamarock, W. C., and J. B. Klemp, 2008: A time-split nonhydrostatic atmospheric model for weather research and forecasting applications. *J. Comput. Phys.*, **227**, 3465–3485.

Slemmer, J. W., 1998. Characteristics of winter snowstorms near Salt Lake City as deduced from surface and radar observations. Doctoral dissertation, Dept. of Meteorology, University of Utah. pp. 138.

Stamus, P. A., F. H. Carr, and D. P. Baumhefner, 1992: Application of a scale-separation verification technique to regional forecast models. *Mon. Wea. Rev.*, **120**, 149–163.

Steenburgh, W. J., S. F. Halvorson, and D. J. Onton, 2000: Climatology of lake-effect snowstorms of the Great Salt Lake. *Mon. Wea. Rev.*, **128**, 709–727.

——, and D. J. Onton, 2001: Multiscale analysis of the 7 December 1998 Great Salt Lake-Effect snowstorm. *Mon. Wea. Rev.*, **129**, 1296–1317.

Stensrud, D. J., J. W. Bao, and T. T. Warner, 2000: Using initial condition and model physics perturbations in short-range ensemble simulations of mesoscale convective systems. *Mon. Wea. Rev.*, **128**, 2077–2107.

——, 2007: *Parameterization Schemes: Keys to Understanding Numerical Weather Prediction Models*. Cambridge University Press. 480 pp.

Stevens, D. E., A. S. Ackerman, and C. S. Bretherton, 2002: Effects of domain size and numerical resolution on the simulation of shallow cumulus convection. *J. Atmos. Sci.*, **59**, 3285–3301.

Stratman, D. R., M. C. Coniglio, S. E. Koch, and M. Xue, 2013: Use of multiple verification methods to evaluate forecasts of convection from hot- and cold-start convection-allowing models. *Wea. Forecasting*, **28**, 119–138.

Sun, J., and Coauthors, 2014: Use of NWP for nowcasting convective precipitation: recent progress and challenges. *Bull. Amer. Meteor. Soc.*, **95**, 409–426.

Szeto, K. K., and H. Cho, 1994: A numerical investigation of squall lines. Part III: Sensitivity to precipitation processes and the Coriolis force. *J. Atmos. Sci.*, **51**, 1341–1351.

Tadashi, A. R. M., 1977: Water Balance. *The Climate of Japan*, E. Fukui, Ed., Kondasha, 167–197.

Takemi, T., H. Y. Inoue, K. Kusunoki, and K. Bessho, 2009: The development and intensification of multiple misocyclones in shallow cumulus convection over the warm ocean during winter cold outbreak. Preprints, 13th Conf. on Mesoscale Processes, Salt Lake City, UT, Amer. Meteor. Soc., 16.3

Tao, W. K., and J. Simpson, 1989: Modeling study of a tropical squall-type convective line. *J. Atmos. Sci.*, **46**, 177–202.

——, ——, and M. McCumber, 1989: An ice-water saturation adjustment. *Mon. Wea. Rev.*, **117**, 231–235.

——, ——, D. Baker, S. Braun, M. D. Chou, B. Ferrier, D. Johnson, A. Khain, S. Lang, B. Lynn, C. L. Shie, D. Starr, C. H. Sui, Y. Wang, and P. Wetzel, 2003: Microphysics, radiation and surface processes in the Goddard Cumulus Ensemble (GCE) model. *Meteorol. Atmos. Phys.*, **82**, 97–137.

Theeuwes, N. E., G. J. Steeneveld, F. Krikken, and A. A. M. Holtslag, 2010: Mesoscale modeling of lake-effect snow over Lake Erie, sensitivity to convection, microphysics and the water temperature. *Adv. Sci. Res.*, **4**, 15–22.

Thompson, G., R. M. Rasmussen, and K. Manning, 2004: Explicit forecasts of winter precipitation using an improved bulk microphysics scheme. Part I: description and sensitivity analysis. *Mon. Wea. Rev.*, **132**, 519–542.

–––, P. R. Field, R. M. Rasmussen, and W. D. Hall, 2008: Explicit forecasts of winter precipitation using an improved bulk microphysics scheme. Part II: implementation of a new snow parameterization. *Mon. Wea. Rev.*, **136**, 5095–5114.

Toth, Z., and E. Kalnay, 1993: Ensemble forecasting at NMC: the generation of perturbations. *Bull. Amer. Meteor. Soc.*, **74**, 2317–2330.

–––, –––, S. M. Tracton, R. Wobus, and J. Irwin, 1997: A synoptic evaluation of the NCEP ensemble. *Wea. Forecasting*, **12**, 140–153.

U.S. Census Bureau cited 2014: 2010 Census data. [Available online at http://2010.census.gov/2010census/data/.]

U. S. Geological Survey cited 2014: Great Salt Lake, Utah. [Available online at http://ut.water.usgs.gov/greatsaltlake/.]

Van Weverberg, K., A. M. Vogelmann, H. Morrison, and J. A. Milbrandt, 2012: Sensitivity of idealized squall-line simulations to the level of complexity used in two-moment bulk microphysics schemes. *Mon. Wea. Rev.*, **140**, 1883–1907.

Weisman, M. L., 1992: The role of convectively generated rear-inflow jets in the evolution of long-lived mesoconvective systems. *J. Atmos. Sci.*, **49**, 1826–1847.

–––, W. C. Skamarock, and J. B. Klemp, 1997: The resolution dependence of explicitly modeled convective systems. *Mon. Wea. Rev.*, **125**, 527–548.

–––, C. Davis, W. Wang, K. W. Manning, and J. B. Klemp, 2008: Experiences with 0–36-h explicit convective forecasts with the WRF-ARW model. *Wea. Forecasting*, **23**, 407–437.

Wernli, H., M. Paulat, M. Hagen, and C. Frei, 2008: SAL-A novel quality measure for the verification of quantitative precipitation forecasts. *Mon. Wea. Rev.*, **136**, 4470–4487.

––––, C. Hofmann, and M. Zimmer, 2009: Spatial forecast verification methods intercomparison project: application of the SAL technique. *Wea. Forecasting*, **24**, 1472–1484.

Westrick, K. J., C. F. Mass, and B. A. Colle, 1999: The limitations of the WSR-88D radar network for quantitative precipitation measurement over the coastal western United States. *Bull. Amer. Meteor. Soc.*, **80**, 2289–2298.

Wilks, D. S., 2006: *Statistical Methods in the Atmospheric Sciences.* Academic Press, 627 pp.

Williams, G. C., 1963: Weather note: An occurrence of lake snow one of the direct effects of Lake Michigan on the climate of the Chicago area. *Mon. Wea. Rev.*, **91**, 465–467.

Wright, D. M., D. J. Posselt, and A. L. Steiner, 2013: Sensitivity of lake-effect snowfall to lake ice cover and temperature in the Great Lakes region. *Mon. Wea. Rev.*, **141**, 670–689.

Wu, L., and G. W. Petty, 2010: Intercomparison of bulk microphysics schemes in model simulations of polar lows. *Mon. Wea. Rev.*, **138**, 2211–2228.

Yeager, K. N., W. J. Steenburgh, and T. I. Alcott, 2013: Contributions of lake-effect periods to the cool-season hydroclimate of the Great Salt Lake basin. *J. Appl. Meteor.*, **52**, 341–362.

Yoshimoto, N., Y. Fujiyoshi, and T. Takeda, 2000: A dual-doppler radar study of longitudinal-mode snowbands. Part II: influence of the kinematics of a longitudinal-mode snowband on the development of an adjacent snowband. *J. Met. Soc. Japan*, **78**, 381–403.

Yoshino, M. M., 1977: The Winter Monsoon. *The Climate of Japan*, E. Fukui, Ed., Kondasha, 65–84.